Aeroacoustic Phenomenon in centrifugal compressors

A Lattice Boltzmann Method based approach

Rahul Phogat

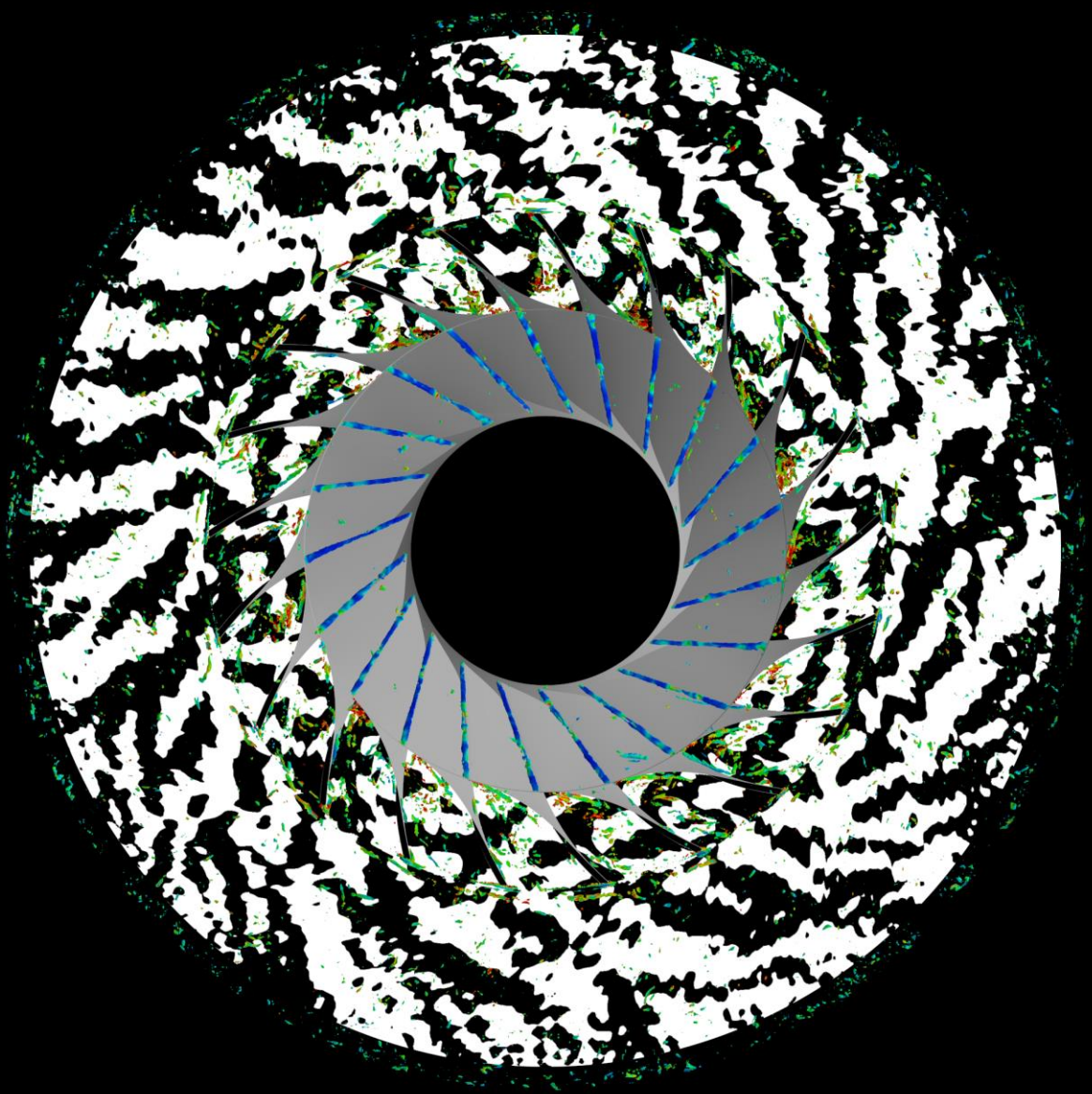

Aeroacoustic Phenomenon in centrifugal compressors

A Lattice Boltzmann Method based approach

By

Rahul Phogat

in partial fulfilment of the requirements for the degree of

Master of Science
in Aerospace Engineering

at the Delft University of Technology,
to be defended on Wednesday, May 29, 2019, at 10:00 AM.

Student number:	4617096	
Supervisor:	Dr. F. (Francesco) Avallone	TU Delft
Thesis committee:	Prof. dr. Damiano Casalino	TU Delft
	Dr. M. (Matteo) Pini	TU Delft
	Ir. Néstor González Díez	TNO

TU Delft

TNO innovation for life

Preface

The following quote summarises my philosophy in life:

"Run like a mad-man towards what scares you, but still attracts you…"

Rahul Phogat
Vellore, November 2017

I believe that one of the definite ways of progressing in life is to strive to grow beyond one's comfort zone. This belief has guided me in the adult years of my life. I remember it all so clearly how pursuing a Master of Science degree in Aerospace Engineering with a background in Mechanical Engineering seemed quite daunting. The journey was longer and more challenging than I anticipated. My experiences as a graduate student at TU Delft helped me grow both personally and professionally. I learnt that consistency and hard work are the key ingredients of achieving success and that being an engineer is a journey and not a destination. I feel happy about finishing this phase of my life while looking forward to the adventures time holds for me.

These were undoubtedly the most challenging years of my life where some days I struggled to push my physical and mental limits. I want to sincerely thank all the people who showed their support during this period. It would not have been able to get this far without their love, support and help. Firstly, I must express my gratitude to my advisors at TNO, who made this project possible. Thanks to *Néstor González Díez* and *Jan Smeulers* for introducing me to the world of turbomachinery aeroacoustics. Their support has been fundamental not to lose sight of the final objective. They motivated me and helped me get through the hurdles that I faced during this project. In times where I bugged them with more or less stupid questions, they always offered their warm support.

The work presented here could not have been possible without the patient support of *Damiano Casalino* and *Francesco Avallone. Damiano* introduced me to *SIMULIAcloud*, giving me access to the *LBM* solver *PowerFLOW* and virtually unlimited computational resources. A computationally expensive case like this would have been impossible otherwise. It was a pleasure working with *Francesco*, who supervised my work regularly. His enthusiasm was praiseworthy throughout the project. Thanks to *Ignacio Gonzalez-Martino,* who offered his generous support during the case-setup and implementation related hurdles in this project.

I must express my gratitude to my flatmate, a friend that turned into a brother, *Kaustubh,* with whom I shared most of my journey as a student at TU Delft. We both have been to hell and back! He was kind enough to offer his generous support during the project with his expertise in *CAD*. Thanks to *music*, my new-found hobby that helped me feed my soul in desperate times. Expressing my thoughts and emotions in a small home studio helped rejuvenate me.

Last but not least, thanks to my family, who trusted me and believed in me since I shared with them my plan of going abroad. Thanks to my mother, *Krishna* who was with me in Delft during the last and probably the hardest month of my thesis. Her endless love, support and positivity helped me regain perspective when I needed it the most. My sister *Kanika*, who also played the role of a mother in counselling me during her time in Amsterdam. My father, *Surender*, who always inspired me to take a step back and enjoy the journey.

Table of Contents

Abbreviations

BGK	Bhatnagar-Cross-Krook
BPF	Blade Passing Frequency
CAA	Computational Aeroacoustics
CFD	Computational Fluid Dynamics
DFT	Discrete Fourier Transform
FEA	Finite Element Analysis
FES	Finite Equivalent Surfels
FEV	Finite Equivalent Voxels
FFT	Fast-Fourier Transform
HCF	High Cycle Fatigue
HVAC	Heating, ventilation, and air conditioning
ILES	Implicit Large Eddy Simulation
LB/VLES	Lattice Boltzmann/Very Large Eddy Simulation
LBM	Lattice Boltzmann Method
LCF	Low Cycle Fatigue
LES	Large Eddy Simulation
ND	Nodal Diameters
NS	Navier-Stokes
ODS	Operating Deflection Shape
OEM	Original Equipment Manufacturer
OGV	Outlet Guide Vanes
RNG	Renormalization Group Theory
TSM	Tyler-Sofrin Modes
URANS	Unsteady Reynold's Averaged Navier Stokes
VPF	Vane Passing Frequency
VR	Variable Resolution

Abstract

Flow unsteadiness caused by impeller rotation, vortex-shedding, secondary flows etc. can lead to the generation of acoustic waves within the turbomachinery cascade. This causes pressure loading on the impeller. When acoustic resonance occurs, i.e. the frequency of acoustic wave excitation matches with the structural natural frequencies of the impeller, high fatigue and vibrations are encountered, which can lead to structural failure. Centrifugal compressor applications like turbocharging and process engineering require an advanced understanding of the aeroacoustic excitation mechanisms as these have been suspected of playing a significant role in structural failures. Given that the current state-of-the-art analysis methods are incapable of explaining various instances of structural failures, a novel Lattice Boltzmann Method (LBM) based approach is explored. For the first time, aerodynamic and performance predictions, along with aeroacoustic amplitudes from the LBM based approach will be compared with a conventional Unsteady Reynolds Averaged Navier Stokes (URANS) based approach as well as test rig data. This will assess the feasibility of the LBM model for analysing forced response behaviour of a centrifugal compressor operating at conditions of acoustic resonance. The research compressor has been chosen based on an aeromechanic test campaign where high impeller blade trailing edge vibrations were measured. The computational domain consists of full compressor wheel including the hub and the shroud cavities. An attempt will be made to quantify the resonant amplification factor by simulating off-resonant conditions. The findings from this research would result in the development of a numerical framework for assessing the physics and severity of resonant excitations in centrifugal compressors. It will also highlight the importance of accounting for aeroacoustic mechanisms in the aeromechanical design of centrifugal compressor stages.

Keywords - high-cycle fatigue, Tyler-Sofrin modes, acoustic resonance, triple-coincidence, impeller loading, vibro-acoustic resonance.

List of Tables

List of Figures

1 Introduction

1.1. Centrifugal compressors

Centrifugal compressors are robust, compact and capable of operating at high-pressure ratios. They are used in process engineering for flow compression and transportation. In the aerospace industry, they are used in rocket and helicopter engines where compact and light-weight designs are needed. A centrifugal compressor usually consists of a rotating impeller followed by a diffuser. The fluid enters the impeller in the axial direction and exits in the radial direction. Torque from the impeller blades is transferred to the fluid increasing kinetic energy and Mach number. The total pressure rise in a centrifugal compressor stage is realised in two consecutive steps. Firstly, the flow is accelerated by the rotating component (i.e. the impeller), which increases kinetic energy. Then, the flow is decelerated in the stationary component (i.e. the diffuser) resulting in pressure rise [1]. The centrifugal compressor rig shown in Figure 1 [2] has a shrouded impeller and a vaneless diffuser. The inlet and return guide vanes are highlighted.

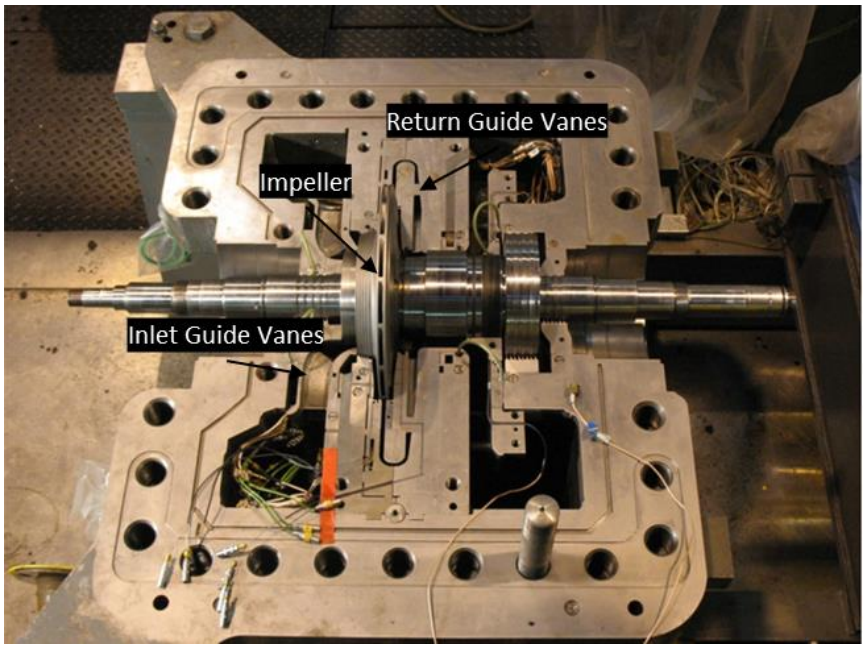

Figure 1 Cut-section of a centrifugal compressor rig [2].

Advancements in the field of compact gas turbine engines required by military helicopters in the 1960s lead to rapid advancements in centrifugal compressor capabilities. Previously, research efforts in the centrifugal compressor domain were mainly directed to aerodynamic aspects with the aim of increasing performance and efficiency. This involved designing the aerodynamic flow path inside the compressor which is characterised by highly complex three-dimensional flow features. Typical investigations in this field involve the modelling of impeller wake, tip leakage flows and the resulting impeller-diffuser interaction. This required intensive experimental and computational research efforts. With the advent of advanced numerical techniques and availability of computational resources, high fidelity computational methods are now capable of simulating larger three-dimensional computational domains, thus, enabling detailed insights of various flow structures within the compressor.

The consistent trend towards improving the aerodynamic performance of centrifugal compressors pushes modern designs to their mechanical limits. Higher pressure ratios are achieved by increasing rotational speeds and mass flow rates. Consequently, this leads to an increase in unsteady interaction between components that might cause fatigue failures. Further advancement along this trend requires a better understanding of fluctuating aerodynamic loads and the resulting aero-mechanic performance of the compressor.

1.2. Forced vibratory response in turbomachinery

Commonly, acoustics refers to noise generation from mechanical components. Depending on the severity of the problem, the addition of silencers might be sufficient to reduce the sound pressure levels. Impellers of turbomachinery (for example, compressors, turbines and fans) are exposed to pressure loading caused by the generation of acoustic waves within the cascade. The amplitude of these waves can be amplified by acoustic resonance, which has been confirmed by experimental findings of F.L. Eisinger [3]. When the frequency of acoustic wave excitation matches with the structural natural frequencies of the impeller, high fatigue and vibrations are encountered, which can lead to structural failure of the compressor. This phenomenon is called an aeromechanical coincidence. The coupling between acoustics and structure is a different problem which is out of the scope of the present study. For oil and gas applications, such failures might lead to a shutdown of the complete facility. Therefore, aeroacoustic mechanisms play a key role in ensuring the operational availability of turbomachinery. This requires a profound understanding of physical mechanisms governing the acoustic resonances.

1.3. Selection of a research compressor

A centrifugal compressor stage with vaneless diffuser has been chosen for the aeroacoustic analysis. A 30/rev excitation was measured at the blade trailing edge during an experimental campaign corresponding to the sum of upstream and downstream blade rows. A pre-test modal analysis of the impeller was performed by Richards et al. [4] where all impeller natural modes were extracted up to 10000 Hz. Modes with larger shroud side disk were called F2 modes, and they were found to be associated with the 30/rev vibratory response measured during the experimental campaign. The stress distribution for the F2 mode is shown in Figure 2.

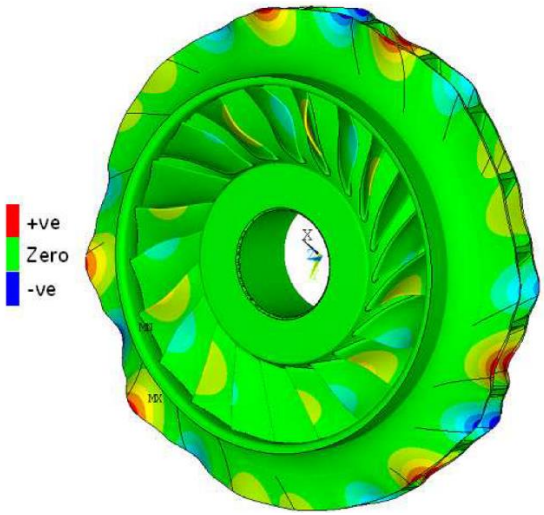

Figure 2 Impeller F2 mode shape [4].

Two reasons pointed to the hypothesis that acoustic resonances are involved. Firstly, it is known that blade row interactions are weak for low-pressure ratio stages. Therefore, there could be a resonance allowing unsteady pressure forcing (acoustics) to store energy [5]. Secondly, the tests also showed that 30/rev vibrational response was significantly lower when carbon dioxide (CO_2) was used as the working fluid at the same impeller rotational speed and flow coefficient. Gonzalez et al. [5] explored the scenario of acoustic resonances in the compressor flow path by executing an acoustic modal analysis. They concluded that the aeroacoustic excitation was amplified by acoustic resonances in case of nitrogen ($N_{2)}$. In the case of CO_2, the excitation did not have sufficient energy to cause sufficient loading on the impeller.

2 Background and motivation

2.1 Centrifugal compressor durability

Centrifugal compressor durability is the capability of a compressor to withstand operating loads over its prescribed life span [6]. Durability is a crucial design constraint which affects the safety and operational availability of the compressor. Materials used to manufacture centrifugal compressor stages exhibit an endurance limit, which represents the mean and alternating stress levels that the material can withstand for an indefinite period without encountering structural failure [6]. Fatigue margin is defined as the difference between peak operating stresses and the endurance limit. In the absence of vibratory stresses, the ultimate strength of the material is defined by the fatigue limit [6].

There are two common ways of mechanical failure in centrifugal compressors: low cycle fatigue and high cycle fatigue. Coffin [7] defines Low Cycle Fatigue (LCF) as the class of fracture in ductile materials where failure takes place in less than 10,000 cycles. LCF is caused by the regular starting and stopping as well as the temperature gradients and centrifugal stresses in the compressor structure during its lifetime [8]. High cycle fatigue (HCF) occurs when mechanical vibration induces significant vibratory stress in centrifugal compressor parts. Flow-induced HCF is the focus of this work as high-frequency vibrations were recorded in the experimental campaign for the chosen research compressor. Its definition and quantification are further elaborated in the following sections.

2.2 High Cycle Fatigue (HCF) definition

Konig et al. [2] provided a theoretical background of flow-induced excitation phenomena where the fluid exerts forces on confining structure through fluctuating pressure. Such forces can induce a vibratory response in the structure, which can lead to High Cycle Fatigue (HCF) when the number of stress cycles is higher than 10^5 [9]. HCF is a phenomenon that can result in catastrophic failure in turbomachinery. It occurs when vibratory stresses in a turbomachinery component exceed the material capability. Current design trends in centrifugal compressors demand increased performance and lighter weight, which requires smaller tip clearance between rotors and stators. Smaller tip clearance leads to increased blade-row interaction effects and hence, increases the severity of HCF problems. This has been confirmed by the experimental and numerical investigations of Wang et al. [10]. HCF problems are rare in case of low pressure ratio centrifugal compressors with vaneless diffusers [5]. Several excitation sources may contribute to a forced response. For example, flow distortion at impeller inlet due to flow from the upstream stage, vanes and pipe bends.

Primarily, two types of flow-induced HCF problems are encountered in centrifugal compressors: forced response, which is the vibratory response of a component to external aeroacoustic excitations (occurs at blade passing frequency of the rotor and its harmonics). For example, wakes from inlet guide vane are perceived as an unsteady flow field to an impeller located downstream. Such an interaction can lead to the generation of acoustic waves, which cause pressure loading (pressure pulsations) on the impeller structure [3]. The pressure pulsations consist of 1) fluctuating wall pressure, 2) plane waves, and 3) higher order acoustic modes [3]. Comparatively, higher order acoustic modes are the most common and efficient sources of impeller excitation due to their coincidence with the impeller structural modes [3]. The necessary conditions for such a coincidence are outlined in Section 2.6.

The second problem is flutter, which is caused when there is a dynamic instability during the interaction between an acoustic excitation and blade displacement. Flutter is also caused at frequencies close to the material eigenfrequencies [11]. Although analysing flutter is essential for the aeromechanical design of centrifugal compressor stages, it requires a coupled fluid-structure interaction computation. This is out of the scope of the present investigation; therefore, this topic is not pursued further.

2.3 Evaluation of impeller excitation due to HCF

The highly complex geometry of shrouded centrifugal compressors with three-dimensional blade profiles requires the implementation of numerical techniques for modal and stress analysis. Since HCF always points to high-frequency excitations that are close to impeller structural natural frequencies, modal analysis is required. Finite element analysis (FEA) is a state-of-the-art technique for such an analysis.

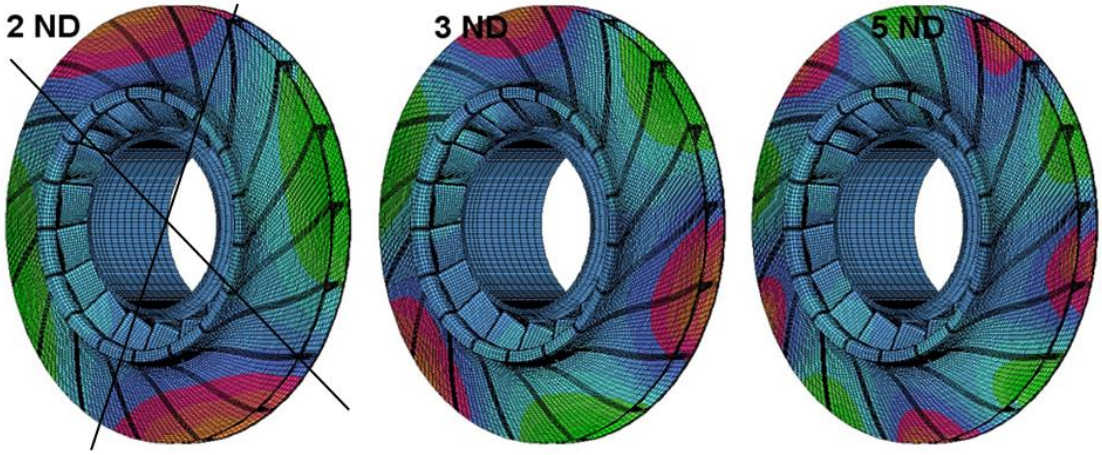

Figure 3 Mode shapes with 2, 3 and 5 Nodal Diameters (ND) [2].

In order to evaluate the severity of an aeromechanic coincidence, the frequencies, as well as mode shapes must be analysed. A typical FEA analysis provides information about both the natural frequency of the impeller vibration, and the associated distribution of vibratory stresses. The visual representation of such a distribution is called the mode shape. Figure 3 [2] illustrates structural mode shapes obtained from such an analysis for two, three and five nodal diameters with zero nodal circles. A nodal diameter or nodal circle is defined as a line with zero amplitude highlighting zones with zero stress amplitudes. This distinguishes zones with finite stress amplitudes. Figure 4 [12] illustrates the modes for one, two and three nodal diameters with one nodal circle. Red colour indicates motion into the paper and the blue colour indicates motion out of the paper [12].

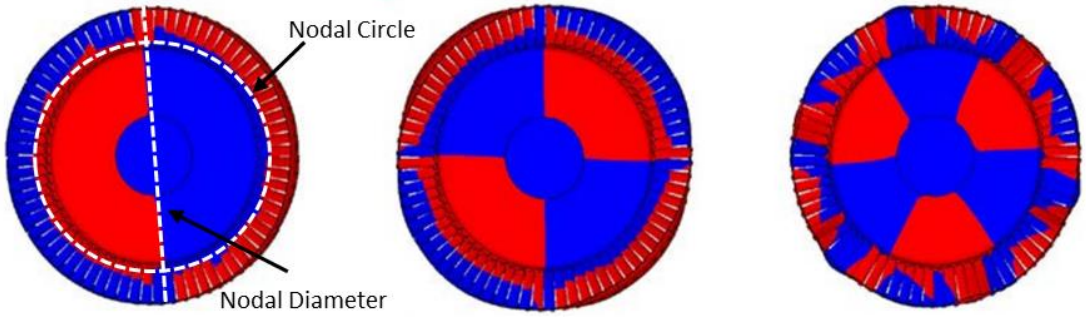

Figure 4 One, two and three nodal diameters and one nodal circle for a bladed disk configuration [12].

Results from the FEA analysis can also be used to plot the Campbell diagram. Campbell diagrams give an overview of possible vibratory excitations in a rotating system. A typical Cambell diagram is shown in Figure 5 [13]. The rotation speed of the engine is plotted on the

X-axis and compressor material eigenfrequencies are plotted on the Y-axis. The fan lines indicate engine-order. Engine order excitation is a periodic force, and its frequency depends on the rotational speed of the compressor. Such a study is necessary to determine if the structural eigenfrequency of the compressor is excited by the rotation frequency or its harmonics. For example, let us consider the second stage blade of a hypothetical compressor. From Figure 5, it is observed that a forcing frequency of 12000 rpm will excite the 200 Hz natural frequency of the blade [13].

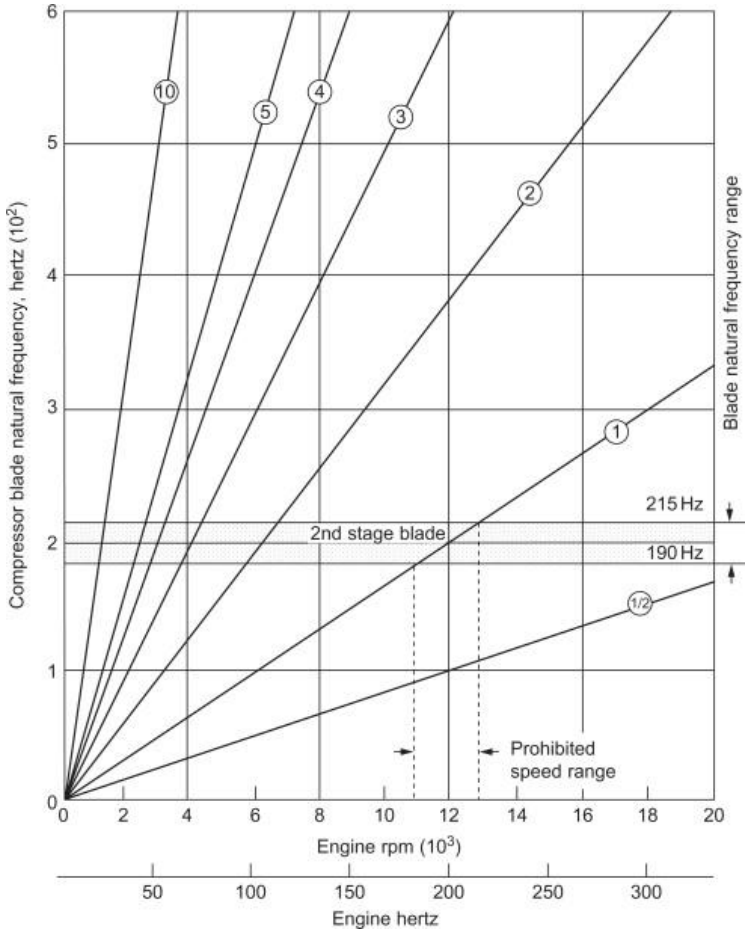

Figure 5 A typical Campbell diagram [13].

A Campbell diagram includes all impeller vibration modes and links them to the impeller rotation speed. Not every coincidence between impeller rotation speed and blade material eigenfrequency is likely to cause a vibratory response. Therefore, a Campbell diagram indicates more problems than actually exist. Furthermore, a typical Campbell diagram provides no information on the correlation between the structural and acoustic natural mode shapes. Due to these limitations, it is not possible to predict HCF during the design phase of the centrifugal compressor using Cambell diagrams alone.

Interference diagrams help overcome these limitations of Campbell diagrams. They provide information about which conditions are likely to cause aeromechanical coincidence by simultaneously taking into account the natural frequency, mode shapes, nodal diameters as well as forcing function [12]. This information can be obtained by combining results from an impeller modal analysis (to obtain structural modes) with the identification of aerodynamic excitation frequencies (to obtain acoustic modes). The interference diagram presented in Figure 6 [4] is a result of such a comprehensive analysis. The vertical axis represents the impeller excitation frequencies and the red vertical lines denote the relevant crossings where a forcing function is matching the impeller mode shape and also its natural frequency.

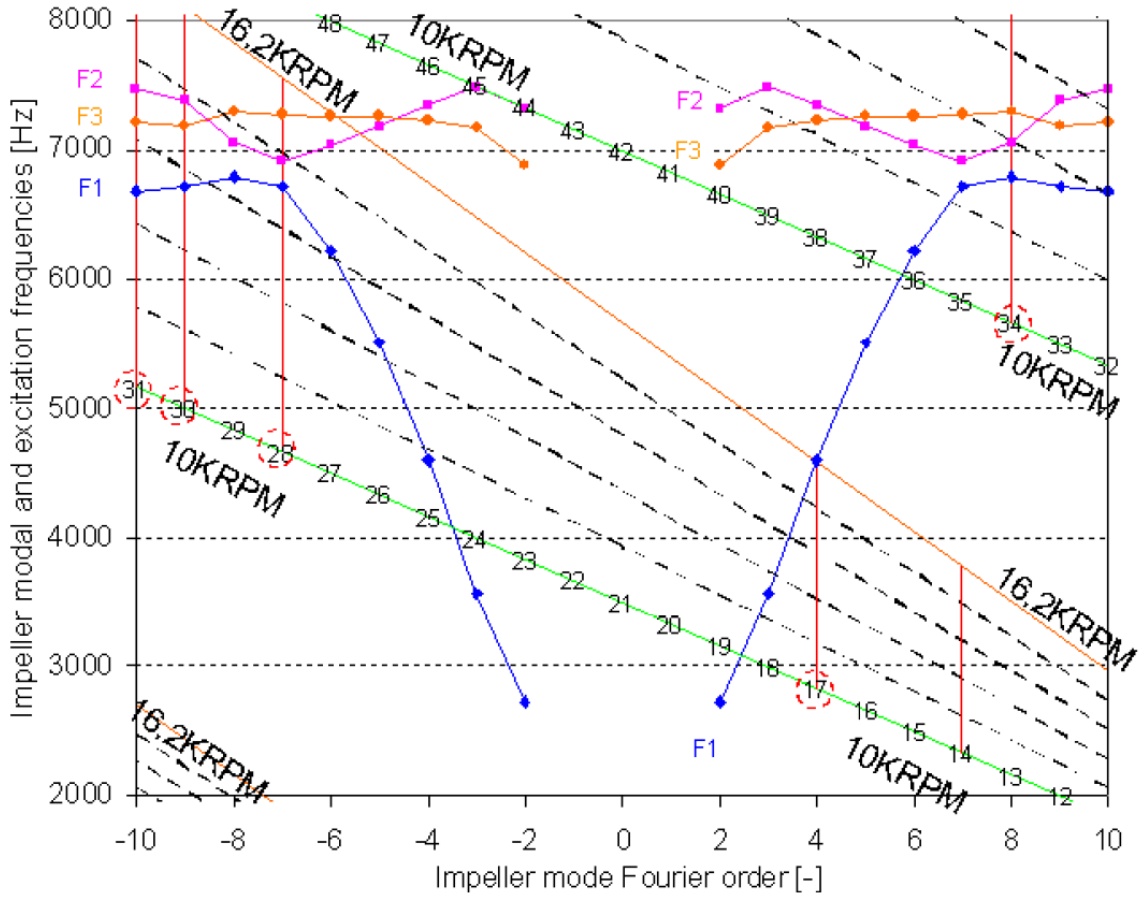

Figure 6 A typical stage interference diagram [4]. F1: Shroud vibration modes, F2: Disk outer diameter modes, F3: Blade first bending modes. Vertical lines indicate possible aeromechanic coincidences [4].

This method is usually sufficient to verify whether a given number of stator vanes can induce resonant vibrations in the impeller. In the case described in Figure 6, the compressor is fitted with a vaneless diffuser and 16 return channel vanes. Upstream set of de-swirl blade row is fitted with 14 vanes. Interference diagram shows that 17th harmonic could coincide with F1 (disk outer diameter) mode at 16200 rpm forcing function line while only 30th harmonic caused high vibratory response in the experiments conducted by Richards et al. [4]. Although this method represents the current state-of-the-art, it is insufficient to explain various instances of impeller failures [2].

2.4 Quantification of impeller excitation due to HCF

The maximum amplitude of vibratory structure response during resonance is given by [14]:

$$A_0 = \frac{|F(t)|}{2\omega^2 \zeta_{critical}} \tag{2.1}$$

where A_0 represents the vibratory response amplitude of the structure. $F(t)$ is the excitation amplitude, which can be described as source strength multiplied by the resonant amplification factor. $\zeta_{critical}$ is the critical damping ratio, which is defined as the sum of pressure dependent (or density dependent) aerodynamic damping and pressure independent material damping [15]:

$$\zeta_{modal}(\rho) = \zeta_{material} + \zeta_{aero}(\rho) \tag{2.2}$$

and ω represents the eigenfrequency of the system. Hence, in order to make a quantitative estimation of blade vibratory response, excitation forces and material damping properties must be quantified.

2.5 Fundamentals of flow-induced excitation phenomenon

Impeller fatigue quantification and assessing the resulting aeromechanic risk is a multi-disciplinary analysis process which involves the study of coupling between acoustic and vibration modes. Possible coincidences in impeller structural and acoustic eigenfrequencies must be checked against the excitation sources to detect aeromechanic coincidence early in the design phase. HCF failures usually occur due to cyclic stresses, which constitute following building blocks:

1) Excitation source
2) Acoustic resonances
3) Mechanical resonances

Excitation sources that lead to forces on confining structure can be divided into two categories: acoustic, which is associated with the compressibility of fluid, and hydrodynamic (refer Figure 7) [2]. Pressure fluctuations can be both discrete and broadband depending on the nature of periodic events in the flow field. Both can lead to resonance conditions by exciting the acoustic eigenmodes. In a special case where acoustic eigenmodes are excited to high amplitudes, the classical approach of linear acoustics is no longer valid [2]. A simple example of such a phenomenon is observed in a trombone, where the pressure at the exit of the horn shows very sharp peaks. In such a scenario, the fluid system is fully coupled and acoustic modes cannot be decoupled from the entropic modes and vorticity.

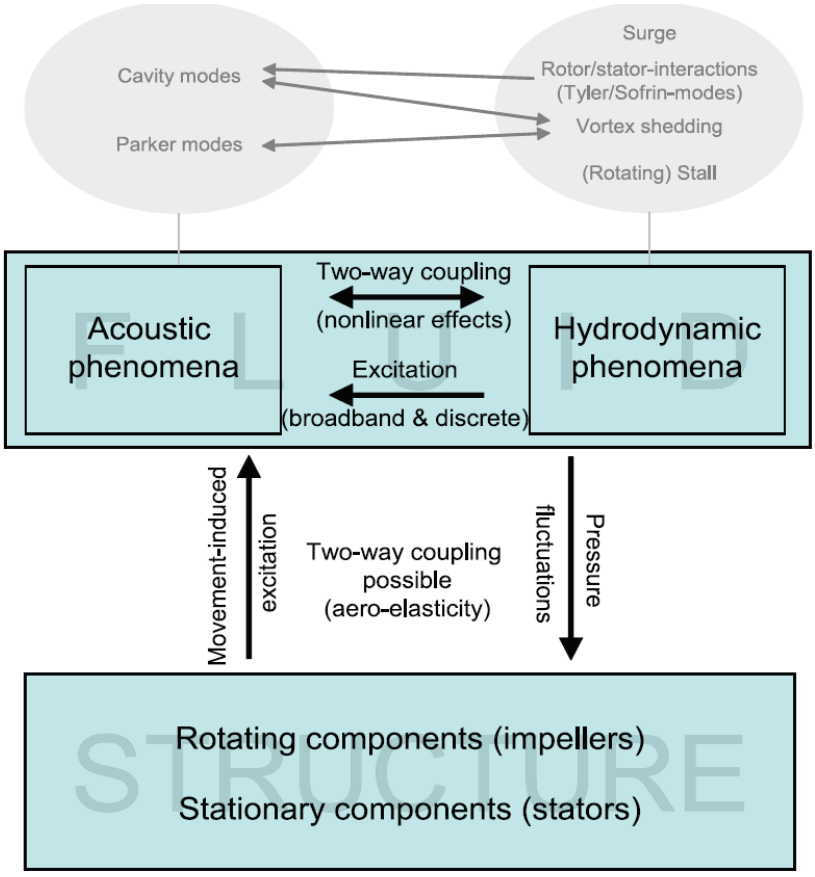

Figure 7 Fluid-Structure interaction mechanisms [2].

Excitation sources, when amplified by acoustic resonance, may induce cycle stresses in the structure that can cause vibrations. When the vibration amplitudes are high enough, feedback on the fluid will occur (movement-induced excitation), which results in complex non-linearities in the system [2]. Such a strong feedback loop between fluid and structure caused blade failure is reported in [16] where the acoustic field around the fan induced strong impeller vibratory response which in turn led to variation in leakage flow rate due to change in seal gap width. Fluid-structure interactions are generally expected to be dominant at high operating pressures when the gas density is high, resulting in a stronger coupling between flow and the impeller structure. Konig et al. [2] state that a two-way coupling (fluid-structure interaction) as discussed above, is not a necessary condition for a strong vibratory response leading to structural failure. In the research compressor chosen for the present investigation, it is observed that low-pressure compressor stages can also show large structural vibrations when certain flow conditions are satisfied. Due to the low operating pressure of the chosen research compressor, the scenario of a two-way coupling is not explored. The acoustic analysis of the research compressor performed by Gonzalez et al. [5] pointed to acoustic standing waves in the compressor flow path which coincide in frequency and mode shape with at least two mechanical natural modes [17]. In case of such behaviour, the cause-effect diagram is presented in Figure 8.

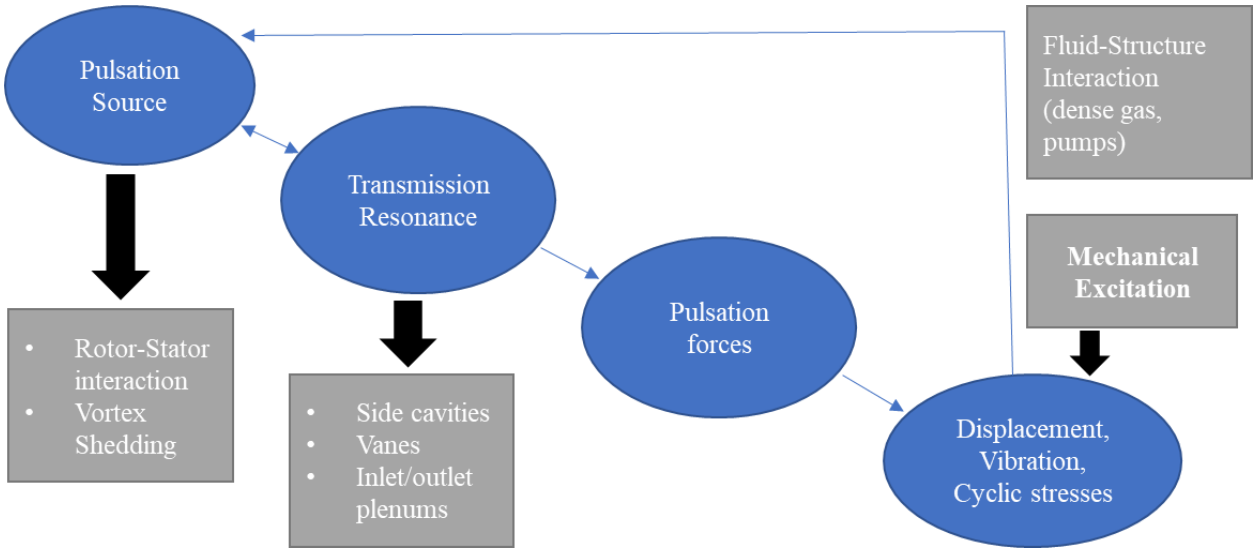

Figure 8 Pulsation-induced vibrations inside centrifugal compressors [5].

2.6 Acoustic resonances in centrifugal compressors

Acoustic resonances might amplify excitation sources causing noise emissions and in severe cases, structural failure of the centrifugal compressor. The presence of many cavities and an inherently unsteady flow field in centrifugal compressors makes these machines highly prone to acoustic resonances. Due to their confined volumes, cavities exhibit characteristic acoustic eigenfrequencies [2]. Highly unsteady and complex flow in centrifugal compressors poses a variety of excitation sources such as Tyler-Sofrin modes and vortex shedding. In the case of a coincidence between an excitation source frequency and the acoustic eigenfrequency of one of the cavities, advanced understanding of the relevant physical mechanisms is necessary to classify the severity of the problem [2]. According to [17], the following conditions must be met for an acoustic mode to be excited:

1) The frequency of the excitation source matches the acoustic eigenfrequency of compressor side-cavities, vanes and inlet/outlet plenums.
2) The circumferential mode order (number of nodal diameters) of the excitation source (for example Tyler-Sofrin Mode) is equal to that of acoustic mode.

When both conditions are satisfied, the strength of the resulting coupling depends upon the radial distribution of mode shapes. Such a coupling mechanism is illustrated in Figure 9 [2].

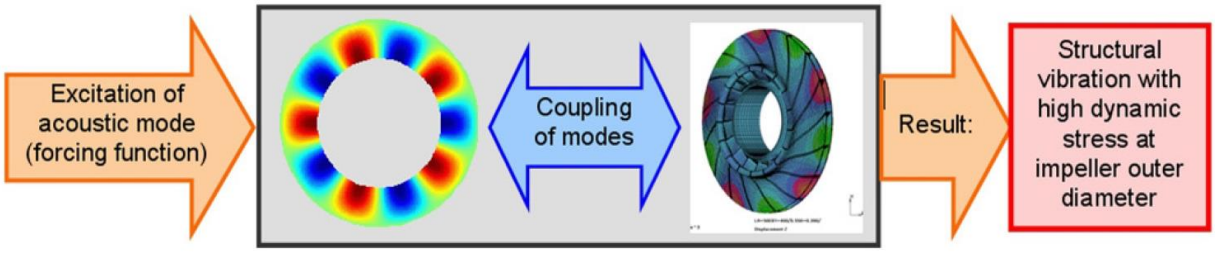

Figure 9 Principle of Mode-Coupling mechanism [2].

In the example shown above, acoustic and structural modes are characterised by 5 nodal diameters. An aeromechanical coincidence may occur when an acoustic mode is excited by a forcing function and its frequency as well as mode shape matches with the structural eigen-mode. One relevant excitation source constitutes Tyler-Sofrin modes resulting from rotor-stator interaction. This will be addressed in more detail in Section 2.7.

Other flow phenomena like vortex shedding and inlet flow distortion can also act as a source of impeller excitation [14]. Therefore, in the process of analysing acoustic resonance conditions, the first step should be the calculation of acoustic eigenfrequencies for relevant cavities [2]. The next step is to estimate aerodynamic forcing function and damping to eliminate the most critical conditions with respect to aeromechanical coincidence. In cases where such coincidences cannot be avoided, resulting in blade vibration amplitudes and the resulting stress must be quantified to ensure compressor reliability.

2.7 Tyler and Sofrin rule for Rotor-Stator Interaction

The majority of unsteady flow structures in centrifugal compressors are caused by rotor-stator interaction, resulting in discrete blade passing frequency (BPF) tones [18]. This causes the generation of acoustic waves. Spatial periodicity of these waves is governed by the location of blade rows. This unsteady interaction results in a spatial and temporal fluctuation in fluid pressure which can be decomposed into Fourier modes, $\hat{P}_{mn}$ by following equation [4]:

$$p(\theta,t) = \sum_{n=0}^{\infty}\sum_{m=-\infty}^{\infty}\hat{P}_{mn}\ e^{i(m\theta-n2\pi ft)} \tag{2.3}$$

where circumferential coordinate and mode number are denoted as θ and *m* respectively. Blade passing frequency is denoted by *f*. In the work on axial compressor aeroacoustics, Tyler and Sofrin [19] derived an empirical relationship for determining modes numbers resulting from rotor-stator interaction. This relationship is given by [4]:

$$m = nB \mp kV, \quad n,k \in \{0,1,2,\dots\} \tag{2.4}$$

For the chosen research compressor, *B* and *V* represent impeller and upstream de-swirl vane blade counts respectively and *n* and *k* represent the impeller blade passing frequency (BPF) and vane passing frequency (VPF) harmonics respectively. The compressor has three sets of blade rows. When an acoustic wave with mode number *m*, obtained from equation 2.4 interacts with downstream vanes, it might be scattered or reflected spatially into various circumferential modes. Therefore, a modified version of equation 2.4 can be obtained which gives the scattered mode number m' [4]:

$$m' = m \mp k'V' \quad k' \in \{0,1,2,\dots\} \tag{2.5}$$

where the downstream de-swirl vane-blade count is denoted by V' and k' represents the respective VPF.

The next important step in the project is to compute the impeller loading caused by the rotor-stator interaction. Pressure loads acting on the impeller can be obtained by sampling pressure probe data across various locations in the computational domain. Discrete Fourier Transform (DFT) technique will be used to obtain spectra of direct pressure measurements from CFD. It is given by the following equation [4]:

$$\hat{P}_n = \frac{1}{N}\sum_{k=0}^{N-1} p(t_k) e^{-i(\frac{2\pi kn}{N})} \quad (2.6)$$

where *P* denotes unsteady pressure obtained from CFD data sampled at k^{th} time step. $\hat{P}_n$ represents the complex Fourier coefficient corresponding to n^{th} frequency harmonic of BPF.

2.8 Previous work

Extensive research has been conducted on turbomachinery aeromechanics particularly for axial compressors for large engines; whereas, considerably fewer resources and research efforts have been devoted to research and development of centrifugal compressors [20]. Tyler and Sofrin [19] investigated rotor-stator interaction mechanisms for an axial compressor.The study was aimed at finding the root cause for noise generation, however, such an interaction and the resultant rotating pressure profiles called the Tyler-Sofrin Modes (TSMs) may contribute as an excitation source characterised by the blade passing frequency. This study was followed by a number of publications focusing on axial compressor noise [21-28] but no significant research efforts were directed to centrifugal compressor stages.

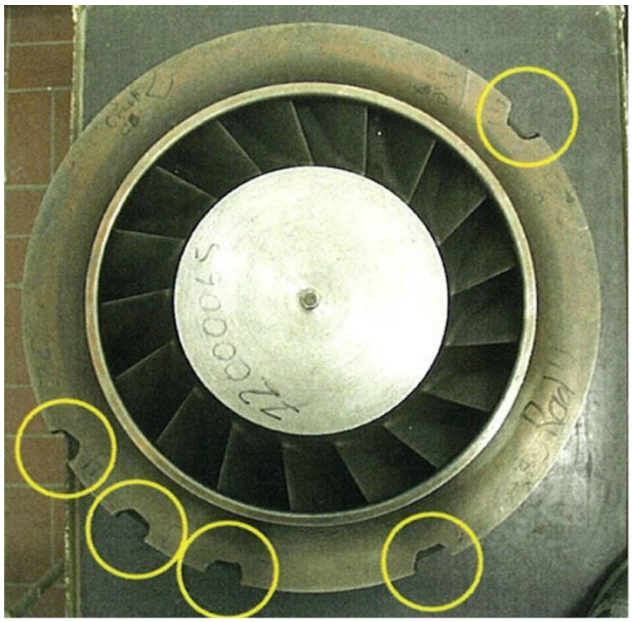

Figure 10 Fatigue Failure on the Shroud disk of a centrifugal compressor impeller [2].

A small number of research works have been dedicated to the study of unsteady processes in the centrifugal compressor stages, aimed at finding the root cause of the impeller failure. Most of the work has been done by Original Equipment Manufacturers (OEMs). [2], [17], [29] have made a significant contribution to this domain. The acoustic phenomenon in the side cavities has been the main focus of attention in these works. It has been proven that acoustic

excitation of resonant modes inside cavities can lead to forced excitation of impeller vibrations to dangerous levels. Sven et al. [2] performed root cause analysis of the structural failure of the impeller wheel shown in Figure 10. After 22,000 hours of operation, a compressor assembly was disassembled where fatigue failure on the last stage of the compressor was observed. Five coin-sized pieces, spaced equally around the circumference, broke from the shroud disk [2].

Experimental research on forced response analysis is a multidisciplinary process that requires the use of several measurement techniques. In order to quantify the forced response parameters given in Equation 2.1, a combination of techniques like modal testing, forcing function measurements, blade response measurements and flow field measurements must be performed. Modal testing provides an insight to blade modal shapes and eigenfrequencies during vibration. For a typical centrifugal compressor analysis, the impeller is excited by mechanical, electrical or acoustic actuator [14]. Measuring the blade surface unsteady pressure is one of the most challenging experimental tasks. This requires unsteady pressure sensors to be mounted on rotating blade surfaces. The current state of the art pressure sensors are incapable of withstanding such harsh environments. Therefore, experimental techniques alone are incapable of quantifying the unsteady pressure loading on the impeller blades. Computational tools are capable of overcoming these limitations.

Computational methods have proved to be cost-effective and reliable tools for the detection of HCF in the preliminary phase of the design process [11]. Numerical analysis can enable understanding of flow physics governing the root cause and amplitudes of unsteady loading on blades and vanes, which can aid in identifying possible aeromechanical coincidences. By developing a numerical model capable of predicting the time-dependent flow field inside the compressor, the forcing function can be obtained which is required for vibratory response analysis. Computational analysis of forced response in centrifugal compressors focuses on three main objectives that must be met in order to ensure a safe design. Firstly, modal parameters, i.e. structural eigenfrequencies and modal shapes, must be quantified. Secondly, forcing function, i.e. pressure loading on the impeller structure must be quantified for critical conditions with respect to an aeromechanical coincidence. Thirdly, static stresses acting on the blade and disk must be computed. All of these objectives require the use of computational tools. However, the increasing availability of computational power might allow the merging of these objectives. Two approaches have been found in the literature. Firstly, a coupled fluid-structure interaction calculation can be performed to compute bidirectional interaction. This needs an enormous amount of computational resources, therefore, a decoupled unidirectional approach is commonly used to quantify blade loading in centrifugal compressors. Hence, the aerodynamic analysis is performed independently of structural analysis [14]. Examples of fully coupled or decoupled simulations can be found in [30-35].

For the state-of-the-art evaluation of forced response analysis in centrifugal compressors, shrouded centrifugal compressors should be distinguished from semi-open centrifugal compressors [2]. The sensitivity to aero-mechanical excitation and the resulting failure is highest for axial compressor impellers and lowest for shrouded centrifugal impellers. Available excitation models and analysis tools are directly proportional to this sensitivity. Following sections contain a review of published literature on the analysis of forced excitation in centrifugal compressors.

2.8.1 Excitation sources in centrifugal compressors

The relative motion of blade surfaces is the root cause of flow unsteadiness in the centrifugal compressors [22]. Steady relative flow with a tangential velocity gradient in blade passage produces an unsteady flow when observed in the absolute frame of reference [36]. Absolute frame of reference in centrifugal compressors refers to the stator frame of reference (non-rotating) while the relative frame of reference is the impeller frame of reference (rotating).

Boundary layers on the blade surfaces create wake lattices that are mixed and transported throughout the machine generating more flow unsteadiness [22]. These steady flow features can act as sources of blade excitation when amplified by an acoustic resonance within the compressor. Therefore, accurate resolution of these flow features is essential to analyse the physics as well as the severity of aeromechanic coincidence.

2.8.1.1 Rotor-stator interaction (Tyler-Sofrin modes)

As described in Section 2.7, the majority of unsteady flow structures in centrifugal compressors are harmonic, originating from blade passing frequency (BPF). Consequently, they are the root cause of many fatigue-induced failures encountered in the impellers. Two types of interactions can occur between rotor and stator in centrifugal compressors. First is potential interaction, which occurs when the blade rows are close to each other. In cases where the distance is significant, an aeroacoustic interaction can occur where acoustic waves exiting the rotor interact with the stator.

Franke et al. [37] studied mode shapes emanating from the rotor-stator interaction for the case of a radial turbine. In an experimental campaign, they recorded unsteady pressure measurements in the spiral case and the draft tube. A study of temporal and spatial variation of pressure distributions enabled them to visualise mode shapes. They adopted an addition tool called Operating Deflection Shape (ODS) [37] technique to visualise complex pressure distributions. This enabled a more direct evaluation of causation. Unsteady pressure at a point may be the result of unsteadiness caused by different physical phenomena. Hence, experimental measurements alone might not be sufficient to distinguish effects like acoustic wave reflections and stochastic flow-induced turbulence [37].

Zemp et al. [38] used a framework of numerical and experimental techniques to quantify forced vibratory response of impeller blades in a centrifugal compressor. They pointed to the potential interaction between the impeller and vaned diffuser as the root cause of high impeller excitation. Stage performance estimations from steady fluid flow simulations were compared with experimental data to validate the simulation strategy. They performed unsteady flow simulations to study the effects of the compressor operating point as well as tip clearance size on the impeller loading amplitudes. Blade surface pressure measurements from unsteady simulations were analysed to study pressure loading in the streamwise direction. Figure 11 illustrates the blade forcing amplitudes for three resonant crossings (modes 6-8), and two impeller-diffuser configurations. It is observed that large tip clearance causes peak pressure loading at 93% of the blade length. This is different from small gap configuration which caused peak blade loading amplitudes at 98% of the blade length. Blade loading distribution for different operating conditions (exciting different resonant modes) provided valuable insights into the severity of impeller excitation. However, loading amplitudes were not validated with experiments. They concluded that it is impossible to quantify vibratory stress response from an unsteady load calculation by CFD as the structural response is governed by mode-dependent aerodynamic and material damping properties.

Smyte [11] and Villanueva [39] conducted experimental campaigns to study rotor-stator interaction in two nearly identical centrifugal compressor stages with a tip clearance variation of 0.55% of the impeller radius. It was found that with only a slight difference in tip clearance the resulting amplitude of blade stress was about a factor of two larger in comparison to the configuration with larger tip clearance. Villanueva [39] also studied the effects of varying the impeller radius and found a correlation between the increase in unsteadiness at diffuser leading edge and impeller trailing edge with a decrease in impeller radius. This corroborated the findings of Zemp et al. [38].

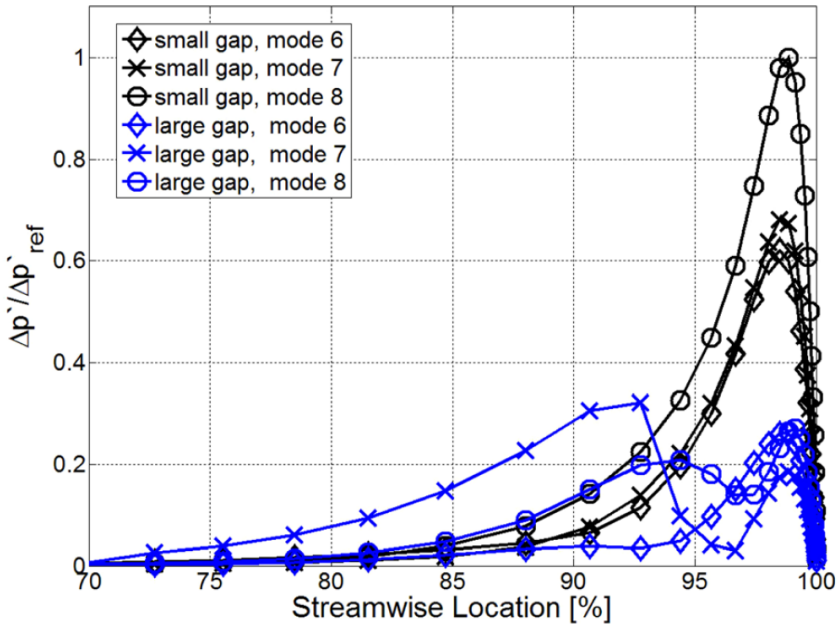

Figure 11 Unsteady blade pressure amplitude computed from CFD, near stall operating point [38].

Excitation mechanisms caused by rotor-stator interaction were studied by Gallier [40]. In an experimental campaign, data from wall mounted unsteady pressure sensors, and Particle Image Velocimetry (PIV) was used to study velocity and pressure field in the vane-less gap between impeller exit and vanes at diffuser inlet. The interaction of impeller wakes with diffuser vanes caused high excitation amplitudes at impeller blade trailing edge. The transient flow incidence angle at the diffuser vane caused transient vane loading, resulting in the generation of pressure waves propagating upstream and downstream.

Petry et al. [2], [17], [41], [42] have made a remarkable contribution towards achieving a comprehensive understanding of underlying physics governing the rotor-stator interaction in centrifugal compressors. In [41], Petry et al. focused on impeller excitation due to rotor-stator interaction. High noise and vibratory response were measured when acoustic eigenmodes in the centrifugal compressor cavities were excited by Tyler-Sofrin modes (TSMs). In another study, Petry et al. [2] concluded that predicting acoustic cavity modes in complex geometries like three-dimensional shrouded impellers requires high fidelity numerical solvers and well-resolved grids. Later, Petry et al. [17] investigated the aeroacoustic excitation mechanisms in a full centrifugal stage. The interaction between Tyler-Sofrin modes (TSMs) and side cavity acoustic modes was studied with the help of experimental and numerical investigations. They developed an excitation model capable of predicting resonance between the TSMs and acoustic eigenmodes. They also emphasised the relevance of fluid core rotation for such a prediction model. Therefore, cavity flow must be well resolved in order to estimate the correct frequency and amplitude of the impeller excitation resulting from Tyler-Sofrin modes.

Building upon their work from 2010, Petry et al. [42] addressed the effects of swirling fluid flow in the compressor side-cavities on the acoustic resonances by independently measuring the circumferential flow Mach numbers and acoustic resonances. Contrary to their findings in [17], they found that pressure peaks were mainly caused due to the acoustic resonance of side cavity eigenmodes which were localized to only one of the side cavities. However, numerical simulations on the compressor stage given in [17] showed the coupled behaviour of the two cavities. Therefore, more numerical investigations are required to validate these conflicting findings.

Walton et al. [20] developed a simplified model for capturing impeller forcing function generated by impeller-diffuser interaction at resonance. They measured splitter blade surface pressure fluctuations for two mode shapes based on the Campbell diagram. The pressure loading amplitudes and stage performance could not be validated with experimental data due to the usage of a modified blade count. This was done to approximate circumferential passage to passage variation of the flow field in the complete impeller.

Vogel et al. [43] studied flow features in the vaned diffuser of a centrifugal compressor using a framework of experiments and numerical simulations. They simulated a 360 degree model of the compressor wheel and studied the effects of using non-reflective boundary conditions. They found that CFD results overpredicted the amplitude of pressure fluctuations by 62% in the case of reflective boundary conditions. Therefore, acoustic treatment on domain boundaries is crucial for capturing turbomachinery aeroacoustics.

Gould [44], Lusardi [45] and Leng et al. [46] showed that the unsteady flow field in the vaneless space generates acoustic waves propagating upstream and downstream of the flow. This corroborates findings of Gallier [40]. Gould et al. [6] implemented numerical techniques to characterise unsteady loading on impeller blades in centrifugal compressors. They identified three key parameters that control the extent and level of the unsteady blade loading: stage loading, impeller-diffuser gap (tip clearance), and the relative Mach number in the compressor passage (speed of sound effects). The impeller-diffuser gap was shown to control the unsteady peak loading on the impeller blades. Stage loading was observed to impact the upstream attenuation of the loading. The relative Mach number was shown to impact the chord-wise distribution of unsteady pressure forcing on the impeller blade.

2.8.1.2 Circumferentially non-uniform flow at the impeller inlet

Circumferential non-uniformity in the inlet flow can act as a source of impeller excitation when amplified by acoustic resonance. Haupt et al. [47] found that it does not cause significant impeller vibration amplitudes, while others contradict these findings [48], [49], and [50]. These works are discussed in this section.

Haupt et al. [47] implemented a framework of experimental and numerical techniques to investigate the root cause of a high-frequency impeller excitation. They pointed to multiple excitation sources including inlet flow distortion, rotating stall and rotor-stator interaction. The analysis of acoustic eigenmodes in the compressor cavities suggested that the acoustic resonance did not amplify inlet flow distortion and therefore, did not cause significant blade vibration amplitudes. This corroborates previous findings on similar machines given in [46], [47], and [48]. They found that the potential interaction of diffuser vanes caused significant vibration amplitudes. In the case of a rotating stall, vaned diffuser caused higher vibratory amplitude in impeller blades compared to the vaneless configuration. Laser-based optical measurements of blade rotation at resonant conditions depicted that all blades vibrated with similar mode shapes but different amplitudes. This observation was attributed to mistuning effects in the compressor.

Salzle [48] performed forced response measurements to investigate the root cause and amplitude of the impeller harmonic excitation. The analysis pointed to a spiral-type volute as the source of the high cycle fatigue failure. Flow recirculation resulting from the volute caused a non-homogeneous flow profile at the impeller inlet. The unsteady pressure measurements inside the rotor were found to be dependent on the stage mass flow rate. The findings suggested that flow distortion upstream of the impeller can act as a source of forced blade excitation. This has been corroborated by the findings of Jin [49] where the magnitude and the root cause of the excitation responsible for a forced response in a centrifugal compressor were studied. The blade vibratory response was attributed to flow recirculation inside the shroud. The resulting unsteady pressure field affected the blade vibration and was found to

be dependent on the flow incidence angle at the impeller inlet. Unlike the findings of Salzle [48], a two-way coupling was found between blade vibration and the unsteady pressure field. This resulted in a high resonant response, which exceeded tolerable stress amplitudes for the impeller structure. This mechanism is dominant in high-pressure centrifugal compressors with thin blades and vaned diffuser. In such cases, pulsating flow at the inlet of the compressor was found to cause unsafe blade vibratory amplitudes.

Abhari et al. [50] performed unsteady CFD simulations to investigate the root cause of blade vibratory response, which pointed to unsteady flow generated by grid installations upstream of the impeller. In another publication, Abhari et al. [51] performed the experimental investigation of forced response in a centrifugal compressor with inlet distortion. They showed that excitation order due to inlet flow distortion is of comparable magnitude to the second and third harmonic of blade passing frequency. Ecker and Ni [16] also studied the case where a two-way coupling caused blade failure in a high-pressure centrifugal compressor system. Eisinger and Sullivan [52] performed a root cause analysis on a high cycle fatigue failure encountered in a centrifugal fan impeller blade. They also pointed to a structural-acoustic coupling as the root cause for the vibrational problem.

Resonant blade excitation in a centrifugal compressor for turbocharging applications was studied by Kammerer [53]. He found out that distortion screen at the inlet of the compressor caused flow distortion resulting in a resonant vibratory response in the impeller structure. The circumferential non-uniformity of the inlet flow was changed by varying distortion screen porosity. A circumferential non-uniformity of 1% - 4% in the inlet pressure caused a dangerously high forced response.

In summary, non-uniformity in inlet flow can act as a source of resonant blade excitation only in the case of high-pressure centrifugal compressors. Two-Way coupling between fluid and structure occurs at high operating pressures when the density of the working medium is high. For low-pressure compressor systems, the source strength is not high enough to excite the impeller structure. Furthermore, the frequency of such excitation is usually low compared to acoustic and structural natural frequencies.

2.8.1.3 Vortex shedding as a source of impeller excitation

Vortex shedding is referred to as oscillating fluid flow past a bluff body [54]. It usually occurs at the trailing edge of transonic centrifugal compressor blades [54]. Other bluff bodies, for example, struts at compressor inlets have also been shown to shed vortices [55].

Unlike Tyler-Sofrin modes (generated due to rotor-stator interaction), it is hard to attribute a discrete mode shape, pressure pattern or a frequency to vortex shedding in centrifugal compressors [2]. In most practical applications, factors like local flow unsteadiness, acoustic feedback, inter-blade interactions alter vortex shedding frequency [55]. This causes high uncertainties in the quantification of Strouhal number [54]. Vortex shedding is the root cause of high impeller excitations in the following cases.

Ziada et al. [56], investigated acoustic resonance in the inlet scroll of a turbo compressor which caused a high vibratory response in the impeller blades. They pointed to a complex interaction between vortex shedding and a standing wave inside the ring chamber as the root cause. They noticed that as the compressor mass flow rate increases, ‘lock-in’ occurs where acoustic modes control the vortex shedding frequency. ‘Lock-in’ is caused due to acoustic-feedback, where acoustics effects the flow and vice-versa.

Parker et al. conducted a series of studies [25-28] and [57] on a less researched excitation source in turbomachinery called Parker Modes. It was shown that vortex shedding from impeller blades excited acoustic modes between the blades. However, this occurred only for

high blade chord-pitch ratios, which are usually found in axial turbomachinery. Therefore, no further literature will be discussed on this subject

2.8.1.4 Other sources of impeller excitation

Some of the uncommon and less researched sources of impeller excitation in centrifugal compressors include pulsating inlet flow, rotor instability, instability of bearings and broadband pressure fluctuations caused due to rotor-stator interaction.

Dickmann et al. [35] implemented experimental and numerical methods to study impeller blade excitation. Their root cause analysis pointed to flow recirculation and pulsation caused by the bleed system where the flow from shroud exit is re-injected to the impeller. It was demonstrated that the vibratory response of the blades varied significantly based on the compressor operating point. Structural response measurements were obtained from a numerical investigation, enabling visualisation and quantification of unsteady flow mechanisms that caused resonant excitation.

2.8.2 Discussions using a CFD based approach in the literature

Turbomachinery flows are inherently unsteady. The unsteady flow phenomena play a critical role in both the performance and the safe operation of the machine. These flow features must be accurately modelled to assess the root cause as well as the severity of impeller excitation. The majority of these unsteady flow structures are harmonic, originating from blade passing frequency (BPF). However, wakes or any transient external force might happen on a different time scale [18].

Tucker [58] categorises computational modelling hierarchy according to fidelity. Figure 12 [58] classifies various models based on fidelity. There is a trade-off between accuracy and the required amount of computational resources.

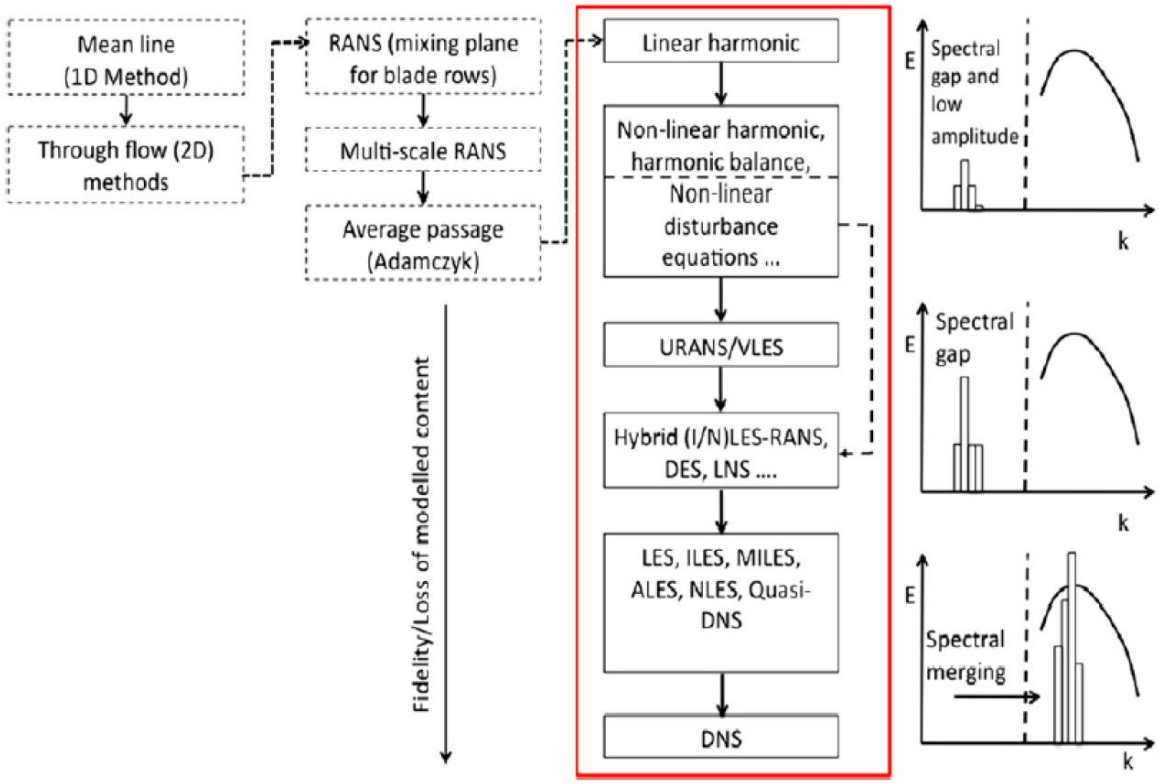

Figure 12 CFD Modeling hierarchy based on fidelity [58].

Earlier, mixing-plane RANS computations were incorporated to compute the 3D flow field in turbomachinery. This approach assumes a plane between blade rows allowing not just spanwise, but also circumferential averaging of flow variables [18]. This simplified approach allows reasonable global performance parameters, but all of the unsteady effects are not modelled. Due to this simplification, usually, modelling a single blade per row is enough instead of simulating the same pitch angle. This makes mixing-plane approach highly computationally efficient. Another method of obtaining a steady-state solution is a frozen rotor approach. This allows calculation of flow variables for a “fixed rotor” but not mixed [18]. This approach is usually used to initialise the flow solution for a transient calculation [59]. The inability to model the unsteady flow phenomenon makes this technique infeasible for the present investigation.

Non-linear harmonic and harmonic balance methods are based on the assumption that flow variables change periodically at BPF at the phase-shifted boundaries. Therefore, flow variables are solved in the frequency domain only at certain harmonics by applying a Fourier Transformation [60]. Phase-shifted methods are also based on using the same periodic boundary conditions and solving them in the time domain. It is seen from Figure 12 that they offer an intermediate fidelity between steady-state RANS computations and unsteady RANS computations as they can resolve the unsteady phenomenon only related to BPF while neglecting the others. In terms of computational efficiency, they offer less computationally expensive solutions in comparison to sliding mesh unsteady RANS simulations [18]. Since this method is unable to resolve unsteady features apart from BPF, it can not be used in the present analysis. Furthermore, this method is unable to account for acoustic resonances of the flow path due to the simplification of modelling just a sector of the full compressor wheel.

The sliding mesh RANS computations are unsteady and require a fine grid to capture unsteady features. In most practical cases, blade rows do not have common denominators to avoid flow instabilities; therefore, ‘original design’ cannot be scaled to achieve the periodicity. A full blade row model is possible in such cases but is very computationally expensive. Therefore, in most of the cases, the number of blades is scaled down to find a common denominator and model the periodicity [18]. Such cases often lead to errors which are due to scaling. The feasibility of this approach for prediction and analysis of aeromechanical coincidence in centrifugal machines was explored by Mansour et al. [61]. They implemented a framework of CFD and FEA codes to compute mean strain values on impeller blades. Due to the inability of code to allow the implementation of phase-lagged boundary conditions, a modified blade count was used to avoid modelling the entire wheel. Since then, many researchers have performed time-resolved computations of the flow field inside a centrifugal compressor. For aeroacoustics, unsteady flow features like impeller wake and vortex shedding must be modelled [62]. Furthermore, fine spatial discretisation is necessary to resolve the frequency and mode shapes for higher modes [63]. This imposes strict requirements in terms of computational costs.

Modelling simplifications like using a modified blade count, excluding cavity and leakage flows do not have a significant impact on centrifugal compressor performance predictions. However, they often result in high inaccuracies in the prediction of impeller forcing function amplitudes [64]. Smyte et al. [11] performed a comparative study on two similar centrifugal compressor configurations, one of which failed due to the HCF of aeromechanic nature. They performed a numerical investigation on a simplified model of the compressor stage, which excluded leakage flows, side cavities and the effects of de-swirl vanes. Therefore, unsteady pressure amplitudes could not be validated with experimental data. It was hypothesized that the unsteady pressure distribution resulting from variation in time-averaged incidence angle at diffuser inlet was the excitation source for the forced response. Satish et al. [64] compared time-averaged data from CFD analysis with unsteady probe data from experiments. They found a substantial improvement in computational accuracy by modelling full compressor geometry, including the leakage flows. For the current investigation, modelling the entire

compressor wheel is necessary to account for acoustic resonances which are dependent on side-cavity fluid dynamics and volume.

Richards et al. [65] studied the effects of hub and shroud cavities on the modal forcing on the impeller blades. In a three-step approach, they extracted the 30/rev excitation to the impeller from a full wheel (without side-cavities) URANS CFD simulation as described in [4]. In the next step, they added hub and shroud cavities to the computational domain. Then, they computed the steady flow field inside the compressor including the cavities by incorporating a multi-blade row mixing plane calculation of the flow path described in [4]. Finally, they performed a linearised forced response analysis of the compressor using the acoustic forcing function obtained from CFD simulation described in [4]. Using the linearised model, they performed frequency sweeps on the flow domain to identify cavity resonant frequencies. Their root cause analysis pointed to an aeroacoustic interaction between compressor aerodynamics and acoustic resonance of the flow path. Although their method is computationally efficient and representative of the current state-of-the-art, the exclusion of side cavities from the CFD model neglected the effects of a two-way coupling between hydrodynamics and acoustics. This adversely affects the prediction of impeller forcing amplitudes [64].

The current investigation will build upon the work done in [13], [16] and [65]. Instead of a two-step approach as discussed above, cavities would be simulated in a one-step calculation. This would overcome the limitations posed due to neglecting acoustic-feedback phenomenon. The unsteady CFD domain will comprise of impeller, side-cavities and adjacent blade rows (upstream pre-swirl and downstream return-channel vanes). For the first time, stage performance and unsteady pressure measurements from CFD will be validated with experimental data for a centrifugal compressor operating at conditions of acoustic resonance. It is worth mentioning here that a CFD calculation is capable of simulating the physics of Tyler/Sofrin-modes and the acoustic eigenfrequencies as the Helmholtz equation follows the governing equation of fluid mechanics [2]. The process will lead to the development of a simulation strategy capable of quantifying aero-acoustic forcing in centrifugal compressors. Finally, the pros the cons of the simulation approach will be addressed and recommendations will be given for future research.

2.8.3 Lattice-Boltzmann method based approach for rotor-stator interactions

From a review of published literature, a scarcity of simulation strategies capable of accurately predicting blade loading in a realistic centrifugal compressor geometry operating at resonant conditions has been observed. Simplified simulation models have been able to provide valuable insights into the impeller excitation sources; however, they have failed to predict impeller forcing amplitudes accurately. The simulation framework should be able to resolve vane and blade wakes adequately for prediction of rotor-stator interaction noise as its shape governs the tone amplitudes at blade passing frequency (BPF) and harmonics [62]. The broadband component of interaction is governed by the turbulent content in rotor wake and therefore, is stochastic. Besides, acoustic damping must be adequately quantified, which can be very difficult. The system should also be able to provide postprocessing routines for characterising acoustic modes and computing sound power. This imposes challenging requirements that can only be met within three-dimensional (3-D), unsteady numerical strategies capable of resolving turbulent scales ranging from Reynolds-averaged Navier-Stokes (RANS) to large-eddy simulations (LES) with a hybrid approach like RANS-LES as an intermediate [62].

For the current investigation, the ability to directly measure rotor-stator aeroacoustic interaction will be investigated using Lattice Boltzmann Method (LBM), an inherently compressible scheme which recovers acoustics as well as fluid dynamics [66]. It implements kinetic equations for calculating particle distribution dynamics. LBM method determines

macroscopic fluid dynamics using mesoscopic kinetic equations, i.e. the Boltzmann Equation [66]. The commercial LBM package PowerFLOW will be used.

Unlike traditional CFD methods, which solve conservation equations of mass, momentum and energy on a macroscopic scale, LBM models the fluid as microscopic particles. It solves kinetic equations on a cartesian mesh (termed as the lattice) by an explicit time-stepping scheme and collision modelling. Following equation represents the form of lattice Boltzmann equation [66]:

$$f_i\,(x + c_i\Delta t, t + \Delta t) - f_i\,(x,t) = C_i(x,t), \tag{3.1}$$

where f_i denotes particle distribution function in the *i*th direction governed by a number of discrete velocity vectors $\{c_i : i = 0, \dots, N\}$. Space and time vectors are denoted by $c_i\Delta t$ and Δt respectively. The right-hand side of Equation 3.1 denotes collision term which adopts the most common Bhatnagar-Cross-Krook (BGK) form [67]:

$$C_i(x,t) = -\frac{\Delta t}{\tau}[f_i(x,t) - f_i^{eq}(x,t)] \tag{3.2}$$

Where τ denotes the relaxation time, and f_i^{eq}represents local particle distribution function, which is dependent on local fluid dynamic properties. Fluid dynamic properties like fluid velocity *u* and density ρ, are computed by moment summations over the velocity vectors [66]:

$$\rho(x,t) = \sum_i f_i(x,t), \quad \rho u(x,t) = \sum_i c_i f_i.(x,t) \tag{3.3}$$

Chapman-Enskog expansion can be used to recover the compressible Navier-Stokes equation for a carefully chosen set of discrete velocity vectors [68]. The kinematic viscosity of the fluid is related to the relaxation time parameter τ by [69]:

$$\tau = \frac{v}{RT} + \frac{\Delta t}{2} \tag{3.4}$$

Equations 3.1 to 3.4 form the basis of the LBM scheme.

LBM can recover flow acoustics by recovering ideas gas equation as well as the compressible Navier-Stokes equation. Fundamental aeroacoustic capabilities of LBM like wave propagation and compressible behaviour have been studied by [70-75]. In these studies, the scheme has been shown to capture acoustic related problems well. Other cases where LBM has proved its acoustic capabilities include the simulation of radiation from waveguides [76], aeroacoustic phenomena in ducts [77], landing gear noise [78], automotive underbody acoustics and wind noise [79], and [80], HVAC noise [81], and sunroof buffeting [82].

The Lattice Boltzmann equation is solved spatially on a grid constituting of cubic volumetric cells called voxels. It is possible to have a variable spatial resolution; however, grid size can only change by a factor of two for adjacent domains. As LBM is based on explicit time-stepping scheme, time step changes by a factor of two as well. Therefore, larger cells will not be evaluated every time step of the smallest time. Therefore, the time-step equivalent number of voxels can be defined as the total number of voxels scaled to the smallest time-step [66]. This makes the time-step equivalent number of voxels are a better indicator of the required amount of CPU hours rather than the total number of voxels.

In the LBM scheme, the viscosity model has been implemented by tweaking relaxation time τ to change the numerical viscosity of the scheme locally. An implicit large eddy simulation (ILES) scheme will be used in the current investigation where subgrid-scale viscosity is modeled through the numerical dissipation [66]. This enables direct numerical simulation of smaller scale turbulent structures as compared to the turbulence model incorporated into the

PowerFLOW LBM scheme. This will significantly improve the modelling accuracy of turbulent structures in the impeller wake, which are crucial for accurate prediction of impeller forcing amplitudes.

Recently, LBM has also proven itself as an effective tool for tackling complex engineering aeroacoustic problems. One such application is the work of Casalino et al. [83], where a Lattice-Boltzmann Very-Large-Eddy Simulations (LB/VLES) scheme was used to predict fan-stage aerodynamic performance, transonic flow features and tonal/broadband noise levels for a set of realistic fan/Outlet Guide Vane (OGV) configurations and operating conditions. Tonal levels were predicted with an error in the order of 3 dB. In another work, Casalino et al. [84] investigated noise generated by impingement of turbulent wake on a propeller using lattice-Boltzmann solver PowerFLOW. Results were compared with Large Eddy Simulation and experimental measurements showing that LB simulations performed better than LES in tonal noise prediction whereas LES results compared better in the high-frequency domain. Another advantage of using an LBM based technique for the given application is significantly lower computational costs as compared to LES. This makes PowerFlow highly feasible for studying centrifugal compressor aeroacoustics. The turbulence model in PowerFLOW package is a modified version of the two-equation K - ϵ Renormalization Group (RNG) model. It incorporates a swirl based correction that reduces the amount of generated turbulence due to large vortical structures. Owing to the low numerical dissipation of ILES scheme, a lower spatial resolution is required for adequate simulation of fine vortex scales resulting in accurate fluid dynamic predictions. The computational costs of direct simulation up to the near wall region are too high; therefore, wall functions will be used to approximate wall boundary conditions. For the present study, following wall-shear stress model will be used [69], [71]:

$$u^+ = f\left(\frac{y^+}{A}\right) = \frac{1}{k}\ln\left(\frac{y^+}{A}\right) + B, \tag{3.5}$$

where,

$$A = 1 + f\left(\frac{dp}{dx}\right). \tag{3.6}$$

Equation 3.5 is solved iteratively to estimate the wall-shear stress for wall boundary conditions in the LBM calculation [66]. The, a slip algorithm is used for the boundary process.

This study will be the first of its kind where impeller forcing is quantified with direct measurements from LBM and compared to existing literature. It will add to the existing body of literature on centrifugal compressor aeroacoustics and would lead to a simulation framework capable of providing the ground amplitude and the amplification factor of aeroacoustic excitation acting on the impeller.

2.8.4 Summary and conclusions

The review of the literature on excitation sources in centrifugal compressors has been presented. Numerical analysis can enable a better understanding of flow physics governing the root cause and amplitude of the unsteady pressure loading amplitudes on blade and vanes, which can aid in identifying possible aeromechanical coincidences.

Tyler-Sofrin modes emanating from rotor-stator interaction is one of the most common sources of impeller excitation. Adequate resolution of vane and blade wakes is critical for quantifying rotor-stator interaction noise as their shapes govern the amplitudes at blade passing frequency (BPF) and harmonics [62]. Resolving the broadband component of wakes is of secondary importance due to its low energy content. Furthermore, broadband sources are less likely to be amplified by acoustic resonance. Another critical factor governing tone amplitudes is the accurate prediction of aeroacoustic damping, which can be very difficult for complicated internal flows which are characteristic to centrifugal compressors.

Multiple gaps are identified in the published literature on forced vibratory response analysis in centrifugal compressors. Design simplification, e.g. neglecting cavity and leakage flows, using a modified blade count, and modelling only a sector the compressor wheel pose severe limitations on the prediction of impeller forcing amplitudes. Accurate prediction of side-cavity fluid dynamics is important to resolve resonant excitation of the source. Conflicting arguments have been found about the effects of acoustic modal coupling between side-cavity modes. The relationship between impeller forcing amplitudes and acoustic side-cavity modal coupling is not known yet.

The current state-of-the-art numerical techniques are based on conventional Navier-Stokes (N-S) solvers, which resolve turbulent structures on RANS scale. This approach might be sufficient in adequately resolving low-order acoustic modes from potential interaction between blade rows but fails to resolve higher order modes resulting from an aeroacoustic interaction. This imposes challenging requirements on the conventional URANS approach. Therefore, the LB/VLES solver PowerFLOW has been chosen as an adequate tool for the proposed research.

2.9 Technical objectives

The following objectives are put forward for this research project:

- Formulation of a simulation strategy for modelling rotor-stator interaction:
  - Understanding the physics of aeroacoustic interaction in centrifugal compressors.
  - Literature study on the forced vibratory response in turbomachinery.
  - Literature study on the state-of-the-art in turbomachinery aeroacoustic simulations.
  - Comparison between conventional Navier-Stokes and state-of-the-art Lattice Boltzmann Technique based techniques in terms of accuracy and resource requirements.
- Aeroacoustic analysis of two-dimensional benchmark compressor geometry using traditional URANS based technique:
  - Modal decomposition of pressure fluctuations in temporal and spatial domain caused by rotor-stator interaction using two-dimensional DFT.
  - Comparison results with Tyler-Sofrin Theory [19].
- Comparison between a URANS and LBM based approach in simulating centrifugal compressor aeroacoustics.
- LBM based approach for modelling centrifugal compressor aeroacoustics:
  - Estimating amplitudes, frequencies and mode shapes of dominant Tyler-Sofrin modes.
  - Study of the relationship between side-cavity mode coupling and impeller forcing amplitudes.
  - Estimation of the resonance amplification factor by simulating aerodynamically similar off-resonant conditions.

2.10 Research questions

Following research questions have been formulated:

1) What are the mechanisms governing forced vibratory response in centrifugal compressors?
2) What are the limitations of the current state-of-the-art simulation strategy to quantify the aeroacoustic phenomenon in centrifugal compressors?
   a. What components must be included in the model?

    b. Can direct measurements provide a reasonable estimation of aeroacoustic forcing or implementation of an acoustic analogy is necessary?
    c. How strong are the amplitudes due to rotor/stator interactions?
    d. How strong are the amplitudes of such an acoustic resonance?
3) Is an LBM based approach feasible for simulating centrifugal compressor aeroacoustics?
    a. Is it possible to extract accurate Tyler-Sofrin modal amplitudes?
    b. Can compressor acoustic eigenmodes be visualized?

This will lead to the following contributions:

1) The first of its kind unsteady numerical simulations will be performed to quantify aeroacoustic forcing in a full centrifugal compressor stage including hub and shroud side cavities.
2) A comparison study between conventional URANS based technique and an LBM based technique, which is the current state-of-the-art in aeroacoustic simulations. This study will be the first application of LBM for studying centrifugal compressor aeroacoustics.
3) Development of a simulation framework capable of accurately predicting aeroacoustic forcing amplitudes in a centrifugal compressor operating at conditions of acoustic resonance. This would enable accurate forced response calculations on the realistic centrifugal compressor stages to assess the severity of aeromechanic coincidence.
4) Side-cavity mode coupling will be studied, and its effects on impeller forcing will be analysed.
5) Acoustic response sensitivity analysis would enable operational guidelines for centrifugal compressor operators to decrease and if possible, avoid aeromechanic coincidences. This would also lead to a better assessment of the severity of the problem.

2.11 Thesis outline

The thesis is outlined in the following manner:

Chapter 3:

Chapter 3 describes the technical approach to the numerical analysis proposed to address the research questions described in Section 2.10. The case set up for each simulation has been presented along with the model assumptions when applicable.

Chapter 4:

Results from solver assessment studies are presented in Chapter 4. Firstly, the results from a URANS based approach for modelling rotor-stator interaction in a benchmark 2D compressor are presented. Then, the results from a comparison study between URANS and LBM based approach are presented. Two-dimensional pressure spectra obtained from DFT of various CFD probes are presented. Accuracy of performance and acoustic predictions from both approaches are assessed for the same number of CPU hours. Chapter 4 provides recommendations on a suitable modelling approach.

Chapter 5:

Chapter 5 presents the results from the LBM approach applied to the research compressor. Grid convergence of key aerodynamic and aeroacoustics parameters are assessed. Results are divided into two parts: flow field and acoustics. Acoustics results are further divided into

two sub-sections. Firstly, the two-dimensional pressure spectrum are presented. This is followed by a discussion on the origin of dominant modes. Then, the dominant modes are visualised.

The implications of using a swirl mass flow inlet boundary condition are discussed. Effects of inlet swirl on compressor performance as well as acoustic amplitudes are addressed. Flow field snapshots are presented to distinguish flow features responsible for discrepancies in performance and acoustic amplitudes.

Chapter 6:

Chapter 6 describes the methodology to estimate the acoustic resonance amplification factor in the centrifugal compressor. Two technical approaches are described, and modal amplitudes are compared with the acoustic resonance operating conditions.

Chapter 7:

Chapter 7 presents the summary and conclusions of the research and ends with recommendations for future experimental and computational work.

3 Technical approach

3.1 Introduction

Three sets of numerical analysis have been designed and implemented for addressing the research questions posed in Chapter 2. This chapter describes the cases and methodologies used in conducting the numerical analysis. Section 3.2.1 presents the specific models used in modelling the 2D rotor-stator interaction using a conventional URANS based approach. Section 3.2.2 describes the 3D realistic compressor model which has been used for the comparison study between URANS and LBM based approaches. Results from both approaches are analysed, and recommendations on a suitable modelling approach are given. Section 3.3 provides a detailed overview of the case setup, computational grid, and the boundary conditions for LBM simulations. Section 3.4 provides a detailed description of the computational grid, modelling assumptions and the boundary conditions used in the URANS simulations.

3.2 Numerical analysis

3.2.1 Model definition and case setup for two-dimensional Rotor-Stator interaction

Two-dimensional rotor-stator interaction is simulated to assess the feasibility of CFD in capturing the relative Tyler-Sofrin mode amplitudes. A two-dimensional (2D) URANS based CFD model is used to calculate the flow field. A case with realistic compressor geometry has been simulated. The geometry for this case is shown in Figure 13. The impeller rotates clockwise, and the flow direction is radially outwards. There are 15 impeller blades and 8 diffuser vanes. The impeller outlet diameter is 0.440m. The model operating conditions are chosen from the actual design operating conditions. The case setup is given in Table 1.

Property	**Value**	**Unit**
Number of cells	672000	-
Turbulence model	$k-\omega$ SST	-
Rotation speed	13050	*RPM*
Density	Ideal gas	kg/m^3
Inlet mass flow	2134.0	kg/s
Relative Outlet pressure	7205000	*Pa*
Time-step	450	*x/rev*

Table 1 Case setup for the 2-D rotor-interaction simulation.

A 2D structured grid with hexahedral cells is used in the Finite-Volume CFD solver ANSYS Fluent. Flow is resolved up to the wall using boundary layer refinement with $y^+ < 1$. A mass flow inlet has been specified with constant static pressure at the outlet. A time-step corresponding to 0.8 degrees of impeller revolution has been chosen. This ensures sufficient temporal resolution to capture the unsteady rotor-stator interaction [85].

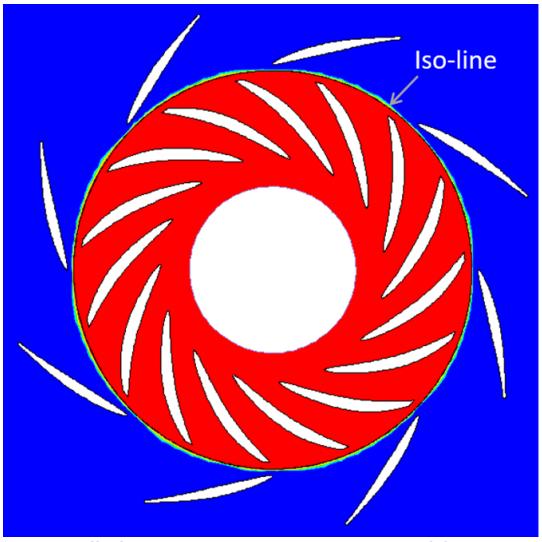

Figure 13 Realistic compressor geometry used for 2D analysis.

The sliding mesh technique has been used to account for impeller rotation. This option allows translation or rotation of a domain with respect to another part of the domain. The impeller part of the domain, indicated in red (refer Figure 13) rotates at the specified RPM while the diffuser, indicated in blue (refer Figure 13) is stationary. Pressure data is monitored over a circumferential line between the rotor and the stator, as indicated in Figure 13. This data is used to extract relative amplitudes of Tyler-Sofrin modes.

The conservation equations for mass, momentum and energy are solved in the absolute frame of reference. Turbulence is modelled using SST $k-\omega$ (2 equation) model. Therefore, flow is resolved up to the wall.

3.2.2 Three-dimensional realistic compressor case

Aeroacoustics of a realistic three-dimensional research compressor is simulated. Two different approaches are tested: a conventional URANS based approach as found in the literature, and a novel LBM based approach. Both approaches are compared in their ability to predict the performance and aeroacoustics of the research compressor. A suitable technique is then chosen for a comprehensive aeroacoustic analysis.

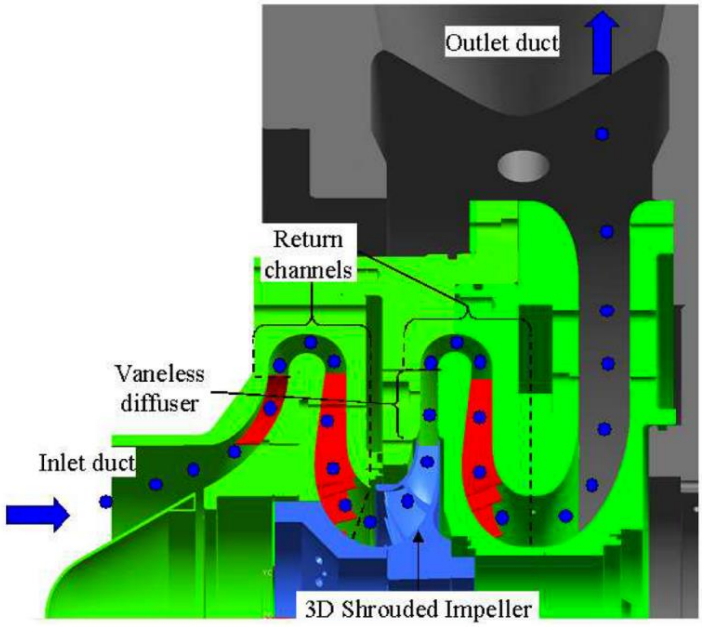

Figure 14 Cut-section of the experimental rig. The gas path is indicated in blue [4].

The cut-section view of the test rig depicted in Figure 14 is taken from [4]. The presented components are a part of a closed-loop system with a pressurised gas supply, a throttleable nozzle, a discharge volume and a cooler. A nozzle is used to control the volumetric flow injected into the loop, which also controls the stage inlet pressure. A variable speed hydraulic torque converter allows a wide range of shaft speeds.

The stage is equipped with tandem rows of pre-swirl and de-swirl vanes in the channel upstream of the impeller. The first blade row (pre-swirl vanes) (shown in Figure 14) replicates the presence of an upstream rotating impeller. In order to reduce the required computational effort, the first set of blade rows have not been explicitly included in the unsteady CFD model; instead, their effect is modelled using a swirl boundary condition at the inlet of the flow domain (i.e. upstream of the inlet de-swirl vanes). The second blade row represents the standard return channel de-swirl vanes which remove the incoming swirl from pre-swirl exit flow.

The instrumentation schematic is presented in Figure 15 with the position of unsteady pressure sensors, CFD probes and strain gauges. The hardware configuration analysed in the current CFD analysis consists of 17 pre-swirl vanes and 14 de-swirl vanes and 16 de-swirl vanes downstream of the impeller. There are 21 blades in the impeller.

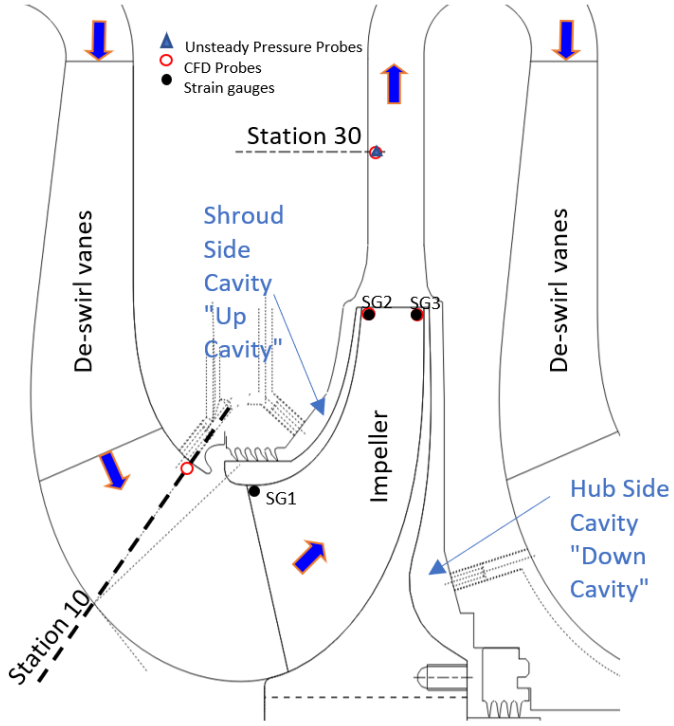

Figure 15 Schematic of the research compressor indicating unsteady pressure sensors, CFD probes, and strain gauges. Flow direction has been indicated by blue arrows [4].

The Campbell diagram during a ramp-up cycle from 10,000 to 16,000 RPM obtained from experimental data for SG2 response is shown in Figure 16. High vibratory response was measured when nitrogen (N_2) was used as the working fluid and not with carbon dioxide (CO_2). Therefore, N_2 is the working fluid of interest for this research. The design point for the compressor is reached at 14646 RPM at a peripheral Mach number of 0.73 [65]. Three points for a strong vibratory response can be seen across the 30/rev excitation line. Only the results from the 30/rev excitation line are relevant for the current investigation as it corresponds to the impeller and adjacent blade row counts. The maximum vibratory response was measured at 6700 Hz (hereafter referred to as OP – 30/rev operating condition). Maximum unsteady pressure amplitudes were recorded at 7323 Hz (hereafter referred to as Nominal – 30/rev operating condition).

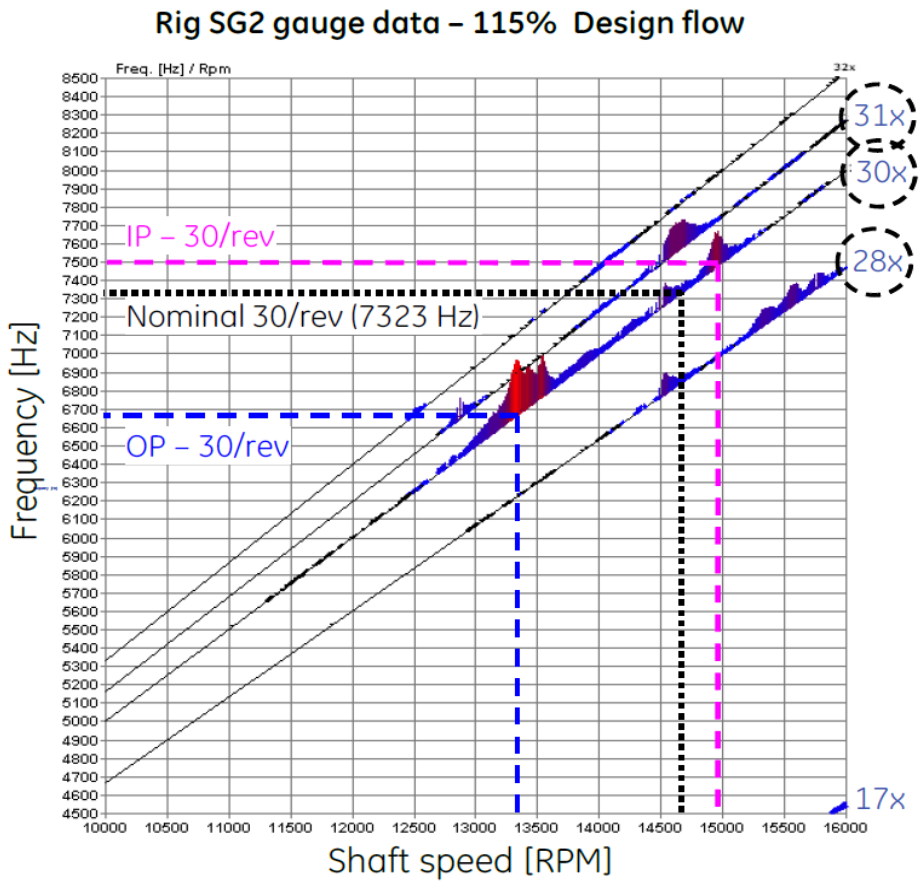

Figure 16 Campbell diagram for SG2 obtained from experimental data taken from [9].

OP 30/rev operating point is chosen for CFD analysis as it caused the highest impeller trailing edge vibratory response. Critical performance as well as acoustic parameters are quantified and compared with experimental measurements.

3.3 Model definition and case setup in PowerFLOW[1]

The CFD analysis was performed using the commercial code Dassault Systems PowerFLOW version 6-2019. Figure 17 shows the computational setup. The region encapsulated by the black square corresponds to the experimental flow domain. The impeller region is depicted in red, indicating the faces used in the generation of a so-called Local Reference Frame (LRF). This enables implementation of a sliding-mesh, where the LRF rotates relative to other portions of the domain. The de-swirl vanes upstream of the impeller are depicted in blue, and

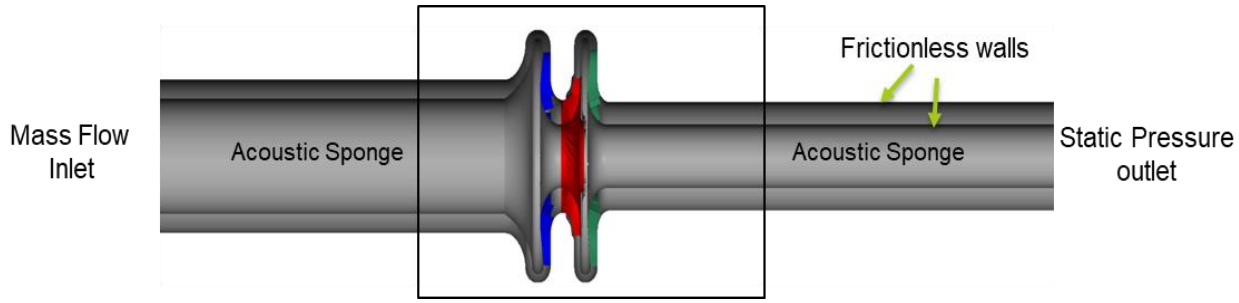

Figure 17 Computational setup.

[1] PowerFLOW is a registered trademark of Dassault Systèmes

the return channel de-swirl vanes are depicted in green. The inlet and outlet sections of the flow domain have been extended to facilitate acoustic sponge zones. The sponge zones are characterised by high viscosity and a large voxel size to dampen the acoustic waves. The large length of the extended ducts ensures that their acoustic eigenfrequencies are low compared to compressor cascade acoustic eigenfrequencies. The impeller consists of 21 blades, and the cavity-blade tip gap is approximately 3 mm.

As discussed above, the OP 30/rev is used for the detailed aeroacoustic analysis and model validation with test rig data. The impeller Ω = 1415 rad/s (13516 rpm). This corresponds to a blade-passing frequency (BPF) of 4730 Hz and a blade tip Mach number of 0.67. The average Reynolds number at the impeller blade midspan chord is 2.58×10^6. The inlet temperature is set to 291.1 K, which corresponds to the experimental conditions. Inlet turbulence is set to 5% with a turbulent length scale corresponding to 10% of the inlet annular diameter. These values have been selected based on previous experience with similar simulations; however, they do not seem to have a significant impact on flow development in the compressor stage. Mass flow inlet and static pressure outlet have been used as boundary conditions. As discussed in Section 3.2.2, the effect of pre-swirl inlet vanes has been modelled using a swirl inlet boundary condition. As pre-swirl vanes are used to replicate flow field from an upstream rotating impeller, the swirl angle has been carefully estimated from the flow exiting the impeller in a non-inlet swirl case. The setup of a swirl inlet boundary condition is described in Appendix C.

Resolution	**VRs**	**Resolution [Voxels/ wavelength]**	**Impeller y^+**	**Voxels (10^6)**	**FEV (10^6)**	**FES (10^6)**	**CPU TIME (Hours)**
Extra Coarse	3	*34*	*150-700*	*1.84*	*1.84*	*6.2*	*489*
Coarse	3	*48*	*96-521*	*6.54*	*5.37*	*18*	*949*
Medium	3	*68*	*60-348*	*16*	*13.3*	*29.2*	*2956*
Fine	3	*97*	*25-220*	*129*	*105.9*	*59.7*	*5421*
Extra Fine	3	*138*	*12-138*	*239*	*217*	*76.2*	*13000*
Ultra Fine	4	*222*	*1-80*	*608*	*324*	*107.4*	*38419*

Table 2 Grid resolution, number of grid elements and CPU time.

The six grid resolutions used in the present investigation are reported in Table 2. Three Variable Resolution (VR) regions have been chosen with the finest VR region encompassing impeller, return channel and cavity region. The resulting number of Voxels, Fine Equivalent Voxels (FEV), and Fine Equivalent Surfels (FES) have been reported as well. The CPU time has also been reported, which is the computational time required to simulate 14 impeller revolutions.

The extra coarse and coarse cases were simulated to perform the case sanity check. The extra coarse simulations ran for a total of 30 impeller revolutions to check the periodic unsteady state which was achieved after 10 impeller revolutions. This was followed by data acquisition, which was performed for 4 impeller revolutions. The current best practice for these types of simulations reported by Casalino et al. [83] has been used in this analysis. The medium resolution was run for over 10 revolutions and the last frame was used to seed fine runs. This resulted in faster convergence.

The computational grid for ultra-fine resolution is divided into VR regions as shown in Figure 18. The finest region (VR3) is defined as a boundary layer refinement in the impeller and side cavity region. VR2 resolution region is defined around the impeller, cavities, and return channel region. The ultra-fine resolution has 4 voxels/mm length in the VR2 region. This corresponds to 200 voxels/ wavelength of the 30/rev excitation (highest frequency of interest). VR1 is the coarser region defined in rest of the computational domain except the extended

inlet and outlet ducts. The acoustic sponge region defined at the extended inlet and outlet regions is the coarsest region (VR0) with a resolution of 1 voxel/mm. The VR2 region is extended beyond the return channel to reduce erroneous non-physical noise sources occurring from passing of unsteady flow features across resolution regions [72].

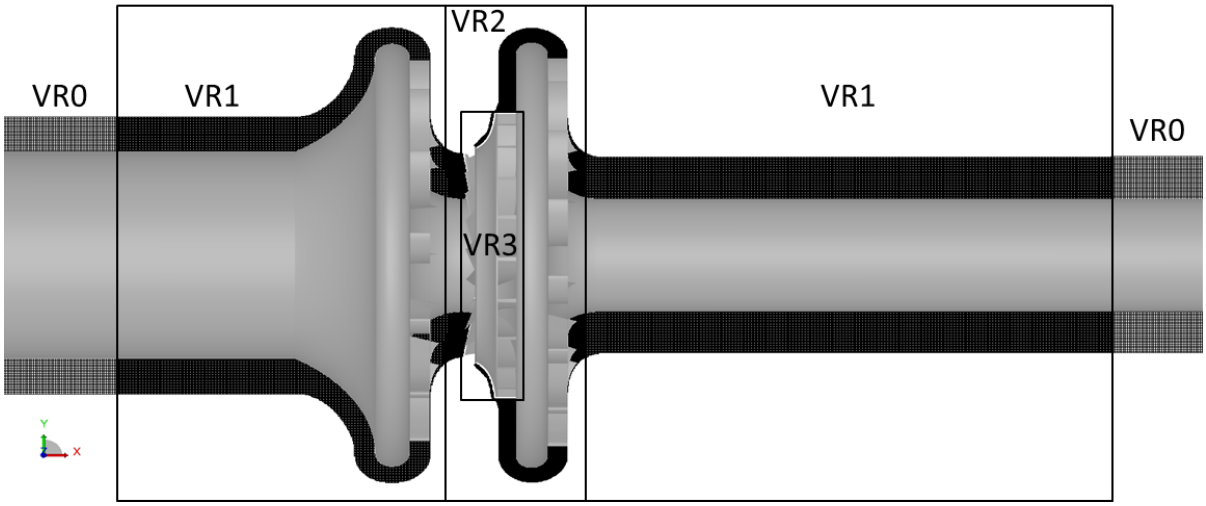

Figure 18 Resolution regions for the centrifugal compressor case. VR0 indicates coarsest, and VR3 indicates the finest grid resolution.

Several CFD probes were set up at various locations in the flow domain. Every probe stores the flow solution at a single voxel for each time-step during the calculation. The number and location of these probes are outlined as follows:

1. 63 equally spaced circumferential probes at Station 10.
2. 63 equally spaced circumferential probes towards the shroud cavity side of impeller blades (SG2).
3. 63 equally spaced circumferential probes towards the hub cavity side of impeller blades (SG3).
4. 63 equally spaced circumferential probes at Station 30.

The location of these probes corresponds to the experimental position of strain gauges and unsteady pressure sensors. The motivation behind this was to perform acoustic analysis and to compare with experimental rig unsteady pressure measurements. A large number of circumferential probes has been chosen to ensure that enough spatial resolution is available to detect ±30 lobes. Station 10 and 30 probes are in a stationary frame of reference while the probes inside the impeller are rotating with the impeller. All the probes are located in the finest (VR2) resolution region with a cell size of 0.36mm. The measurement frequency of all the probes is 1.59e+06 Hz.

3.4 Model definition and case setup in Fluent[2]

The CFD analysis was performed using the commercial code ANSYS Fluent. For this analysis, the *k-ω* turbulence model has been used. A standard limitation of the two-equation turbulence models is the excessive generation of turbulence kinetic energy in the vicinity of stagnation regions [86]. A modified version of the turbulence production term has been implemented as per the work of Launder and Kato to overcome this limitation [87]. The density-based explicit solver has been used due to its stability in high-speed compressible flow regime [88].

[2] Fluent is a registered trademark of ANSYS, Inc.

A steady full-annulus calculation was performed before the unsteady case. The converged flow solution was used to initialise the unsteady case. This resulted in a faster and stable convergence. A temporal resolution of 740 time steps per impeller wheel revolution was chosen for the unsteady CFD calculation. This corresponds to 35 time steps per blade passing period. This is sufficient to resolve the unsteady flow features at the frequencies of interest [15]. The calculation ran for 14 impeller revolutions before reaching a periodic unsteady state. The sampled flow solution from the last 4 revolutions was used to store the data from which the source and amplitude of 30/rev impeller forcing could be determined.

Property	**Value**	**Unit**
Number of cells	46	*million*
Turbulence model	*k-ω*	-
Operating pressure	0	*Pa*
Rotation speed	13516	*RPM*
Inlet mass flow	10.73	*kg/s*
Static Outlet pressure	429095	*Pa*
Time-step	740	*x/rev*

Table 3 Overview of 3D research compressor case setup in Fluent.

The number and location of probes are the same as LBM case setup (refer Section 3.3.2). This has been done to allow a direct comparison between both the solvers and the test rig data. The measurement frequency of all the probes is 1.6e+5 Hz, which is governed by the time step chosen for this simulation. An overview of the case setup is given in Table 3.

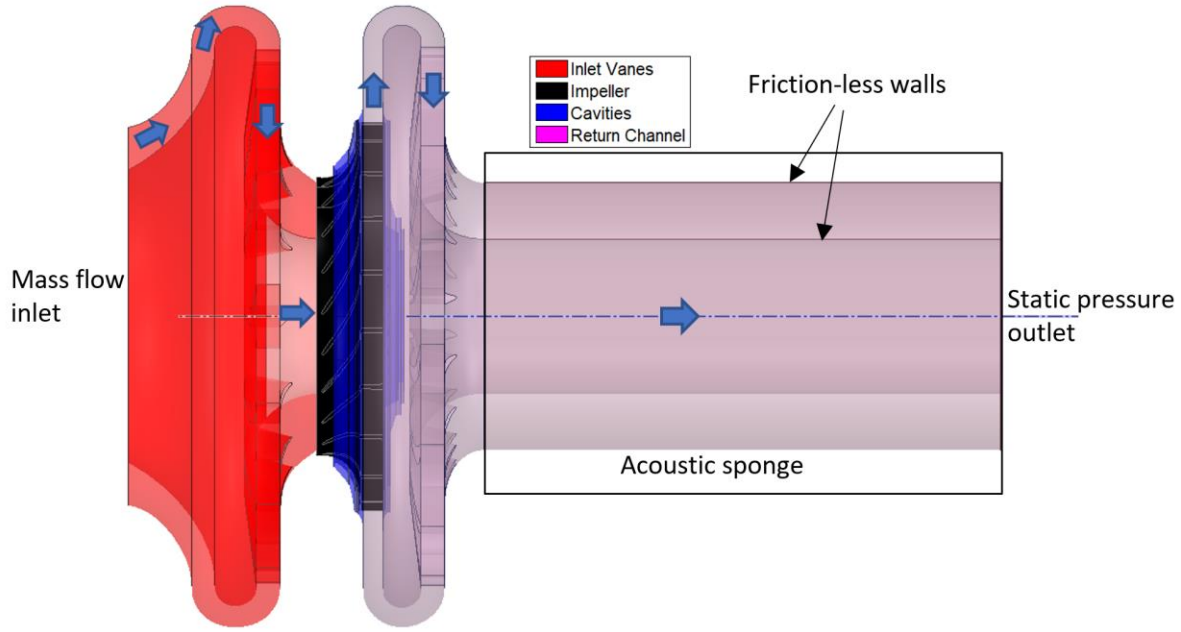

Figure 19 Computational setup in Fluent. Cell zones are color coded.

The flow domain has been divided into three cell zones to facilitate the sliding mesh technique. This allows for the rotation of the impeller cell zone with respect to inlet, cavities and the return channel. For the present investigation, the impeller part of the domain, indicated in black (refer Figure 19) rotates at the specified RPM while the other two cell zones are stationary. It must be noted that both the hub and shroud side cavities are a part of the return channel cell zone. They are indicated separately for illustration purposes only.

Mass flow inlet and static pressure outlet boundary condition are implemented. Acoustic sponge zone has been defined at the extended outlet channel as shown in Figure 19. This is

done to ensure there are no acoustic wave reflections from outlet domain boundary. Acoustic sponge region comprises of large cells and friction-less walls to ensure no artificial pressure losses are added to the system.

The grid was generated using Pointwise[3] software. Triangular prism elements have been used to refine wall boundary in the impeller region while the rest of the flow volume is discretised using a combination of pyramid and hexahedron elements. Grid resolution must be chosen with great care for resolving turbomachinery blade row interactions. As a rule of thumb, ten cells must be present per minimum propagated wavelength to accurately capture acoustic wave propagation [89]. Grid resolution corresponding to 41 cells per 30/rev excitation wavelength was ensured in every direction to capture acoustic wave generation and propagation. This resulted in approximately 3 million cells per blade passage in the impeller. For the complete CFD domain, including 14 de-swirl vanes, 21 impeller blades and 16 return channel de-swirl vanes, the total grid size amounts to 46 million. An example of the grid is shown in Figure 20 [90]. A detailed representation of the grid near impeller blade trailing edges and hub side disk is shown in Figure 21.

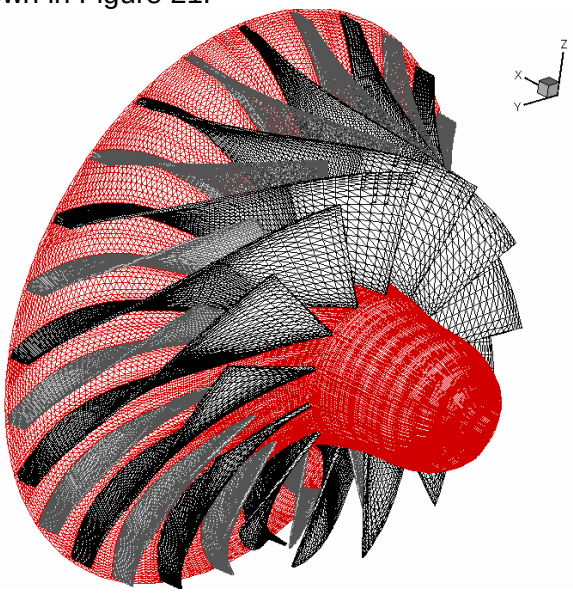

Figure 20 An example of the grid showing impeller blades and hub side disk [90].

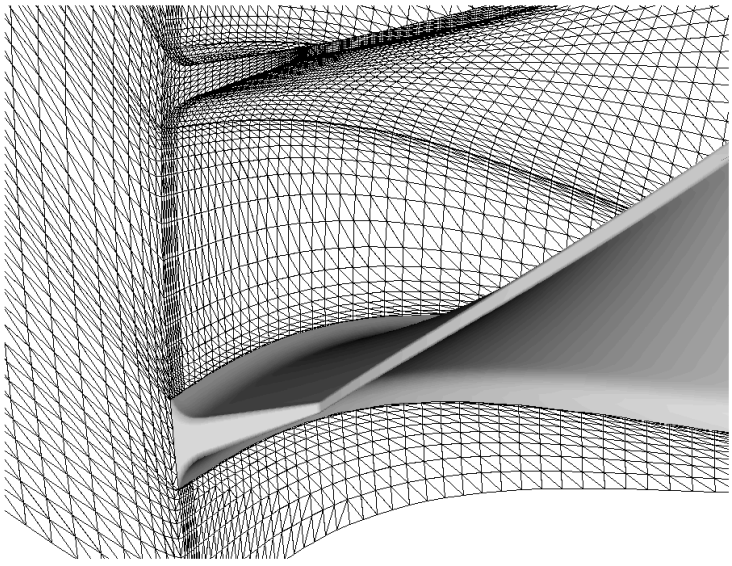

Figure 21 Detailed grid representation: hub near the blade trailing edges [90].

[3] Pointwise is a registered trademark of Pointwise, Inc. in Fort Worth, Texas, USA.

4 Results of code assessment studies

4.1 Introduction

The results from numerical analysis are presented and assessed in a way to address the research questions posed in Chapter 2. The compressor aeroacoustics and performance predictions from CFD are compared with test rig data. Results from the benchmark 2D rotor-stator interaction simulation are presented in Section 4.2. This is followed by the results of a comparison study between the LBM and URANS based approach, which is presented in Section 4.3. Results from a comprehensive LBM based approach are presented in Section 4.4. Effects of grid refinement on the prediction of stage performance and acoustics are also assessed.

4.2 Two-dimensional Rotor-Stator Interaction

In the following section, the results of the two-dimensional rotor-stator interaction calculation are presented and assessed. The impeller has 15 blades, and there are 8 diffuser vanes.

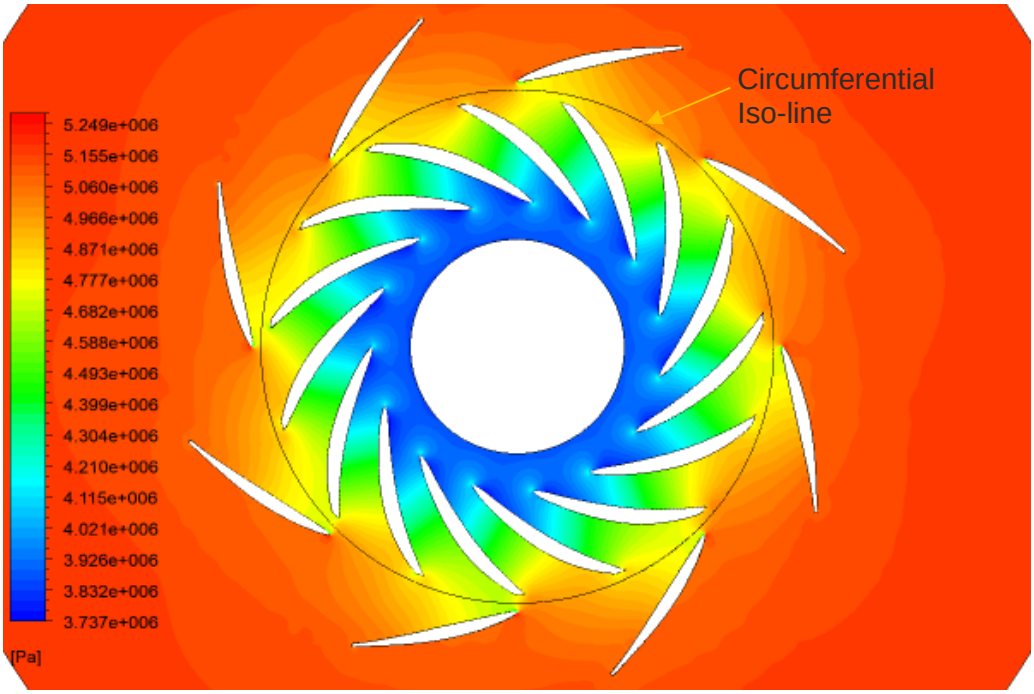

Figure 22 Instantaneous pressure field in the flow domain.

The snapshot of flow-field coloured by pressure magnitude is shown in Figure 22. The Tyler-Sofrin theory states that the pressure field from a rotor-stator interaction can be decomposed into an infinite number of spinning modes [19]. In order to compare results from CFD with Tyler-Sofrin theory, the pressure was monitored along a circumferential iso-line in-between the impeller blade trailing edge and the diffuser vane leading edge as indicated in Figure 22.

Figure 23 depicts the plot of static pressure as a function of circumferential location along the iso-line and time for one impeller rotation. The circumferential location is the length along the iso-line indicated in Figure 22. The data shows 8 spatial repetitions due to the number of diffuser vanes, and 15 repetitions in time due to the number of rotor blades. A 2D DFT was performed on this data to evaluate the relative magnitude of the Tyler-Sofrin modes. This would determine the number of lobes *m* at a specific harmonic *n* of BPF.

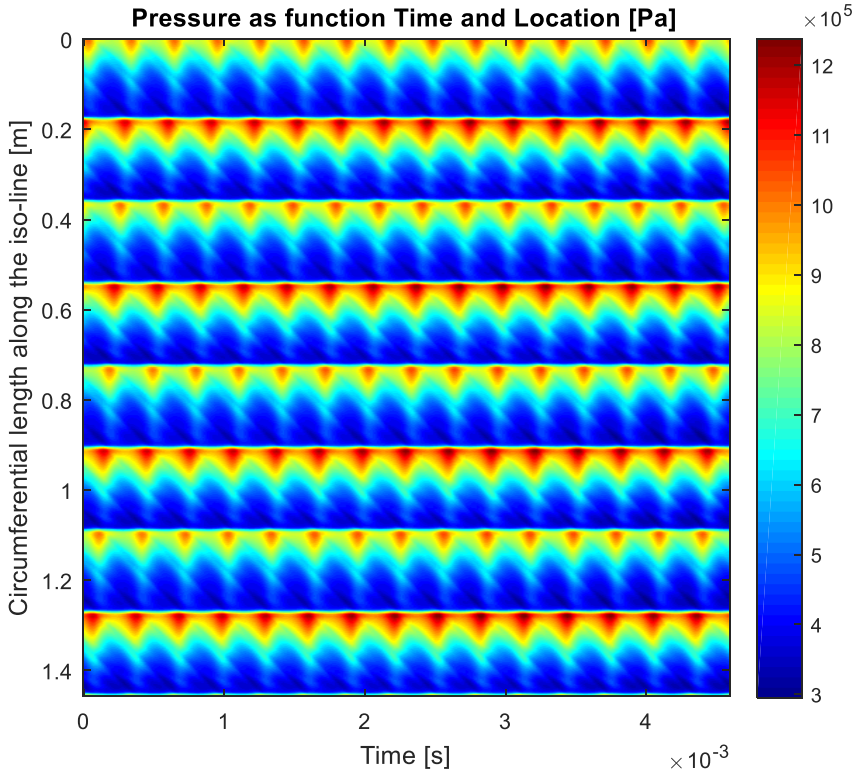

Figure 23 Pressure as a function of time and location along the circumferential iso-line for one rotation of the impeller.

The modes from Tyler-Sofrin theory are presented in Table 4. The two BPF harmonics, n = 1 (1*BPF) and n = 2 (2*BPF) are indicated in the rows. The VPF harmonic, k is varied between -7 and 1 column-wise from left to the right. For instance, 1*BPF excites a spinning pressure pattern with 7 lobes. This conforms to the Tyler-Sofrin relation given in Equation 2.4 using the values B = 15 (number of impeller blades), n = 1 (first harmonic of BPF), V = 8 (number of diffuser vanes) and k = -1 (first harmonic of VPF). The rotational speed of this mode is $n*B/m$ = 2.14 times the impeller rotational speed. The spinning direction of a mode is determined by the sign of m. A mode spins in the same direction as the impeller if m is positive otherwise, it spins in the opposite direction. Similarly, m = +14 is the dominant acoustic mode observed at n = 2 (2*BPF). The relative amplitude of the modes are obtained from the 2D pressure spectra as shown in Figure 24. Dominant modes are indicated in bold-red in Table 4.

K*VPF / n*BPF	-7	-6	-5	-4	-3	-2	-1	0	1
1	-41	-33	-25	**-17**	**-9**	**-1**	**7**	**15**	23
2	-26	-18	-10	**-2**	**6**	**14**	22	30	38

Table 4 Number of lobes (m) for Tyler-Sofrin modes. Negative values indicate counter-rotating lobes.

The result from the 2D DFT is given in Figure 24. The vertical axis denotes the frequency of rotation of lobes in multiples of BPF, and the number of lobes is given on the horizontal axis. The pressure magnitude is normalised by dividing it to the mean pressure on the iso-line over a time period of one impeller rotation. The chosen range for the number of plotted lobes is ±15. The peaks can be observed at the first and second harmonic of BPF with red colour

indicating modes with peak amplitudes. For example, 1*BPF generates dominant peaks at -9, -1, and 7 lobes, which can be found in Table 4 as well. Similarly, 2*BPF generates dominant peaks at -2, 6, and 14 lobes. These are Tyler-Sofrin modes as clear from Table 4.

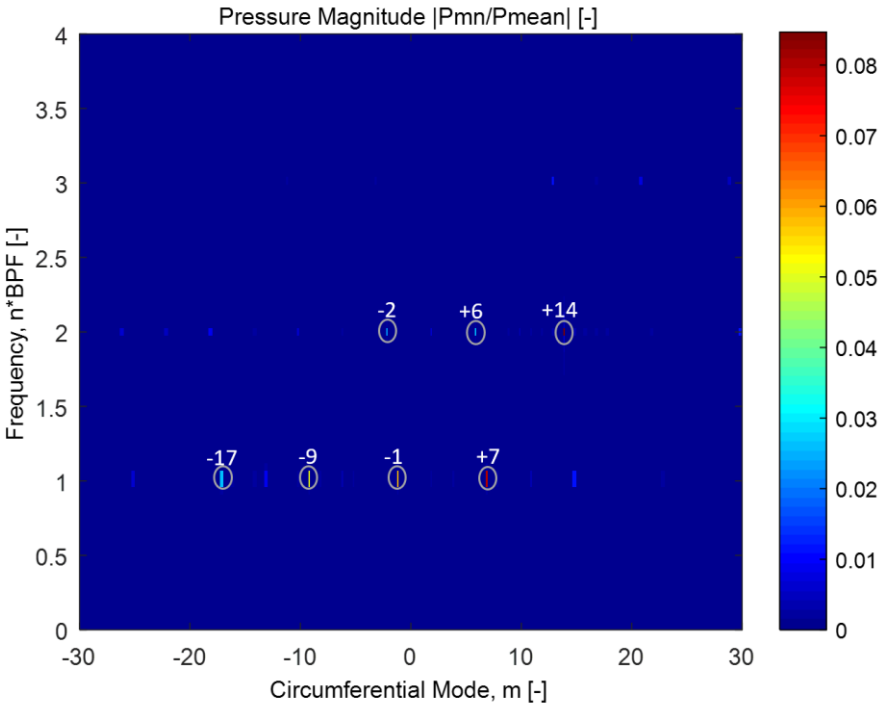

Figure 24 2D-DFT of the pressure signal as a function of time and location.

Based on the above analysis, it can be concluded that a CFD analysis can capture the fluctuating pressure field from rotor-stator interaction. Hence, a direct CFD/CAA analysis would enable estimates on relative Tyler-Sofrin modal amplitudes by resolving pulsation sources and the resulting acoustic wave generation and propagation.

4.3 URANS vs LBM based approach: 3D Compressor results

Results from the comparison study between URANS and LBM based approach are presented and discussed in this section. The setup and modelling approach for both cases have been previously described in Chapter 3. The choice of grid size for URANS simulations was constrained due to the limited availability of computational resources. For a fair comparison, the grid size for LBM simulation was chosen such that both approaches consume a similar number of CPU hours. A periodic unsteady state was reached in case of URANS simulation after 14 impeller revolutions. This was followed by a data acquisition run, which continued for 4 impeller revolutions. LBM case at the chosen grid resolution converged after 10 impeller revolutions. The data acquisition in LBM was also carried out for 4 impeller revolutions. The accuracy of the performance and acoustic predictions from both approaches are assessed. This section concludes with recommendations for a suitable modelling approach for the detailed aeroacoustic analysis of the research compressor.

PowerFLOW is chosen as the computational tool for LBM simulation. It is based on an Implicit Large Eddy Simulation (ILES) scheme, which enables direct simulation of smaller scale turbulence structures as compared to the turbulence model implemented in the URANS based approach using Fluent. This should improve the modelling accuracy of turbulent content in the impeller wake. Therefore, the impeller forcing amplitudes should be better predicted with the LBM based approach.

4.3.1 Comparison with experiments

Table 5 presents the comparison of URANS performance and acoustics predictions with experimental data.

Number of Cells (Millions)	Impeller y^+	Error in T_{tot} at stage exit [%]	Error in Polytropic Efficiency [%]	Error in stage Compression Ratio [%]	Error in SPL [dBs]	CPU Hours
35.2	10-295	0.4	64	23	-0.8	5852

Table 5 Fluent results.

The comparison of performance and acoustic predictions from LBM simulation with test rig data is presented in Table 6.

FEV (Millions)	Impeller y^+	Error in T_{tot} at stage exit [%]	Error in Polytropic Efficiency [%]	Error in stage Compression Ratio [%]	Error in SPL [dBs]	CPU Hours
129	25-220	-1.03	40	9.3	+5.2	5421

Table 6 PowerFLOW results.

Stage pressure ratio has been computed as the ratio of stage outlet total pressure to total pressure at Station 10 (locations given in Figure 15). Polytropic efficiency of a centrifugal compressor stage is defined as the ratio of ideal work to actual work of compressor for a differential pressure change [91]. It is calculated as follows:

$$\eta_{polytropic} = \frac{\gamma - 1}{\gamma} \frac{\ln(\frac{P_{02}}{P_{01}})}{\ln(\frac{T_{02}}{T_{01}})} \tag{4.1}$$

where γ denotes the heat capacity ratio for the working medium. P_{02} and T_{02} denote the stage exit total pressure and total temperature respectively. P_{01} and T_{01} denote the total pressure and temperature at Station 10. By considering temperature rise for a given pressure rise across the stage, polytropic efficiency is a better indication of solution convergence than temperature or pressure rise alone. Polytropic efficiency is found to be significantly overpredicted with both the techniques. As it is directly proportional to the natural log of stage pressure ratio, this discrepancy can be attributed to the overprediction in stage pressure ratio.

As mentioned in Chapter 3, the absence of upstream pre-swirl blade row is one of the most important differences between the current CFD and experimental setup. The purpose of these vanes is to replicate the flow-field from the outlet of an upstream rotating impeller. Without them, the flow incidence angle at the leading edge of de-swirl vanes is very high. This caused the leading-edge flow separation at the de-swirl vanes (indicated in Figure 39) resulting in a significant underprediction of pressure at Station 10. This is the reason for a large discrepancy in stage polytropic efficiency prediction for both the techniques.

LBM based technique was found to be significantly more computationally efficient as compared to URANS. This resulted in the choice of a finer mesh for LBM technique. The discretisation approaches are different for both the techniques. LBM technique is based on a cartesian grid with uniform cell (voxel) size around the impeller. In the case of URANS, finer cell size is used to capture the high curvature gradient towards the leading and trailing edge of the blades and vanes. The range of y^+ at the impeller is specified to compare the grids.

4.3.2 Acoustics results for OP 30/rev operating condition

Acoustic predictions from both solvers are assessed by comparing the two-dimensional unsteady pressure spectra obtained from the stationary CFD probes at Station 10 and 30 (locations given in Figure 16). Figure 25 presents the results of a 2-D pressure spectra of Station 10 probes in the LBM simulation. Circumferential mode number is plotted on the X-axis, and the frequency is plotted on the Y-axis. The frequency has been non-dimensionalised by dividing it to the impeller rotational speed in Rotations Per Second (RPS). Pressure amplitude has been normalised by dividing it to the mean pressure on a point probe at Station 10.

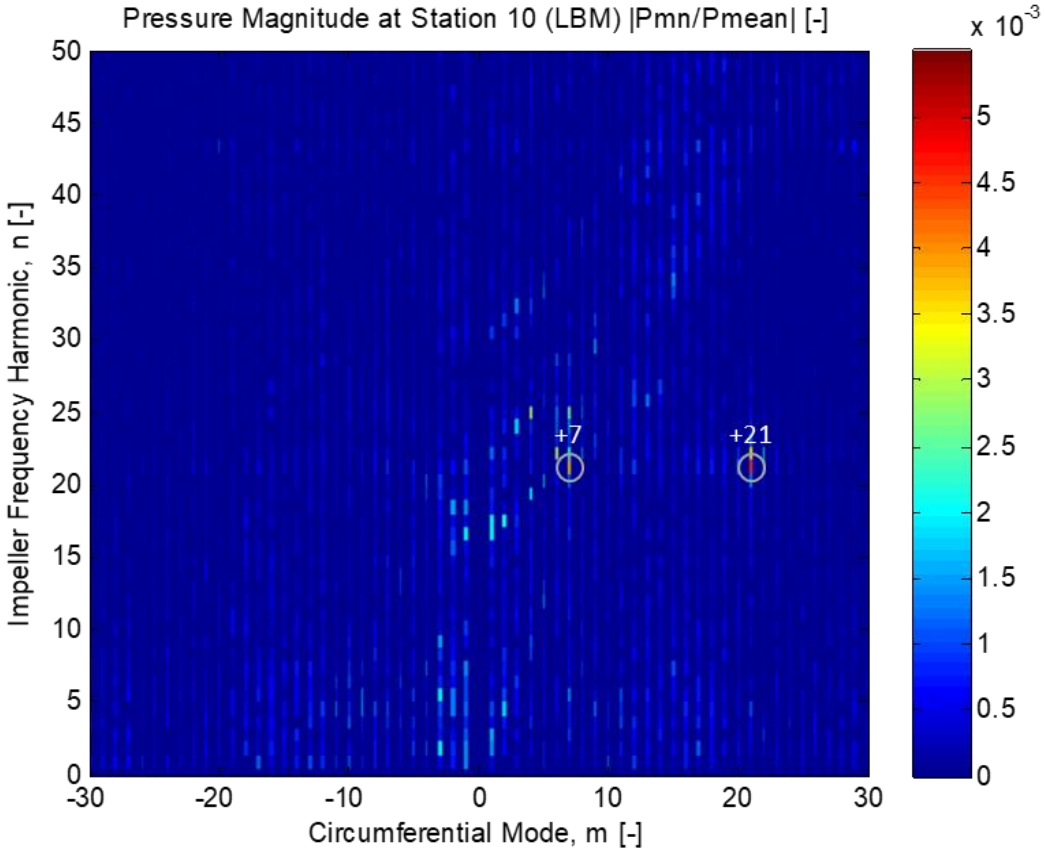

Figure 25 2D Pressure Spectra at Station 10 (LBM).

Single frequency harmonic can be seen with significant amplitude – 21/rev, which corresponds to 1*BPF. The circumferential modes corresponding to these frequencies are acoustic waves. The temporal and spatial variation of pressure caused due to these waves is governed by Equation 2.6. The dominant m = +7 and +21 observed in Figure 25 are spinning acoustic modes generated due to the interaction between wakes from inlet de-swirl vanes and the impeller blades. It conforms to the relationship given by Tyler-Sofrin in Equation 2.4 by substituting B = 21 (number of impeller blades), n' = 1 (1*BPF) and V = 14 (number of upstream vanes). The value of k' is -1 for m = +7 and 0 for m = +21 (rotor only mode).

Pressure spectrum of Station 10 probes from URANS simulation is presented in Figure 26. Comparison between 21/rev (1*BPF) mode amplitudes are presented in Figure 27. The impeller only circumferential mode (m = +21) is slightly stronger for the URANS based approach as compared to LBM. The +7 mode amplitude is comparable for both techniques. Another difference is the absence of lower frequency modes for URANS based approach. Overall, mode amplitudes are comparable for both the techniques.

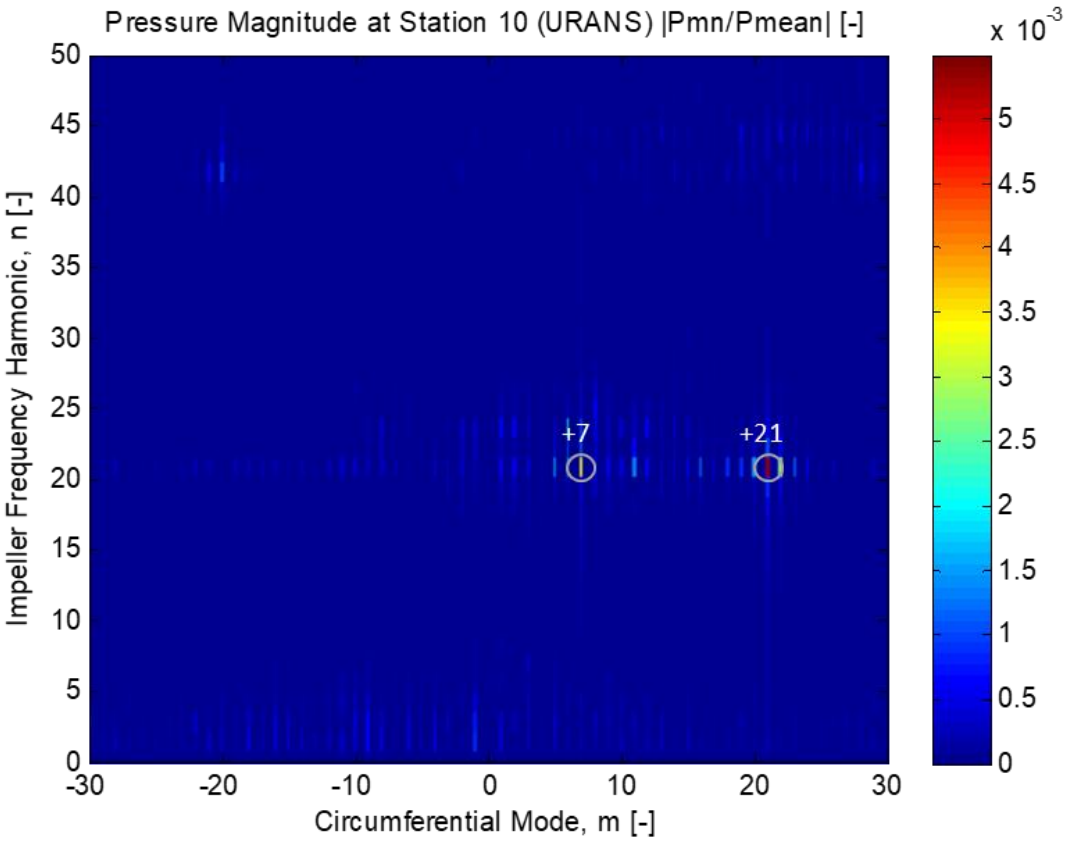

Figure 26 2D Pressure Spectra at Station 10 (URANS).

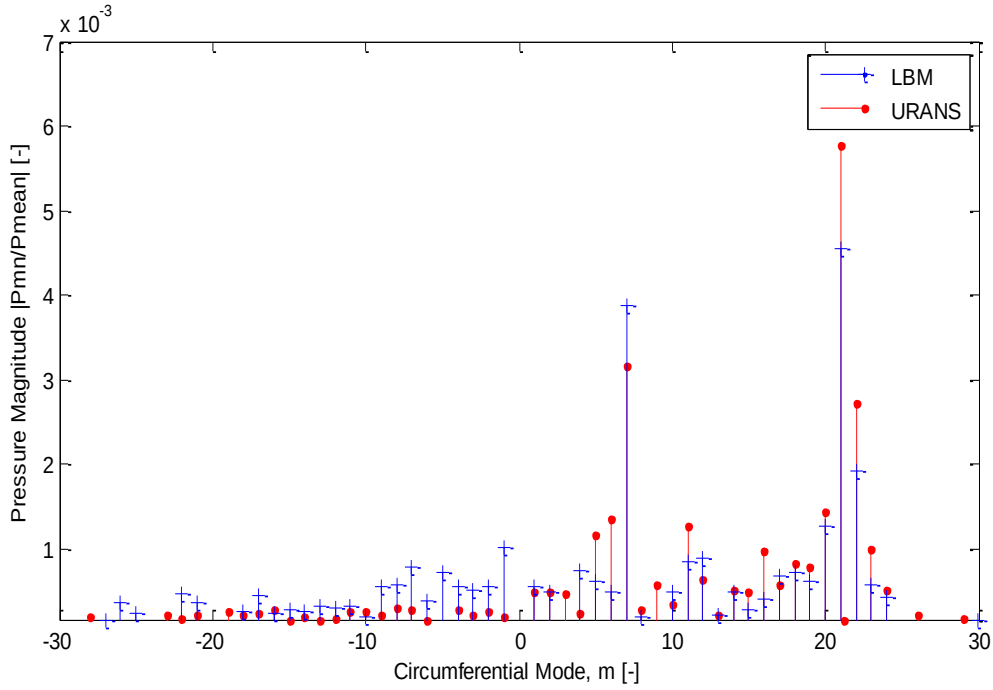

Figure 27 URANS vs LBM circumferential Fourier mode decomposition – 21/rev (1*BPF) at Station 10.

Figure 28 presents results from a similar analysis performed for Station 30 probes in case of LBM simulation. Station 30 probes are located in the return channel downstream of the impeller. Dominant Tyler-Sofrin modes are highlighted.

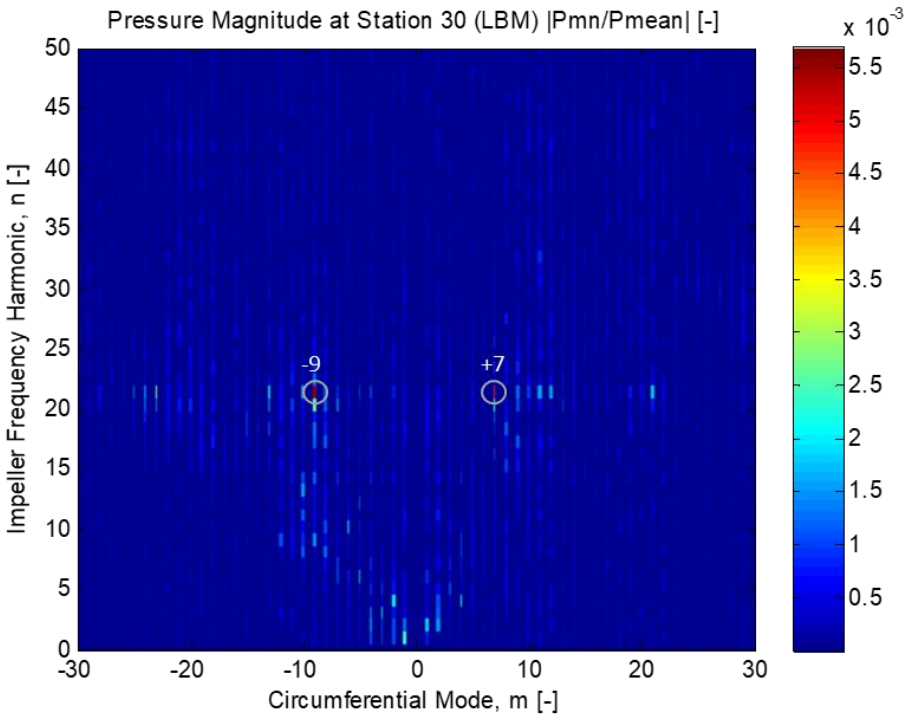

Figure 28 2D Pressure spectra at Station 30 (LBM).

The relative amplitudes of +7 and -9 modes are comparable. The presence of +7 mode at Station 30 suggests that this mode is cut-on and therefore, can propagate in the return channel. -9 mode is generated due to the reflection of the +7 mode from the downstream de-swirl vanes. This conforms to the Tyler-Sofrin in relation given in Equation 2.5 using the values: m = +7 (incident acoustic mode), V = 16 (downstream de-swirl vane-blade count) and the integer value k' = -1 (de-swirl vane frequency harmonic). The resulting -9 mode is reflected upstream causing the 30/rev excitation at the impeller trailing edge.

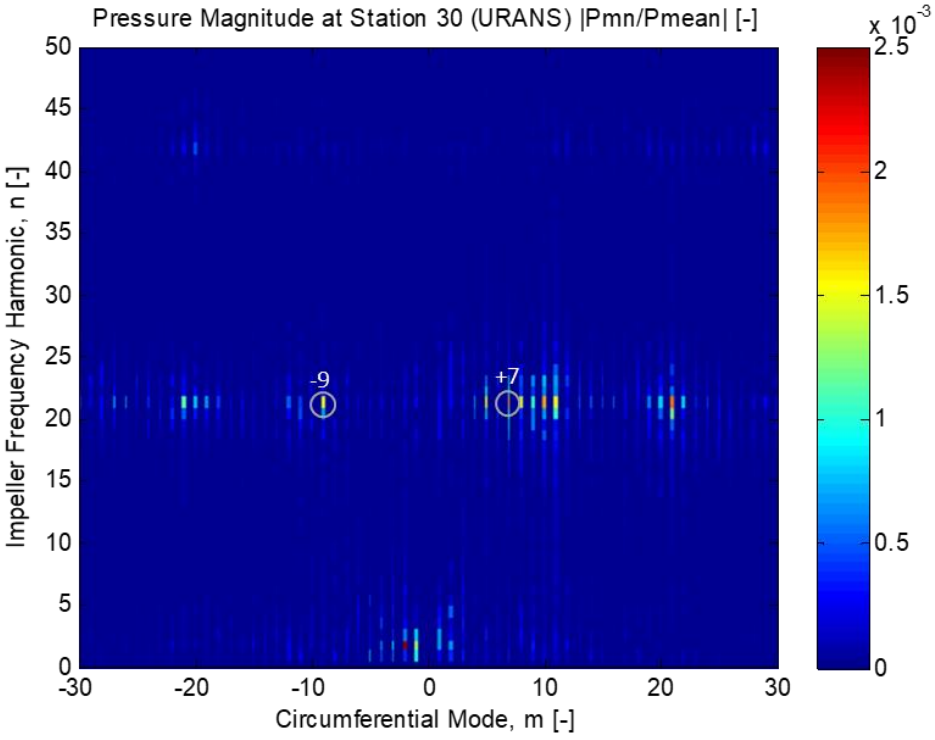

Figure 29 2D Pressure spectra at Station 30 (URANS).

Figure 29 presents the pressure spectra for Station 30 probes obtained from URANS simulation. Qualitatively, 21/rev (BPF) modes agree with the LBM simulation. The dominant +7 and -9 modes are visible, but with significantly lower amplitude. Furthermore, a relatively broad peak is visible close to the +7 mode, with significant acoustic energy in +5, +8, and +9 modes. This is different from LBM results, as seen in Figure 30. This can be attributed to the higher spatial resolution of the LBM technique.

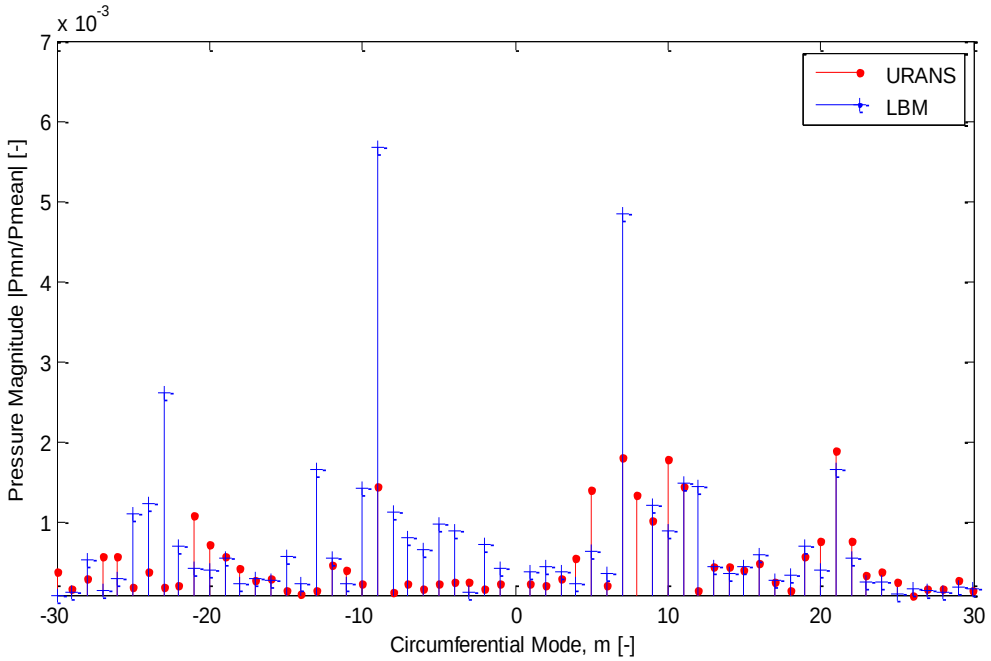

Figure 30 URANS vs LBM circumferential Fourier mode decomposition – 21/rev (1*BPF) at Station 30.

4.3.4 Summary and conclusions

A comparison study was conducted between a URANS based approach and an LBM approach to assess their ability to predict centrifugal compressor performance and aeroacoustics. Mode amplitudes at Station 30 from URANS based approach are significantly lower as compared to LBM. Furthermore, a broadband peak is observed in the vicinity of +7 mode with significant energy in +5, +8, and +9 modes in case of URANS. SPL at Station 30 is lower in case of URANS based approach as compared to the LBM. However, the comparison of SPL at Station 30 from both techniques with experiments is not fair since the increased hydrodynamic interaction between the impeller and upstream de-swirl vanes amplifies the noise sources. This will be further elaborated in Section 5.4.

The URANS based approach at current grid resolution fails to predict turbulent fluctuations in impeller wake; therefore, cut-off tone amplitudes are severely underpredicted as well. URANS method is unable to capture small eddies, which are usually responsible for producing broadband noise. Furthermore, as -9 mode is generated by the acoustic wave propagation and reflection from downstream de-swirl vanes (due to the significant distance between the blade rows), the dissipative nature of the URANS technique affects the mode amplitude. On the other hand, the LBM technique captures a broader spectrum of turbulent scales. Therefore, broadband content is better captured as well.

It can be concluded that a URANS based technique at current grid resolution can capture the acoustic wave generation and propagation due to the hydrodynamic interaction between the upstream de-swirl blade row and the impeller. Due to a relatively small distance between the blade rows, the dissipative effects due to spatial discretisation are less pronounced. However, it fails to capture the dominant Tyler-Sofrin mode amplitudes at Station 30. At this point, it is

hard to distinguish the case setup related effects (e.g. spatial and temporal discretisation, numerical schemes and turbulence model) from the solver physics.

In summary, it is observed that the LBM technique is computationally more efficient and is more accurate than the URANS (for a similar number of CPU hours) in predicting both the performance as well as the aeroacoustics of the research compressor. Therefore, LBM is chosen for a comprehensive aeroacoustic analysis of the compressor stage. The discrepancy in stage pressure ratio will be improved by imposing a co-rotating swirl boundary condition at the domain inlet. This will replicate the effects of an upstream rotating impeller. Furthermore, inlet and outlet ducts will be extended to facilitate acoustic sponge zones. This will dampen acoustic wave reflections from domain boundaries.

5 Detailed aeroacoustic analysis (LBM based approach)

LBM based solver PowerFLOW is chosen as a suitable tool to study the aeroacoustics of the research compressor. In this section, the results from a grid refinement study are presented where grid dependency of stage performance and acoustic parameters are assessed. The modelling approach is validated by comparing the results with test rig data. The results are split into two parts: flow field and acoustics. The implications of imposing a co-rotating swirl on the domain inlet boundary are also discussed.

5.1 Grid refinement study

The main objective of this study is a qualitative assessment of solution convergence without being tied to the experimental data. Grid resolution was successively refined globally with a factor of 1.4 until no significant variation was observed between two consecutive resolutions. An addition VR region was added to the ultra-fine case for boundary layer refinement in the impeller and side cavity region. The six grid resolutions used in the present investigation have been reported in Table 2. Results from grid convergence of stage total pressure ratio, total temperature ratio and polytropic efficiency plotted in Figure 31.

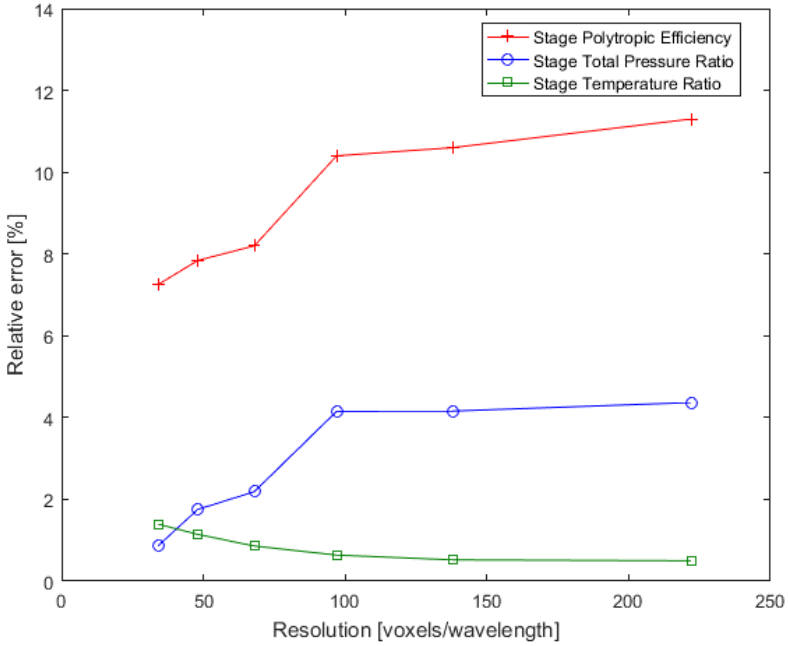

Figure 31 Stage pressure ratio, outlet total temperature and polytropic efficiency dependency on grid resolution.

The relative error in stage temperature, as well as pressure ratio is less than 1% for the two finest grid resolutions i.e. extra fine and ultra fine (refer Table 2 for resolution). The relative error in stage polytropic efficiency is less than 2%.

Acoustics convergence is verified by comparing modal amplitudes at Station 30 for the two finest grids. The results are plotted in Figure 32. The resolution is defined in voxels/wavelength

of 30/rev excitation. With a variation of less than 1% between both resolutions, acoustic convergence has been achieved.

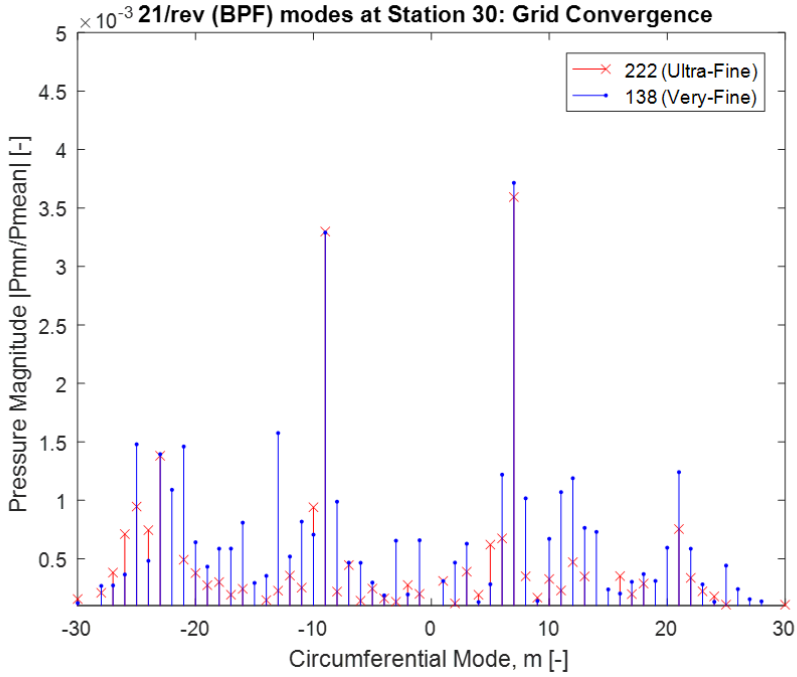

Figure 32 Grid convergence of acoustics: pressure spectra at Station 30 (fine vs coarse grid). Resolution is defined in voxels/wavelength of 30/rev excitation.

The convergence of SPL at Station 30 is presented in Figure 33. With a variation of less than 0.1 dB between the two finest grid resolutions, acoustics is converged as well. On overall, it can be concluded that the grid resolution effects on acoustics as well as performance are limited in the investigated range.

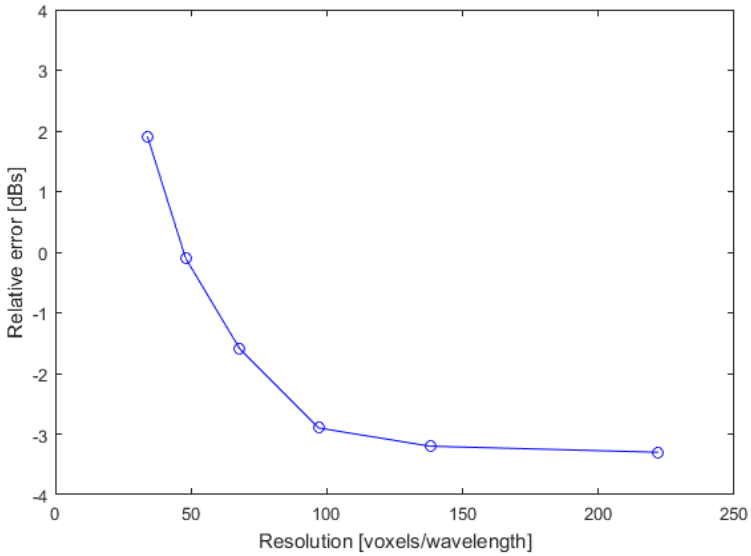

Figure 33 Grid convergence of acoustics: SPL at Station 30.

5.2 Experimental validation

The performance predictions have been significantly improved by imposing a co-rotating swirl at the compressor inlet. It reduced the flow incidence angle at the de-swirl vanes upstream of the impeller, thus, reducing the flow separation and the associated pressure losses. The

comparison of key acoustic and performance prediction from CFD with test rig data is given in Table 7.

Resolution [voxels/ wavelength]	Impeller y^+	Error in stage Temperature Ratio [%]	Error in stage Polytropic Efficiency [%]	Error in stage Pressure Ratio [%]	Error in SPL [dBs]
222	1-80	0.3	11.5	4.2	-3.2

Table 7 Experimental validation (Ultra-Fine resolution).

Stage pressure ratio is overpredicted by 4.2% in comparison to experimental data. As stage outlet pressure is fixed (as a boundary condition), this discrepancy is attributed to an underprediction in total pressure at Station 10. As discussed previously in the report, the upstream set of pre-swirl vanes are not explicitly modelled. Their effect has been simulated by using a swirl inlet boundary condition. Furthermore, cavity leakage flows are not modelled. The discrepancy can be attributed to these modelling simplifications.

Stage temperature ratio is overpredicted by 0.3% in comparison with test rig data. Stage polytropic efficiency is overpredicted by 11.5% in comparison with test rig data. As predicted stage temperature rise agrees well with test rig data, the overprediction of stage polytropic efficiency can be attributed to the error in stage pressure ratio prediction. The SPL at Station 30 is underpredicted by 3.2 dBs. Addition of pre-swirl vanes resulted in considerable improvements in the stage performance and acoustics predictions. The results are presented in Appendix B.

5.3 Flow-field results for OP 30/rev operating condition

Surface contour of time-averaged dimensionless velocity magnitude is shown in Figure 34. Maximum velocity is reached at impeller trailing edge with an absolute Mach number of 0.67. Regions of flow separation are observed at the trailing edges of the upstream and downstream de-swirl vanes. These are indicated using black circles in Figure 34.

Time-averaged dimensionless total pressure (Cp) contour is shown on the symmetry plane in Figure 34. The pressure loss resulting from trailing edge flow separation at the upstream and downstream de-swirl vanes is marked with black circles. The approach for non-dimensionalisation is presented in Appendix A.

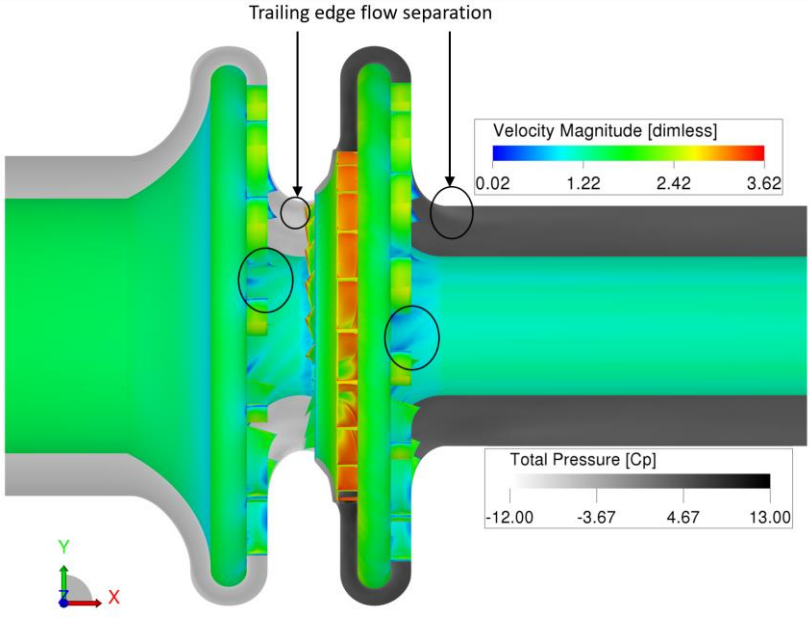

Figure 34 Total pressure and velocity magnitude contours.

Figure 35 shows the time-averaged distribution of the dimensionless total temperature on the symmetry plane. The stage inlet total temperature is fixed as a boundary condition. Significant temperature rise is observed in the compressor side cavities. The shroud side cavity exhibits the highest temperature in the flow domain. Unlike the shroud side cavity, the hub side cavity exhibits a significant total temperature gradient in the radial direction. This affects the shape of spinning Tyler-Sofrin acoustic modes resulting in a phenomenon called mode-bending [29], [42].

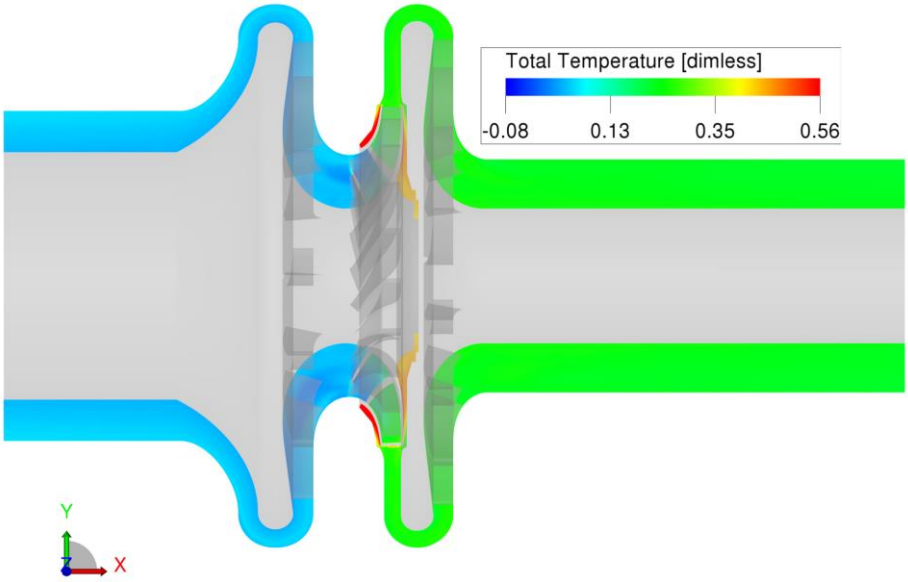

Figure 35 Time-averaged flow field on the symmetry plane. Coloured by the dimensionless total temperature.

A snapshot of the flow field is shown by the λ_2 criterion coloured by vorticity magnitude in Figure 36. Vortex shedding and flow recirculation are captured at the trailing edges of the de-swirl vanes upstream of the impeller. This is one of the key mechanisms of turbulence production upstream of the impeller. The wakes from upstream de-swirl vanes are ingested by the impeller causing the +7 mode as discussed in Section 5.4. This phenomenon also amplifies the +21 (rotor only) mode.

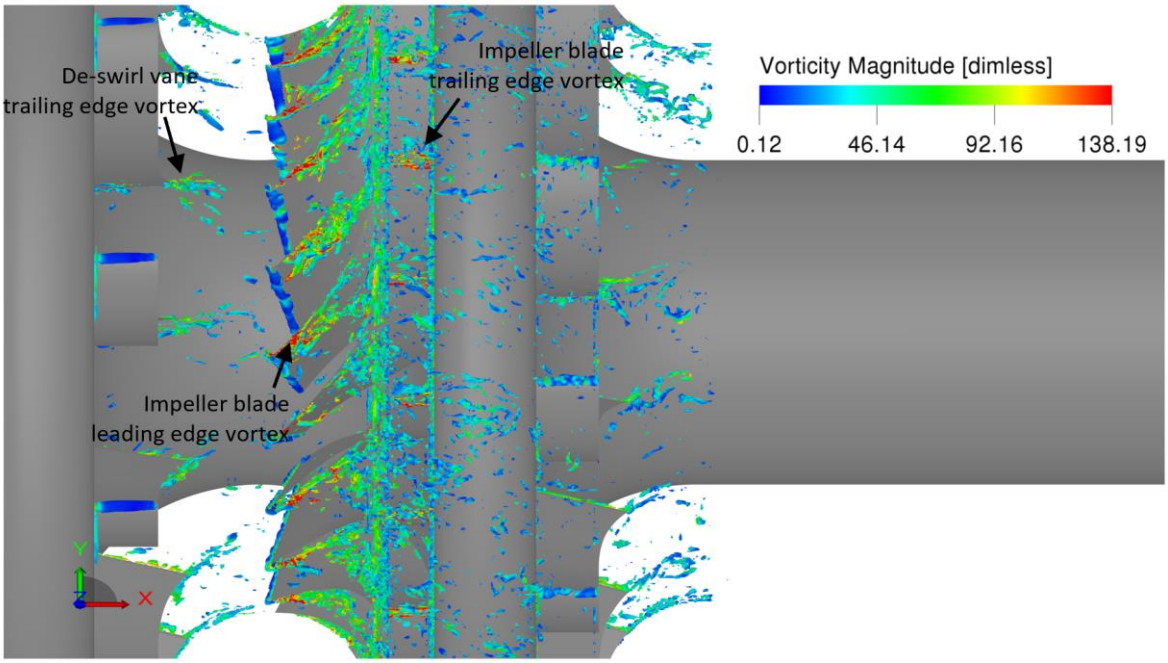

Figure 36 Iso-surface of the λ_2 criterion colored by the dimensionless vorticity modulus.

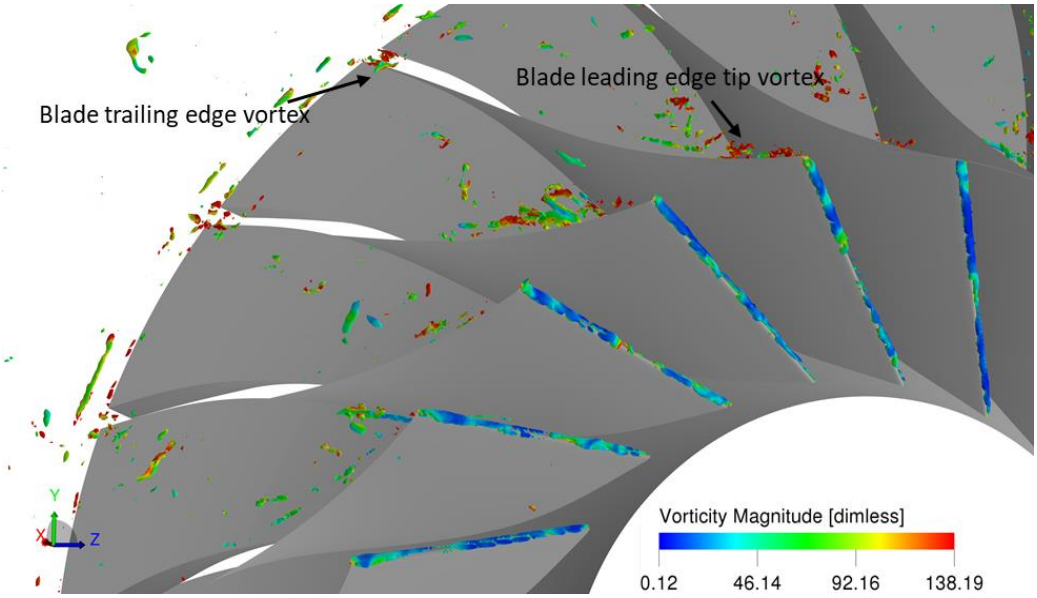

Figure 38 Instantaneous iso-surface of the λ2 criterion colored by the vorticity modulus.

Zones of high vorticity are observed near the shroud side of the impeller blade leading edges. A close-up of the impeller blade leading, and trailing edge vortices are shown in Figure 38. A significant increase in flow incidence angle from the hub to the shroud side on the impeller leading edge caused regions of high vorticity magnitude as marked in Figure 38. The thin leading edge of the impeller blades causes shedding of vortex-tube like structures. This phenomenon is highlighted in Figure 37. In the present investigation, the flow incidence angle fluctuations are linked to flow unsteadiness caused by blade passing effects therefore, the vortex core is extremely unsteady and time-periodic with the blade passing frequency. This onset of such vortices has also been studied numerically by Dufour et al. [92]. They found that the vortex moved circumferentially along the shroud increasing the flow incidence angle on the adjacent blades. However, this phenomenon was only observed close to stall operating conditions.

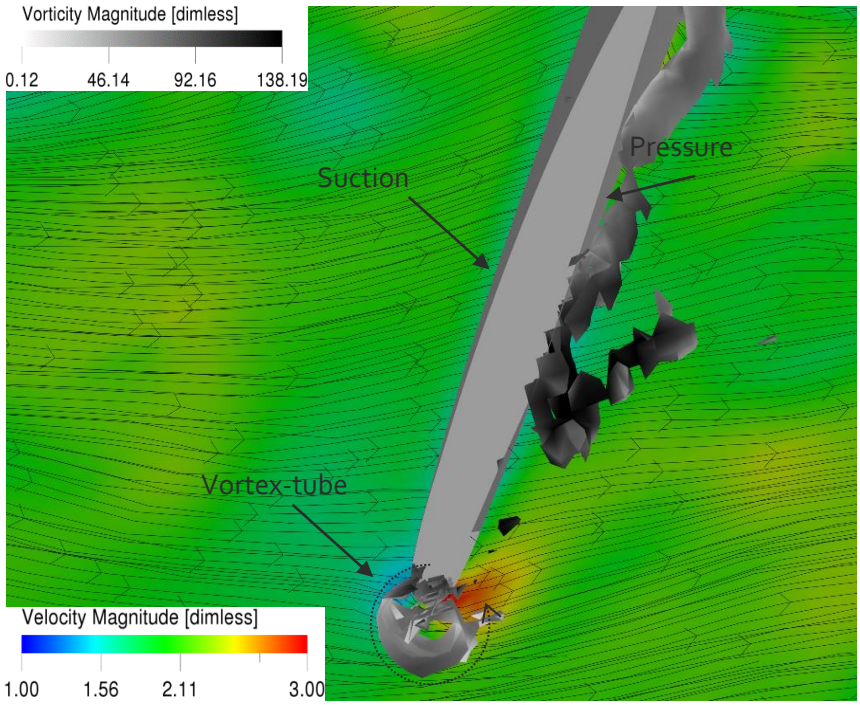

Figure 37 Instantaneous isosurface of the λ_2 criterion representing the vortex formation along with time averaged velocity magnitude contour around the impeller.

In summary, high flow incidence angle produces secondary flow effects at the impeller blade leading edge. This causes the build-up of low-momentum fluid towards the pressure side of the blade close to the shroud side. This is observed in Figure 37.

5.4 Effects of swirl-inlet boundary condition

Figure 39 shows the effects of swirl-inlet boundary condition on the compressor flow-field development. In the absence of swirl-inlet boundary condition (refer to Figure 39(a)), leading-edge flow separation is observed. This leads to the formation of vena-contracta causing relatively high flow acceleration in the vane passage. Another key difference is that the vane wakes are not attenuated and are ingested by the impeller.

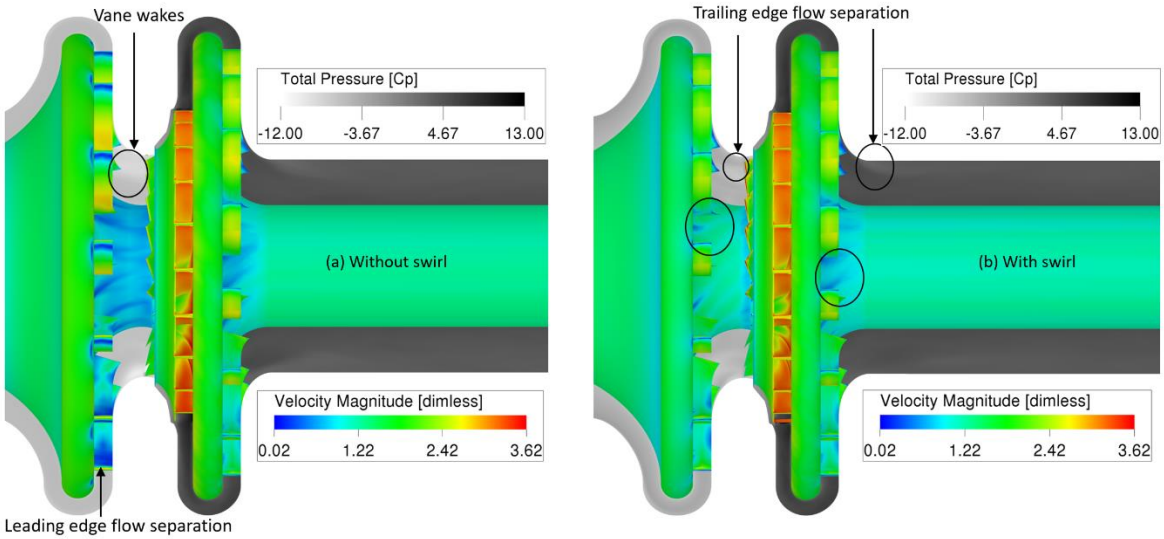

Figure 39 Effects of swirl-inlet boundary condition on compressor flow-field: dimensionless surface velocity magnitude and symmetry plane total pressure contours. (a) Without swirl, (b) With swirl.

The effects of swirl boundary condition on turbulent kinetic energy upstream of the impeller are presented in Figure 40. The flow separation and recirculation impart high turbulence to vane wakes in the absence of inlet-swirl. The resulting turbulent structures are highlighted in Figure 40(a).

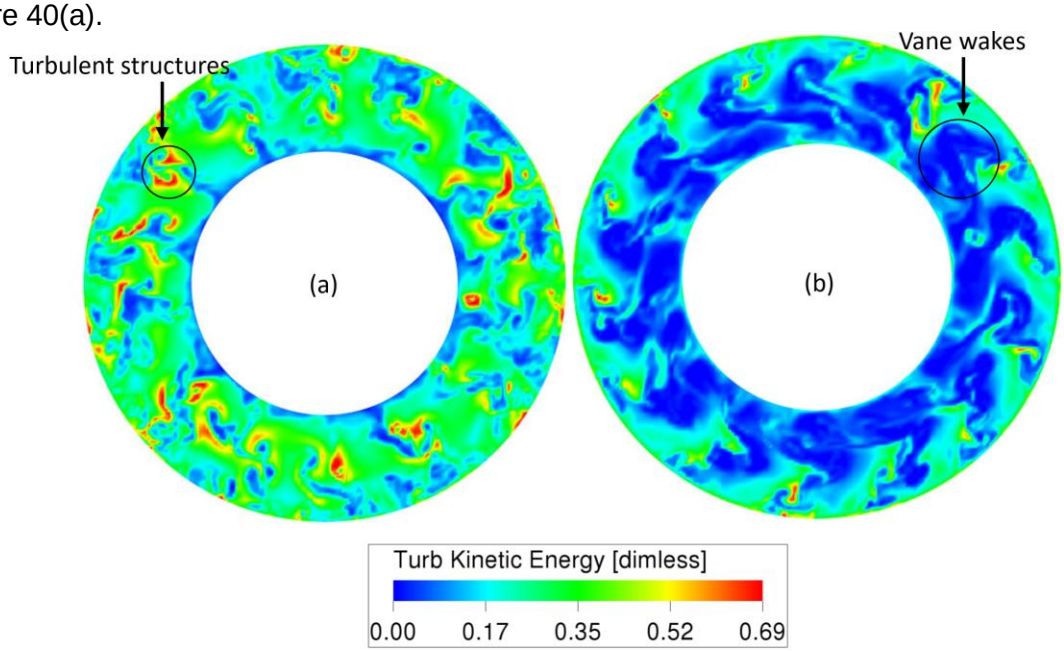

Figure 40 Turbulent kinetic energy at Station 10. (a) Without swirl, (b) With swirl.

Turbulence kinetic energy distribution is comparatively less chaotic in the case with swirl-inlet boundary condition. Vane wakes are distinctly visible and are marked by a region of low turbulent kinetic energy. This is shown in Figure 40(b). Hence, lower turbulence is ingested by the impeller in the case with swirl-inlet boundary condition. This reduces the hydrodynamic interaction between the impeller and upstream de-swirl vanes. The reduction in +7 mode amplitude at Station 30 is shown in Figure 41.

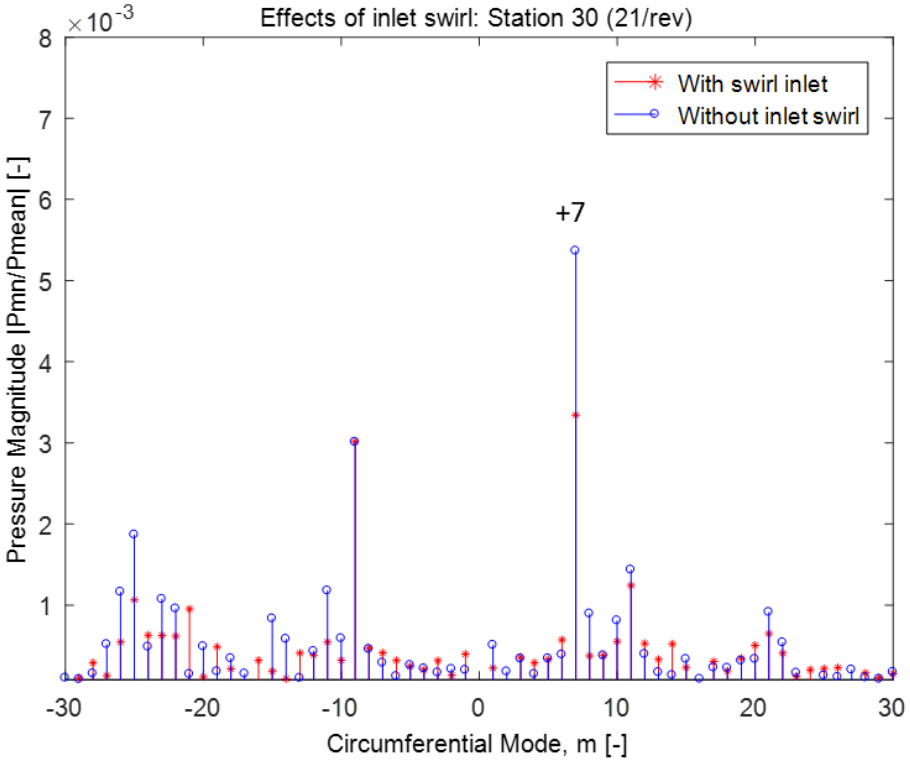

Figure 41 Effects of swirl inlet boundary condition on 21/rev – BPF mode amplitudes at Station 30.

5.4 Acoustics results for OP 30/rev

5.4.1 Two-dimensional pressure spectra

Acoustic analysis was performed in multiple steps. Firstly, a temporal and spatial Fourier transform was performed on the probes located at Station 10, Station 30 and impeller trailing edge (refer Figure 15 for locations). Each set of probes provide information on both spatial (circumferential) and temporal variation of the pressure. The two-dimensional Discrete-Fourier Transform (DFT) is performed on the data stored by each set of probes, as follows [4]:

$$\hat{P}_{mn} = \frac{1}{M}\sum_{j=0}^{M-1}\frac{1}{N}\sum_{k=0}^{N-1} p(\theta_j, t_k)e^{-i2\Pi(jm/M - kn/N)} \tag{5.1}$$

Here, the number of circumferential probes is denoted by M and the number of time steps is denoted by N. This provides a correlation between frequency harmonics and circumferential modes.

The result of the 2D DFT applied to CFD probes at Station 10 is shown in Figure 42. Two dominant frequency harmonics are observed with significant amplitudes – the 21/rev (1*BPF) and 42/rev (2*BPF). Two dominant modes are observed at 21/rev frequency harmonic: +7 and

+21. The generation mechanism of these modes has been previously described in Section 4.3.2 with the help of Tyler-Sofrin theory.

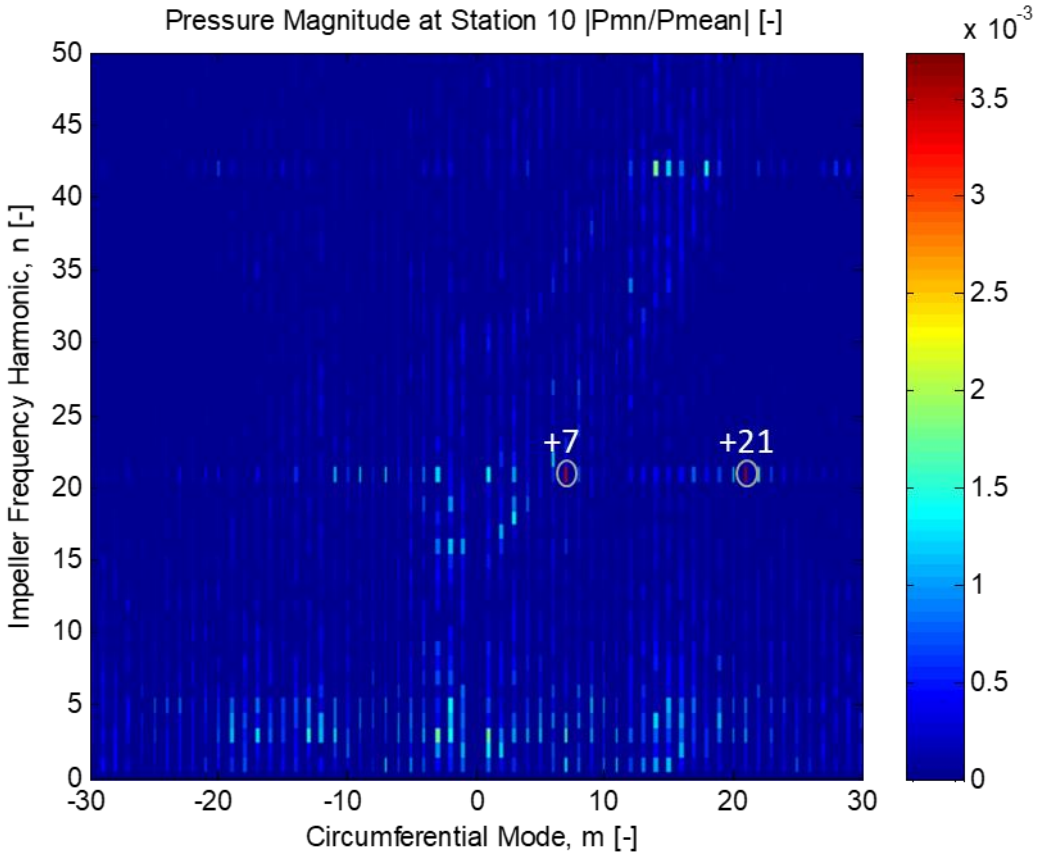

Figure 42 Unsteady pressure spectra of CFD probes at Station 10.

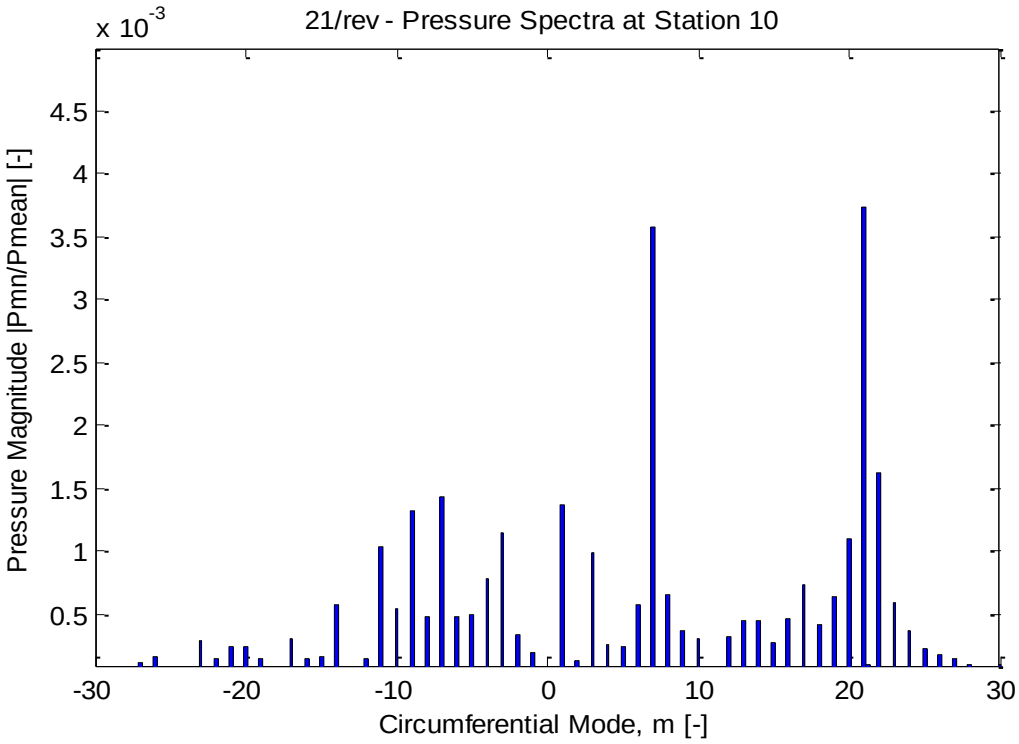

Figure 43 Unsteady pressure spectra at 21/rev (1*BPF) from the Station 10 probes.

The pressure spectra for impeller trailing edge probes presented in Figure 44 is representative of loading experienced by the impeller trailing edge. The CFD probes located at impeller trailing edge are in a coordinate reference frame rotating with the impeller whereas the probes at Station 10 and 30 are located in the stationary reference frame.

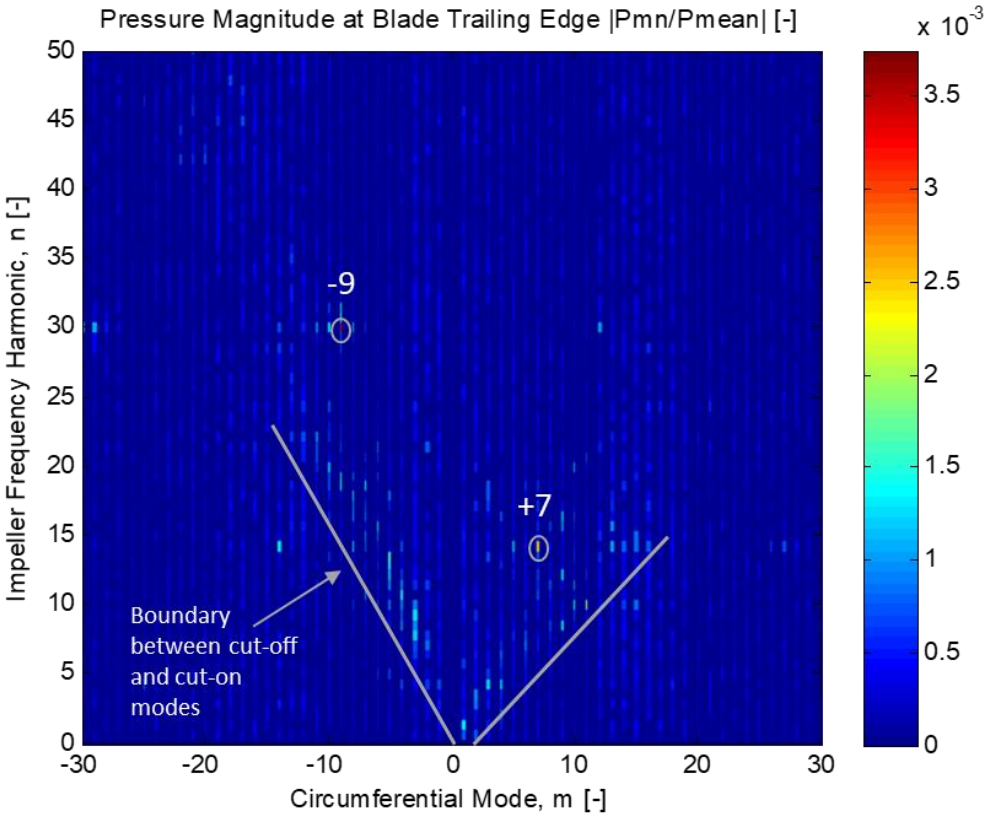

Figure 44 Two-dimensional pressure spectra obtained from impeller blade trailing edge probes.

Two dominant modes can be seen in Figure 44: +7 at 14/rev and -9 at 30/rev. Another important observation is that the 30/rev forcing measured at the impeller trailing edge during the experiments consists of a single dominant circumferential mode, m = -9. The propagation and reflection of +7 and -9 modes are visualised in Figure 47 and Figure 48, respectively.

The difference between frequency harmonic of +7 mode observed at Station 10 and at the blade trailing edge is due to the difference in the coordinate frame of reference for the probes. At impeller blade trailing edge, the acoustic modes spin relative to the impeller. The resulting doppler-shift changes the effective forcing frequency harmonic of the modes. The relative magnitude of -9 mode is higher than +7. The boundary between cut-on and cut-off modes is indicated, with a slightly unsymmetrical pattern between positive and negative modes. This is due to flow swirl effects.

Figure 45 presents the results for a similar analysis performed at Station 30 probes. The probes are located in a stationary frame of reference; hence, dominant modes are observed that 21/rev (1*BPF). Unlike blade trailing edge probes, the relative amplitudes of +7 and -9 modes are comparable with +7 mode being slightly stronger than the -9 mode (refer Figure 46). The presence of +7 mode at Station 30 suggests that this mode is cut-on and therefore, can propagate in the return channel. -9 mode is generated due to the reflection of the +7 mode from the downstream de-swirl vanes. This conforms to the Tyler-Sofrin relation given in Equation 2.5 using the values: m = +7 (incident acoustic mode), V = 16 (downstream de-swirl vane-blade count) and the integer value k' = -1 (de-swirl vane frequency harmonic). The resulting -9 mode is reflected upstream causing the 30/rev excitation at the impeller trailing edge. The mode visualisations are presented in the following section.

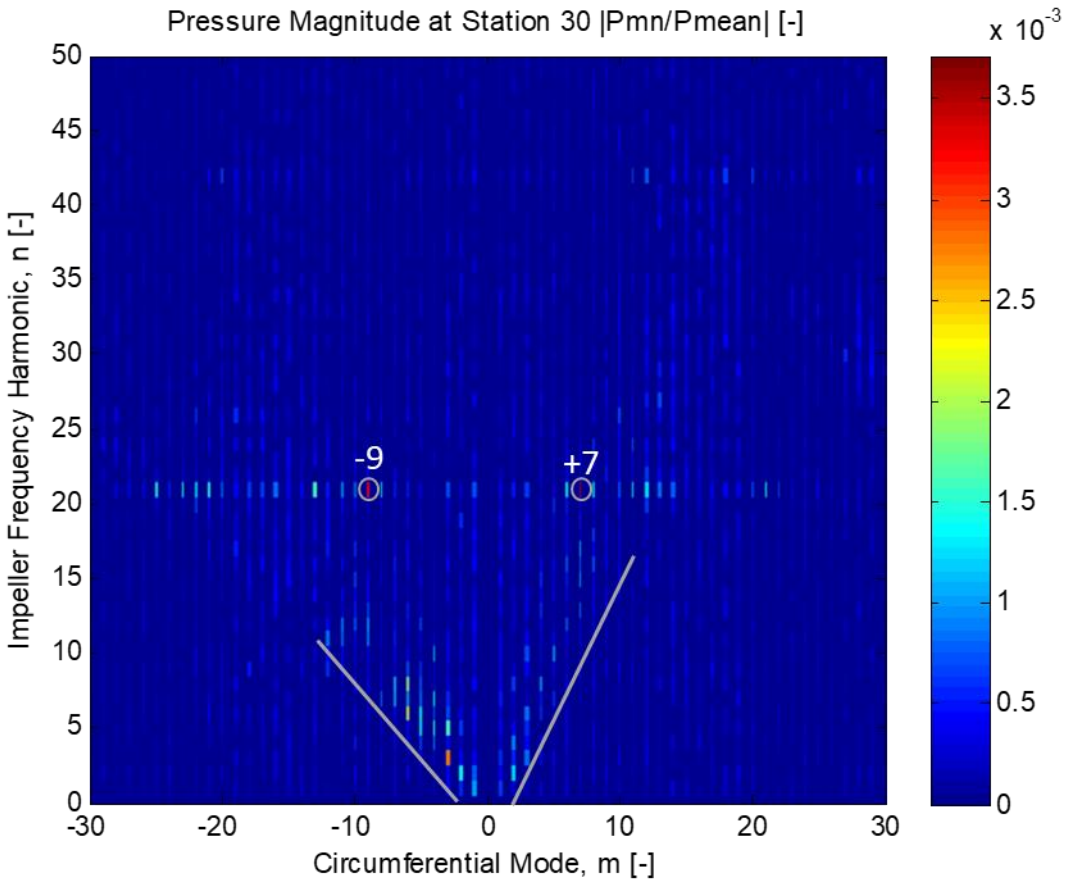

Figure 45 Two-dimensional pressure spectra obtained from probes at Station 30.

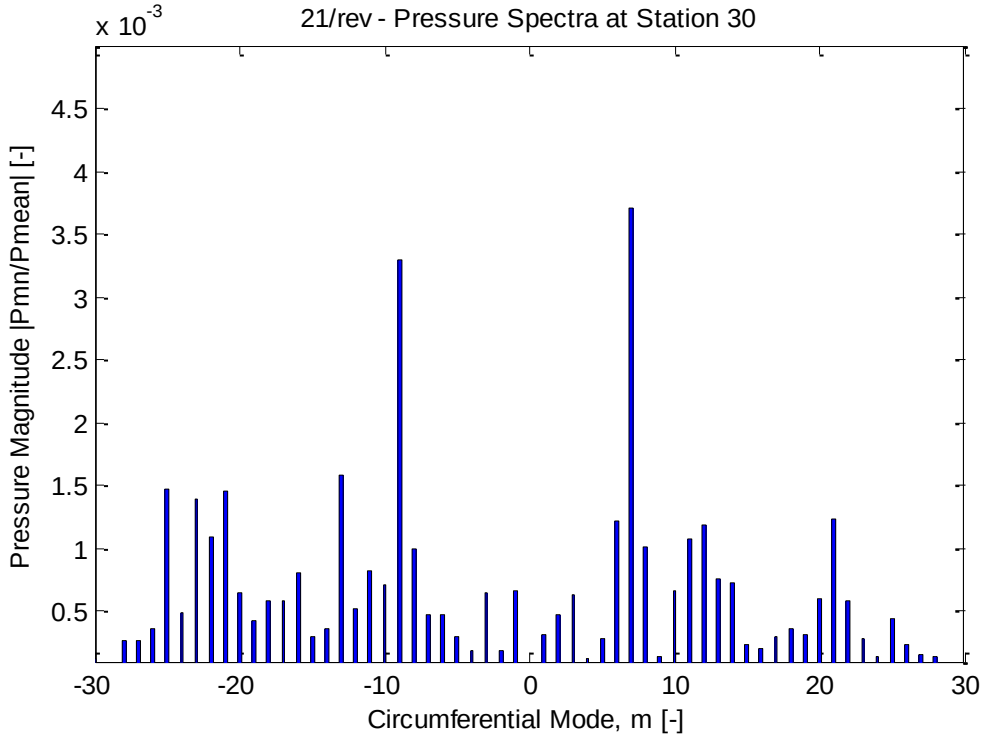

Figure 46 Unsteady pressure spectra at 21/rev from the Station 30 probes.

5.4.2 Acoustic mode visualisation

The second step in the acoustic analysis was to visualise shapes and propagation of the dominant modes obtained in step one. This has been achieved by applying a band-pass filter to the time derivative of pressure derived from the CFD simulations. The frequency band is varied in the range of interest to capture the dominant modes. The +7 mode (14/rev) is visualised on the symmetry plane in Figure 47. The direction of propagation in the ducts is indicated using arrows. It is cut-on in both inlet and outlet ducts and therefore, propagates in both directions.

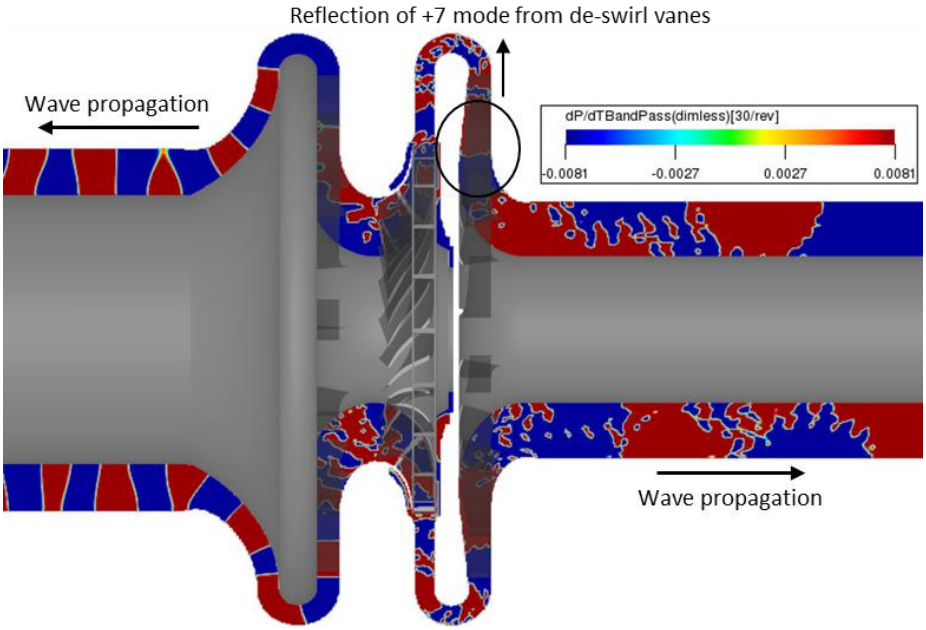

Figure 47 +7 mode visualization on the symmetry plane (14/rev). The direction of wave propagation and reflection is indicated with arrows.

The partial reflection of +7 mode from the de-swirl vanes downstream of the impeller leads to the generation of the -9 mode, which is the 9 lobed spinning pressure pattern that caused the 30/rev vibratory response in the impeller blade trailing edge. This observation is supported by

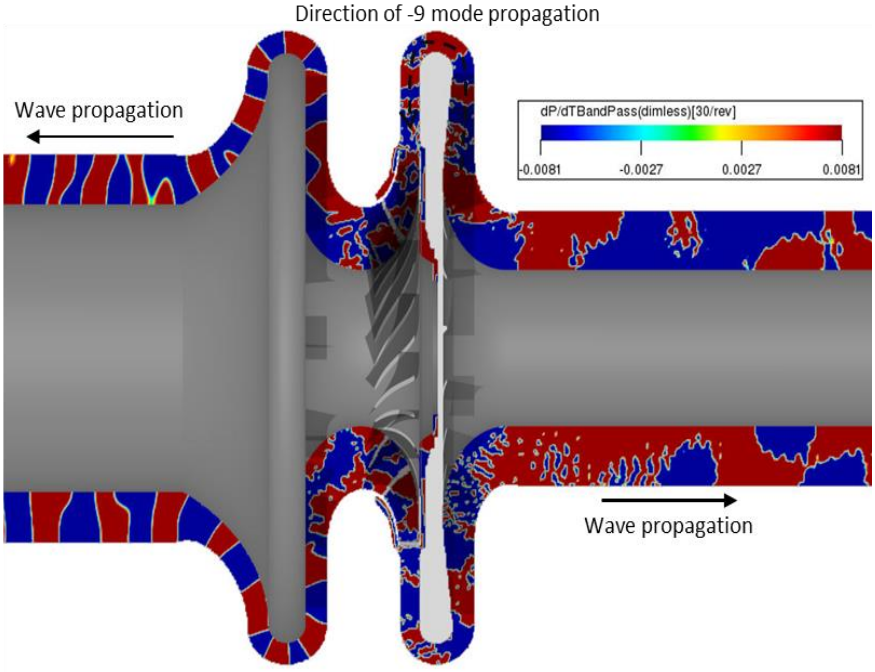

Figure 48 -9 mode visualisation on the symmetry plane (30/rev). The direction of wave propagation is indicated with arrows.

the Tyler-Sofrin theory as described in the previous section. -9 mode is visualised on the symmetry plane in Figure 48. The acoustic wave propagation is faster downstream of the impeller due to the speed of sound effects. -9 mode is also cut-on in both inlet and outlet ducts. Remarkably, the frequency of -9 mode matches with the frequency of impeller blade trailing edge vibratory response observed in experiments performed by Richards et al. [4]. This satisfies the first condition of the aeromechanic co-incidence mentioned in Section 2.6. The acoustic mode shapes will now be visualized and compared with structural eigenmodes to assess the validity of the second condition of the aeromechanic coincidence.

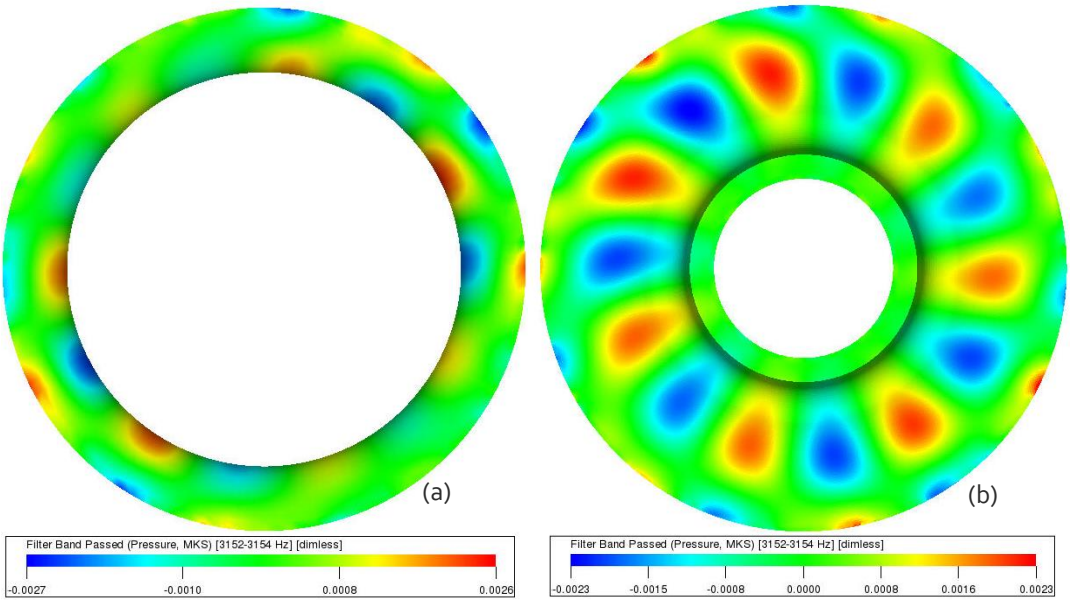

Figure 49 Shroud and hub side cavity acoustic modes (m=+7). (a) Shroud side cavity. (b) Hub side cavity

The +7 acoustic mode at cavity faces is shown in Figure 49. The acoustic mode is mainly localised to hub side cavity. 7 nodal diameters can be seen on the hub cavity surface in Figure 49 (b). One nodal circle is observed on both the hub and shroud side cavity faces.

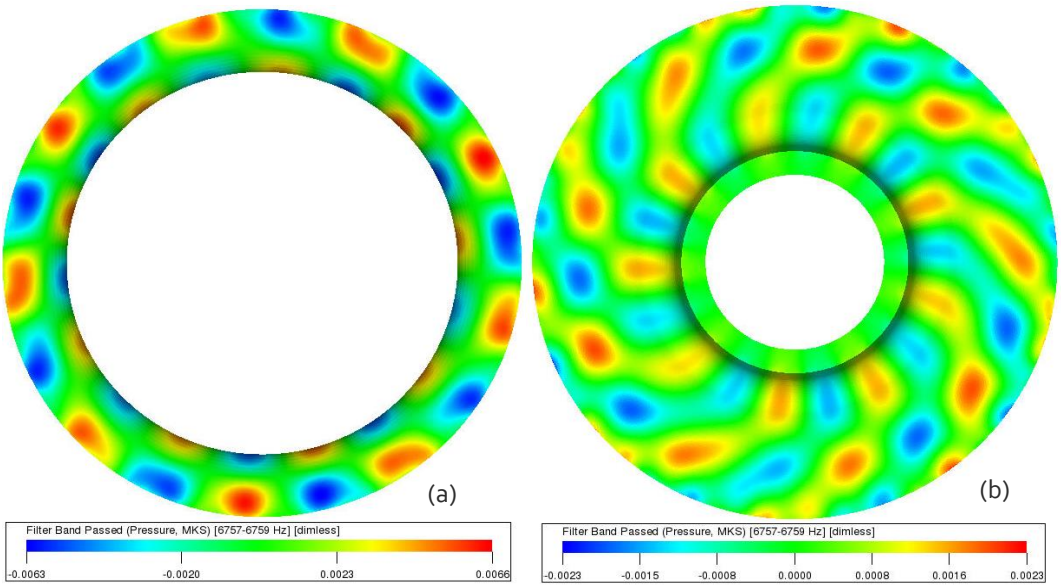

Figure 50 Shroud and hub side cavity eigenmodes (m=-9). (a) Shroud side cavity. (b) Hub side cavity

Figure 50 shows -9 acoustic mode at shroud and hub side cavity faces. This mode is coupled to both side cavities with a stronger coupling to the shroud side cavity. 9 nodal diameters are observed in both the cavity faces. Shroud side cavity modal distribution exhibits 1 nodal circle

whereas, 2 nodal circles are seen in the hub side cavity modal distribution. The -9 acoustic modal distribution shows a good correlation with the F2 structural eigenmode shape shown in Figure 2. Comparing the acoustic and structural mode shapes, it is clear that the acoustic forcing is in-phase with the structural mode. This satisfies both conditions for aeromechanical coincidence as described in Section 2.6. The skewed shape of this mode on hub cavity face can be attributed to the effects of fluid rotation.

5.5 Cavity forced response analysis

Cavity forced response analysis was performed for OP 30/rev by performing frequency sweeps in the hub and shroud cavity to detect individual resonant peaks. The time derivative of pressure was band-passed at different frequency bands close to 30/rev frequency, i.e. 6758 Hz to obtain peak frequencies, amplitudes, and mode shapes. This provided valuable insights into side cavity modal coupling.

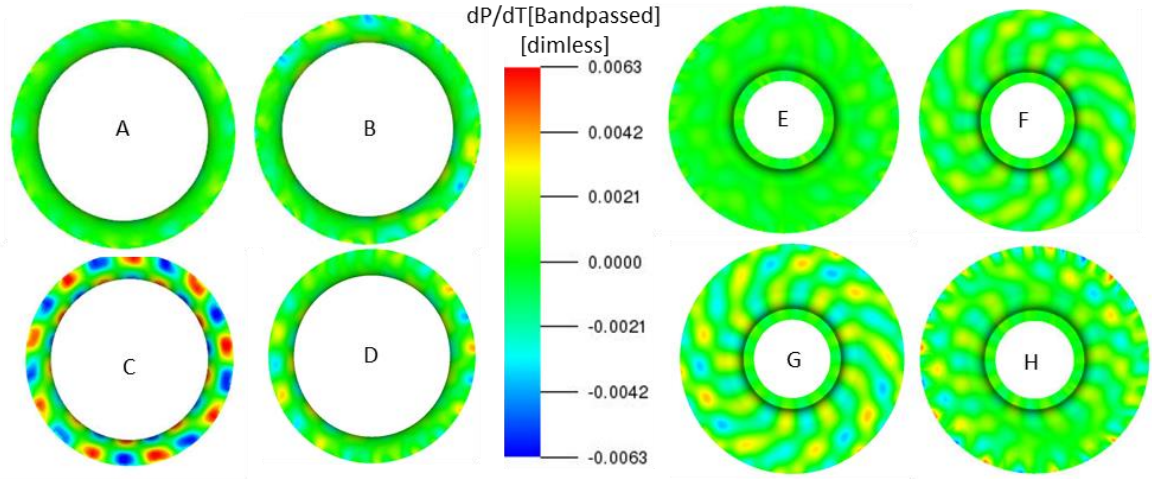

Figure 51 Band-passed pressure on the shroud (A-D) and hub (E-H) side cavity faces close to 30/rev frequency. Contours are coloured by normalized peak pressure amplitudes. A-H denote different frequency bands.

Figure 51 (A-D) presents results for acoustic mode pressure distribution for the shroud side cavity surface for four different frequency bands. Figure 52 presents the normalised shroud cavity peak pressure amplitudes for various frequencies close to 30/rev. The amplitudes are normalised to the peak amplitude on both the faces. Frequencies A-D are marked in the plot. Shroud side cavity exhibits a sharp peak at point C, which is about 6488 Hz.

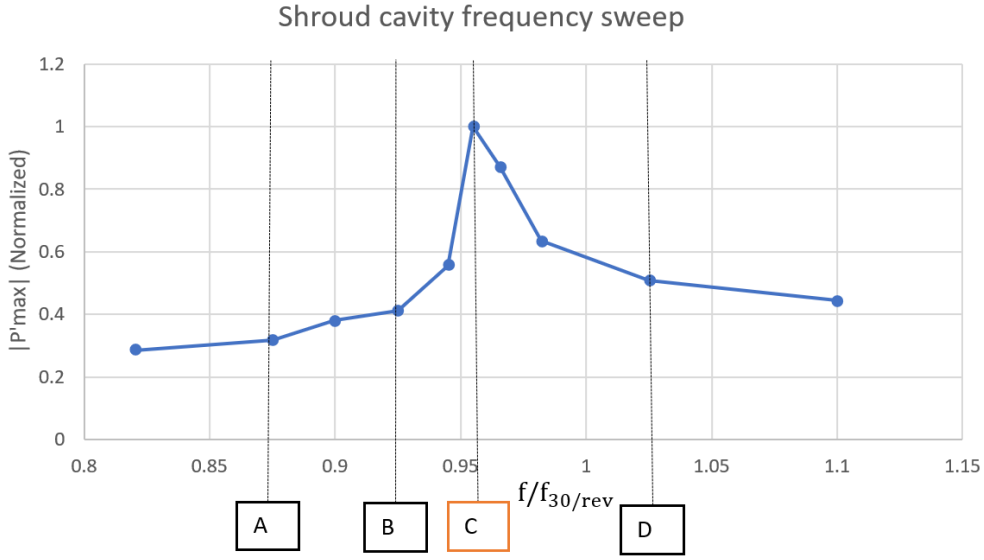

Figure 52 Unsteady pressure peak magnitude for the shroud side cavity.

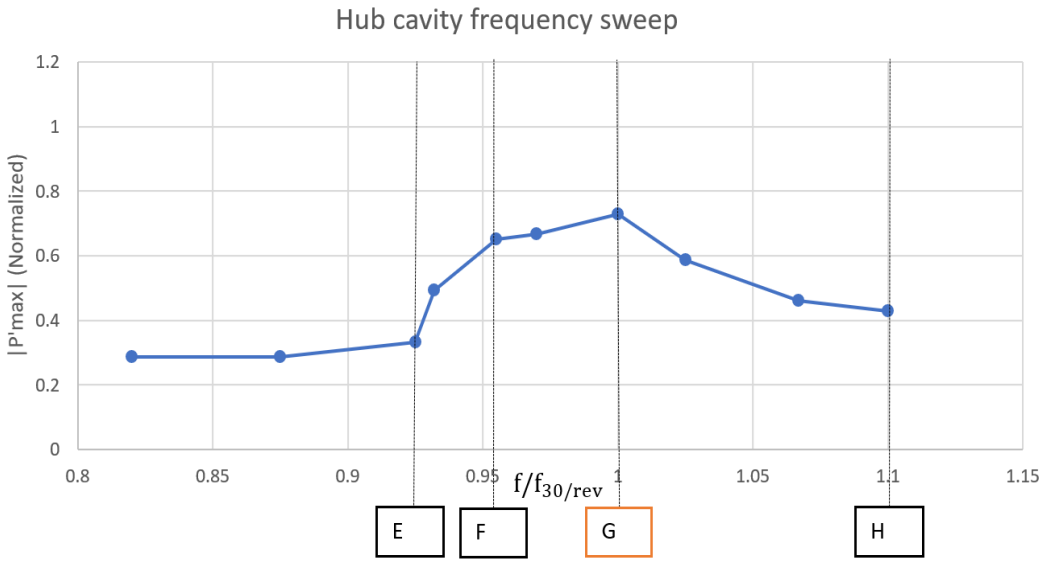

Figure 53 Unsteady pressure peak magnitude for the hub side cavity.

Figure 51 (E-H) presents results for acoustic mode pressure distribution in case of the hub-side cavity. The figures are coloured by normalised peak pressure amplitudes. Unsteady pressure amplitudes for frequencies E to F for the hub side cavity are plotted in Figure 53. Unlike the shroud side cavity, a broad peak is observed with a significant level of acoustic energy at off-resonant frequencies. This behaviour is characteristic of damped acoustic resonators, indicating that acoustic energy is dissipated at the mouth of the cavity. Another difference is the difference in modal pressure distribution between hub and shroud side cavities. Shroud side cavity exhibits 1 nodal circle whereas, 2 nodal circles are observed in the hub side cavity (refer Figure 50). The difference in surface area of the cavity faces can also explain this behaviour. Furthermore, friction losses are higher due to the large surface area of the hub-side cavity.

5.6 Resonant amplification factor calculation

As described in Chapter 2, acoustic resonances in centrifugal compressors may amplify excitation sources. The resultant structural vibratory response described in Equation 2.1 is dependent on source strength, resonant amplification factor and the damping. Therefore, the resonant amplification factor is a key parameter governing the severity of the aeromechanical coincidence.

5.6.1 Technical approach 1: changing impeller rotational speed

The resonant amplification factor has been computed by simulating following operating points:

Case	Impeller Rotational Speed [RPM]	Flow coefficient [-]	Work coefficient [-]
A	13331	0.0955	*0.5711*
B	14958	0.0956	*0.5791*

Table 8 Test matrix for resonant amplification factor estimation.

The two operating points have different impeller rotational speeds and peripheral Mach numbers. It is seen from Figure 16 that case A is close to OP 30/rev, whereas case B is close to IP 30/rev.

Both the cases were simulated using the same technical approach described in Chapter 2. Two approaches have been implemented for the calculation of the resonant amplification. Firstly, dominant Tyler-Sofrin mode amplitudes were compared for both operating conditions. 2D DFT was performed at Station 30 CFD probes. This provided valuable insights into the relative mode amplitudes. Secondly, SPL at Station 30 also compared for both cases.

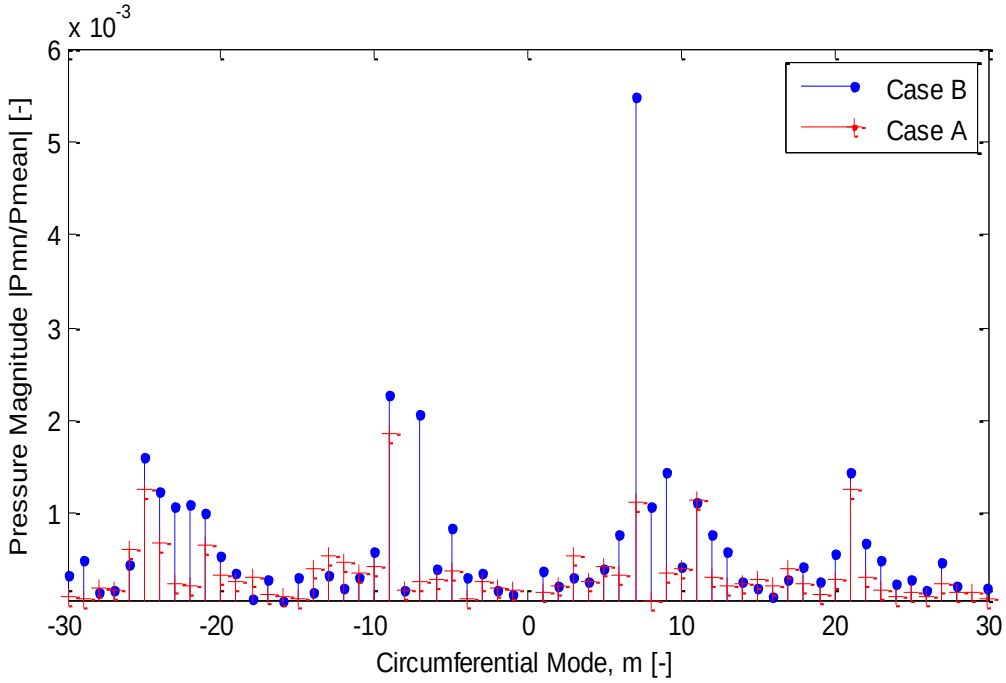

Figure 54 Resonant ampltification factor estimation: unsteady pressure spectra from Station 30 probes at 21/rev (BPF) for case A and B.

Figure 54 presents the results for the 21/rev (BPF) modes extracted from the 2D FFT. +7 and -9 are the two modes of interest in this investigation as they are the dominant Tyler-Sofrin modes. It is seen that the amplitude of -9 mode is unaffected while +7 is significantly stronger for case B.

Quantitatively, +7 mode for case B is 5 times stronger than case A. Therefore, the resonant amplification factor is 5. SPL at Station 30 was amplified by 8.8 dBs at the resonant operating condition.

Case	SPL (Station 30) [dBs]	Normalized +7 mode amplitude (Station 30) [-]
A	150.3	0.0011
B	159.1	0.0056

Table 9 Results from resonant amplification factor simulations.

5.6.2 Technical approach 2: changing de-swirl vane count

In the previous methodology, forcing function was varied by changing the impeller rotation speed. This changed the tip Mach number and hence, the frequency and amplitude of the noise sources. In this approach, the compressor operating conditions are unchanged; therefore, resonant amplification is calculated for the same source amplitude.

A new compressor geometry was designed where the de-swirl vane count downstream of the impeller was reduced from 16 vanes in the original configuration to 15 vanes. As known from

the previous discussions, -9 mode is generated from the reflection of +7 mode from the 16 de-swirl vanes in the return channel. A change in de-swirl vane count excites other modes apart from -9. This is seen in Figure 55, where 21/rev – BPF modes at Station 30 are presented from both compressor configurations.

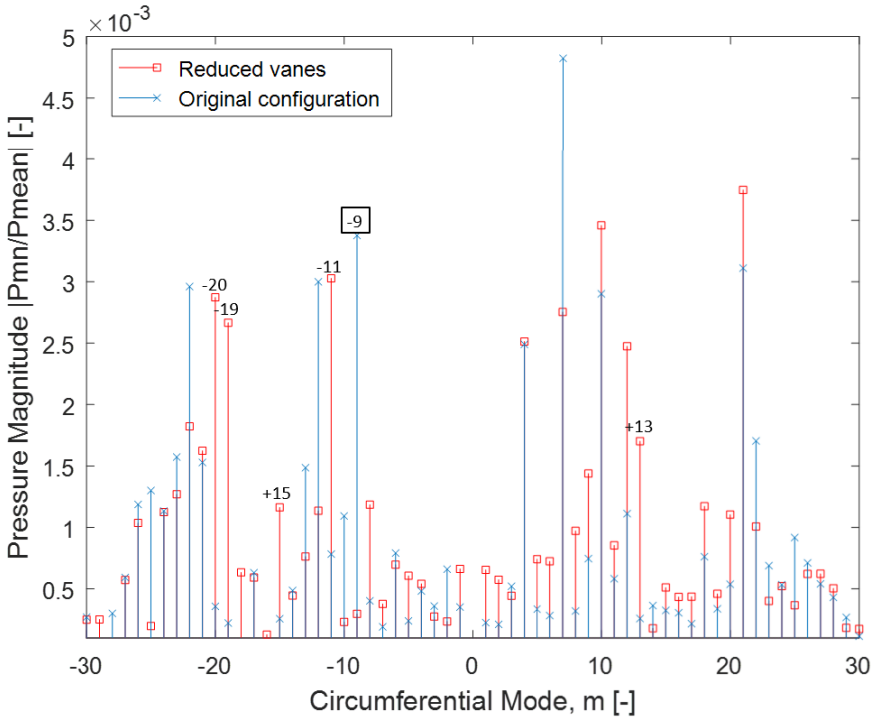

Figure 55 Effect of changing de-swirl vane count on 21/rev (BPF) modes at Station 30.

As expected, the amplitude of -9 mode is reduced by 14 times in the reduced vane configuration. Modes -20, -19, -11, +15 and +13 are amplified in the new configuration. These are Tyler-Sofrin modes generated from the interaction of cut-on modes at Station 10 with the first two harmonics of the new VPF. For example, m = -11 is generated due to the interaction of +4 mode with the de-swirl vanes downstream of the impeller. This conforms to the Tyler-Sofrin relation given in Equation 2.5 using the values: m = +4 (incident acoustic mode), V = 15 (downstream de-swirl vane-blade count) and the integer value k' = -1 (de-swirl vane frequency harmonic). No differences are found in the SPL at Station 30.

6 Conclusions and Recommendations

6.1 Conclusions

The goal of this research was to develop and validate a computational strategy to quantify impeller forcing amplitude in a centrifugal compressor operating at conditions of acoustic resonance. A comparison study was performed between a conventional URANS based technique and a state-of-the-art LBM based technique to assess their capabilities in modelling centrifugal compressor aeroacoustics for the same number of CPU hours. LBM performed better in predicting both the performance, as well as the unsteady pressure amplitudes for similar number of CPU hours. Therefore, the LBM based technique was chosen for a comprehensive aeroacoustic analysis of the research compressor.

The complete 360^0 compressor geometry is simulated including cavity flows to account for acoustic resonances. Measurement probes were distributed near the impeller leading, trailing edge, and in the return channel. The temporal and spatial variation in pressure was decomposed into a sum of Fourier modes. This characterised the flow physics governing the root cause and amplitude of the unsteady pressure loading amplitudes on blade and vanes, which will aid in identifying possible aeromechanic coincidences in centrifugal compressors.

For the first time, a state-of-the-art LBM based technique was used to directly capture pressure fluctuations in the vicinity of impeller blade of a centrifugal compressor impeller. Pre-swirl vanes were not directly modelled to save the required amount of computational resources. Their effect was modelled by imposing a co-rotating swirl at the compressor inlet. It significantly improved stage performance predictions and resulted in reduced blade row interaction, decreasing the mode amplitudes at Station 10, blade trailing edge, and at Station 30. The SPL at Station 30 was underpredicted by 3.5 dBs in comparison with test rig data. The physical modelling of pre-swirl vanes resulted in considerable improvements in the performance as well as acoustic predictions.

Tyler-Sofrin modes generated from blade-row interaction were found to be the root cause of high impeller excitation observed during the experimental campaign. Dominant acoustic modes obtained from two-dimensional DFT were visualised successfully. This is one of the key aspects of assessing the severity of aeromechanical coincidence in centrifugal compressors. The presence of +7 mode at Station 10 upstream of the impeller proves that it originates due to the interaction of upstream de-swirl vane rows with the impeller. +7 mode is cut-on and therefore is able to propagate in the return channel. The reflection of +7 mode from de-swirl vanes downstream of the impeller leads to the generation of -9 mode. These findings are supported by Tyler-Sofrin theory and are successfully visualised from CFD results. The frequency as well as mode shape (number of nodal circles and diameters), of -9 mode on shroud side cavity face matched with its structural eigenfrequency and mode shape, thus satisfying both conditions for a severe aeromechanical coincidence.

Side cavity mode coupling is studied by performing frequency sweeps in both cavities around the 30/rev frequency — this enabled insight into the individual resonant frequencies of the cavities. Shroud side cavity showed a narrow peak at 0.96*30/rev frequency. Hub cavity exhibits a relatively broad peak with significant acoustic activity at off-resonant conditions. This

behaviour is found to be consistent with that of a damped acoustic resonator. A possible cause for this behaviour can be acoustic energy dissipation at the mouth of the cavity in the CFD model. In summary, the hub and shroud side modes are coupled.

Another important outcome of this research is the computation of resonant amplification factor. Two technical approaches were implemented. Firstly, the frequency of the forcing function was changed by changing the compressor RPM. The two operating points were simulated with the same flow and work coefficients. Resonant modal amplitudes were compared for both operating conditions. SPL at Station 30 increased by 8 dBs at resonant conditions. The limitation of the first approach is that due to changes in impeller tip Mach number, noise sources are changed. This was improved in the second methodology where the de-swirl vane count was reduced from 16 vanes in the original configuration to 15 vanes. As a result, new Tyler-Sofrin acoustic modes were excited and -9 mode (30/rev) amplitude was reduced by a factor of 14. SPL at Station 30 was unaffected in this approach.

The most important outcome of this project is the creation of a simulation framework that is capable of modelling aeroacoustic interaction in centrifugal compressors. This research also shows that severe aeroacoustic forcing can exist even in low-pressure ratio centrifugal compressor stages. This adds to the body of knowledge on centrifugal compressor aeroacoustics. Such a simulation strategy would lay the groundwork for future aero-mechanical studies on centrifugal compressors to estimate the vibratory response of impeller blades. Aero-mechanic difficulty in centrifugal compressors is a concern for automotive, oil-gas and aerospace industry alike where centrifugal compressors are used for their compactness and ability to operate at high-pressure ratios.

The research questions of this thesis are answered as follows:
What are the mechanisms governing the forced vibratory response in the research compressor?

Answer: Tyler-Sofrin modes generated from blade row interaction caused high impeller blade vibratory response. +7 mode was generated from the interaction of inlet de-swirl vanes with the impeller. Being a cut-on mode, this mode propagates in the return channel and interacts with the exit de-swirl vanes. This leads to the generation of -9 mode which caused impeller blade trailing edge vibratory response.

What are the limitations of the current state of the art simulation strategy to quantify the aeroacoustic phenomenon in centrifugal compressors?

Answer:

1. *Exclusion of side cavities: Side cavity fluid dynamics is critical for quantification of acoustic resonant amplification of the source. Capturing the correct circumferential flow velocity is essential to simulate the phase relationship between side-cavity modes. Side cavity mode coupling has significant implications on impeller forcing.*
2. *Simulating a sector of the compressor wheel: Modelling the complete geometry is necessary to account for acoustic resonances. This is the root cause of impeller excitation in this case and the majority of cases in the published literature.*

How strong are the pressure forcing amplitudes due to rotor/stator interactions?

Answer: A pressure loading of 1430 Pa has been predicted from CFD simulations in this work. This multiplied by the surface area of the shroud side cavity gives a dynamic force of 63.14 N. This force acting at a high frequency of 6758 Hz caused high impeller vibratory response observed in the experimental campaign.

What is the resonant amplification factor for the research compressor?

Answer: The resonant amplification factor is computed to be 14 for the chosen research compressor.

Is an LBM based approach feasible for simulating centrifugal compressor aeroacoustics?

Answer: Yes, the LBM based approach has proved to be a suitable tool for this research. The stage performance predictions agreed well with test rig data. The unsteady pressure amplitude at Station 30 was underpredicted by 3.5 dBs. A 2D DFT applied to CFD pressure probes provided valuable insights into the frequency and amplitudes of the Tyler-Sofrin modes. Dominant modes were successfully visualised, gaining insight into the pressure distribution on the side-cavity faces.

6.2 Recommendations for future work

6.2.1 Recommendations for comparison study between URANS and LBM based approach

The extended inlet and outlet domain length might be insufficient for comparison study simulations. It was discovered later that both +7 and -9 modes are cut-on in the inlet and outlet ducts. Sufficiently large acoustic sponge zones are necessary to ensure minimal reflections from domain boundaries. This might have affected the acoustic amplitudes. Furthermore, a large domain size was infeasible due to the limited availability of computational resources. The domain size of the LBM simulation was reduced as well to match the computational time in the URANS based approach. Another limitation in the comparison study was the lack of a swirl inlet boundary condition, which made it difficult to compare results with the experimental data. Both of these limitations were improved in the comprehensive LBM simulation results presented in Chapter 5.

Availability of limited computational resources for URANS simulation posed severe limitations on the choice of grid size and time step. To make a direct comparison between the techniques, grid-converged solutions must be compared at the same time step. Time step plays a key role in capturing the unsteady flow phenomenon and governs the temporal resolution of the unsteady pressure probes in CFD. It must be noted that the computational efficiency of the LBM based approach is significantly higher as compared to the URANS based approach. This allowed a much finer spatial and temporal resolution in LBM for the same number of CPU hours. This might have adversely impacted the stage performance as well as acoustic predictions. A fair comparison requires detailed studies on case-setup related effects such as temporal and spatial discretisation, numerical schemes, turbulence modelling etc. A better standard than CPU hours may be chosen in future investigations. For instance, a structured grid may be used in URANS simulations with constant cell size across the flow domain. This would ensure grid similarity between the schemes.

6.2.2 Recommendations for the numerical simulations

Being a low-pressure ratio operating condition, OP-30/rev might not be the best choice for the stage performance validation. Therefore, higher pressure ratio operating conditions can be simulated to assess the feasibility of LBM for performance prediction of centrifugal compressors.

A more practical approach is required to detect aeromechanical coincidences early in the design phase. Centrifugal compressors are uniquely designed for each application in the oil and gas industry. It is infeasible to run such resource-intensive CFD calculations for each possible aeromechanical coincidence in the machines. Therefore, more studies are required

to develop a more practical approach, for example by using simplified models. This work is a small step towards providing the physical insight needed to develop such models.

6.2.3 Recommendations for the experimental campaign

Only two unsteady pressure sensors were mounted at Station 30 in the experiments, which made it impossible to extract the mode amplitudes. Therefore, mode amplitudes from CFD could not be compared with the experimental data. An array of unsteady pressure transducers should be mounted in future experimental campaigns to allow in-depth studies on the agreement/disagreement with CFD.

Appendices

A. Dimensionless unit definitions

Variable	Definition	MKS Units	Dimless Unit Definition
Lambda2 (λ_2)	*Refer A.1.*	$\frac{1}{s^2}$	$\frac{\lambda_2}{(\frac{L_c}{u_c})^2}$
Static Pressure	p	$kg/s^2.m$	$\frac{p-p_c}{q_c}$
Total Pressure	$p+\frac{1}{2}\rho u^2$	Pa	$\frac{p+\frac{1}{2}\rho u^2-p_c}{q_c}$
Total Temperature	T	K	$\frac{T-T_c}{T_c}$
Turbulent Kinetic Energy	u'^2	m^2/s^2	$\frac{u'^2}{u_c^2}$
Vorticity Magnitude	$\nabla * \mathrm{u}$	$\frac{1}{s}$	$\frac{\nabla * \mathrm{u}}{u_c/L_c}$

Table 10 Dimensionless unit definitions [93].

The following symbols are used in variable definitions [93]:

L_c	Characteristic length
p_c	Characteristic Pressure
q_c	Characteristic dynamic pressure
t_c	Characteristic Temperature
u'	Turbulent velocity fluctuation
u_c	Characteristic velocity
p	Pressure
t	Temperature
ρ	Density

Table 11 List of symbols used in unit definitions [93].

A.1. Lambda2 (λ_2) definition

λ_2 is defined as the second largest eigenvalue of $S^2+\Omega^2$, where S is the symmetric deformation tensor:

$$S_{ij}=\frac{1}{2}(\frac{\partial v_i}{\partial x_j}+\frac{\partial v_j}{\partial x_i}) \quad \text{(A.1)}$$

and Ω is the anti-symmetric spin tensor:

$$\Omega_{ij}=\frac{1}{2}(\frac{\partial v_i}{\partial x_j}-\frac{\partial v_j}{\partial x_i}) \quad \text{(A.2)}$$

B. Addition of upstream pre-swirl vanes

B.1. Model definition and case Setup

As discussed previously, the effects of pre-swirl vanes upstream of the impeller was modelled with imposing a co-rotating swirl at the mass-flow inlet boundary condition. In this case, 17 pre-swirl vanes were physically added to avoid this modelling simplification. The updated case setup can be seen in Figure 56. The pre-swirl vanes have been highlighted in yellow. Extra fine grid resolution reported in Table 2 was used. Data acquisition was performed similarly as previously described in Section 3.3.

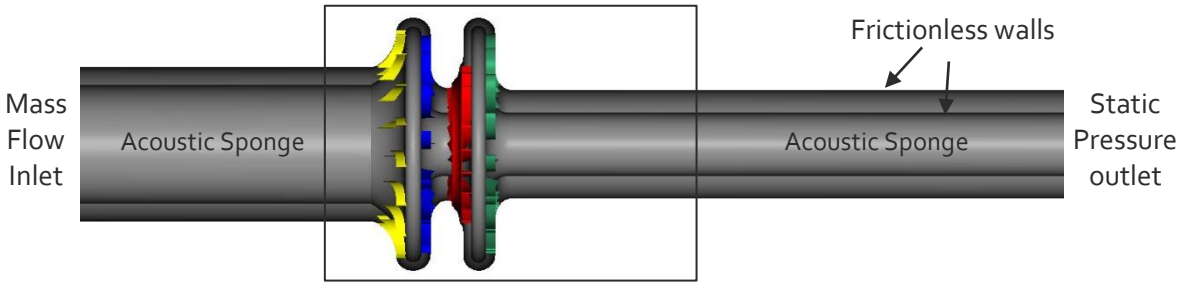

Figure 56 Computational setup with pre-swirl vanes highlighted in yellow.

B.2. Effects on the flow field

Surface contour of time-averaged velocity magnitude is shown in Figure 57. Interaction of pre-swirl vane wakes with de-swirl vanes is visible. Addition of pre-swirl vanes amplifies the hydrodynamic interaction between the vane rows upstream of the impeller. The resulting wakes are able to propagate up to the impeller inlet. The effects on acoustics are addressed in the next section.

Time-averaged total pressure contour is shown on the symmetry plane in Figure 57. Adding pre-swirl vanes introduced additional pressure losses into the compressor system. This caused a further reduction in total pressure at Station 10 and therefore, increased the predicted stage total pressure ratio.

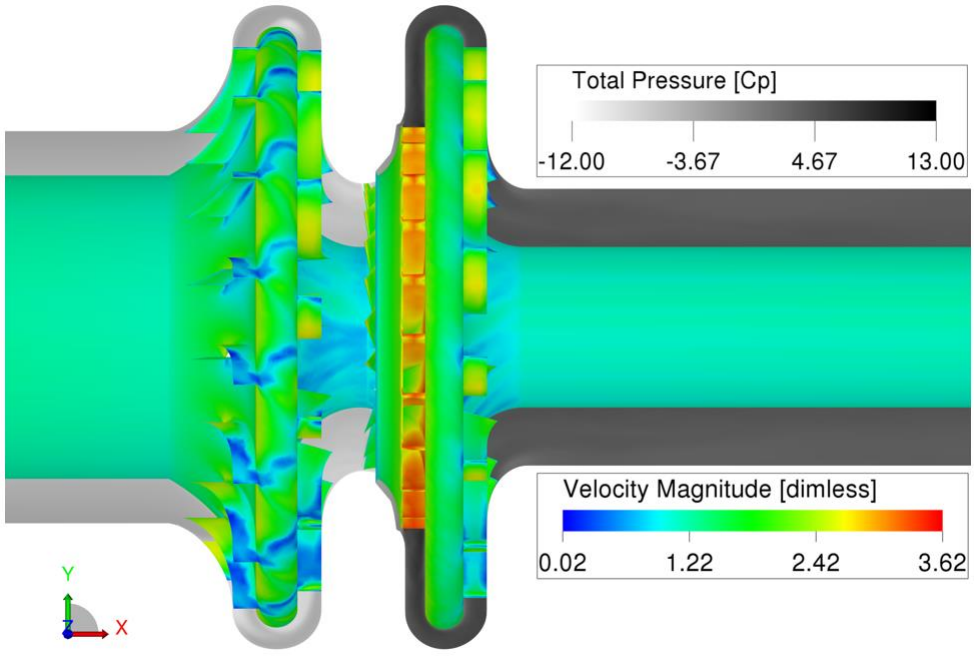

Figure 57 Velocity magnitude and total pressure contours.

Figure 58 shows the time-averaged distribution of the total temperature on the symmetry plane. The highest temperature is observed in the side cavities. The radial temperature gradient observed previously in the swirl-inlet case is less in comparison with without pre-swirl vanes case.

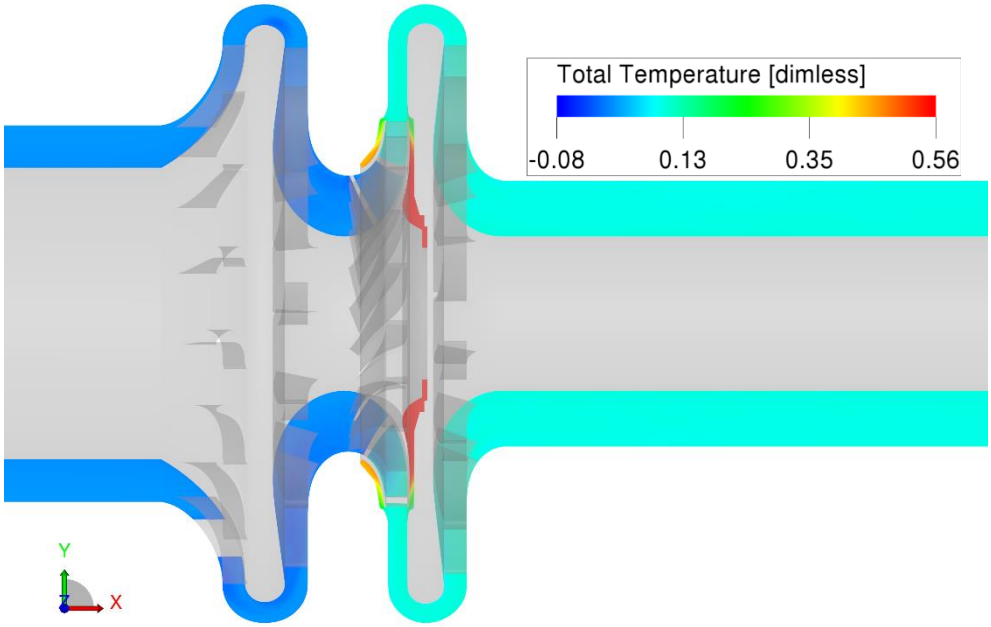

Figure 58 Time-averaged total temperature on the symmetry plane.

B.3. Effects on the acoustics

The Tyler-Sofrin rule can be re-written for four compressor blade rows as follows:

$$m = n_1 V_1 \mp n_2 V_2 \mp n_3 B_3 \mp n_4 V_4, \quad n_1, n_2, n_3, n_4 \in \{\dots, -2, -1, 0, 1, 2, \dots\} \tag{B.1}$$

For the new compressor configuration, V_1, V_2, and V_3 represent the upstream pre-swirl, de-swirl and downstream de-swirl vane counts respectively. B_3 represents the impeller blade count. n_1, n_2, n_3 and n_4 represent the upstream pre-swirl vane passing frequency (VPF), de-swirl VPF, impeller blade passing frequency (BPF) and downstream de-swirl vane passing frequency (VPF) harmonics respectively. For this compressor configuration V_1 = 17, V_2 = 14, B_3 = 21 and V_4 = 16.

In this section, the effects of the addition of pre-swirl vanes on acoustics are studied. Firstly, the results of 2-D pressure spectra obtained from probes at Station 10 and 30 are shown. Then, the BPF modes at Station 30 are compared with the swirl-inlet case discussed previously in the report. Tyler-Sofrin rule is used to highlight the modes resulting from blade-row interactions.

2-D pressure spectra obtained from Station 10 CFD probes is shown in Figure 59. The 21/rev (BPF) modes are shown in Figure 60. The amplitude of m = +21 (rotor only mode) is amplified, whereas +7 mode amplitude is unaffected. Addition of pre-swirl vane row excites +4 mode, which was not observed in the swirl-inlet case. This mode fits the Tyler-Sofrin rule given in Equation B.1 using n_1 = 1, n_2 = 0, n_3 = -1, and n_4 = 0. Therefore, this mode is generated by the interaction of pre-swirl vane wakes with the impeller.

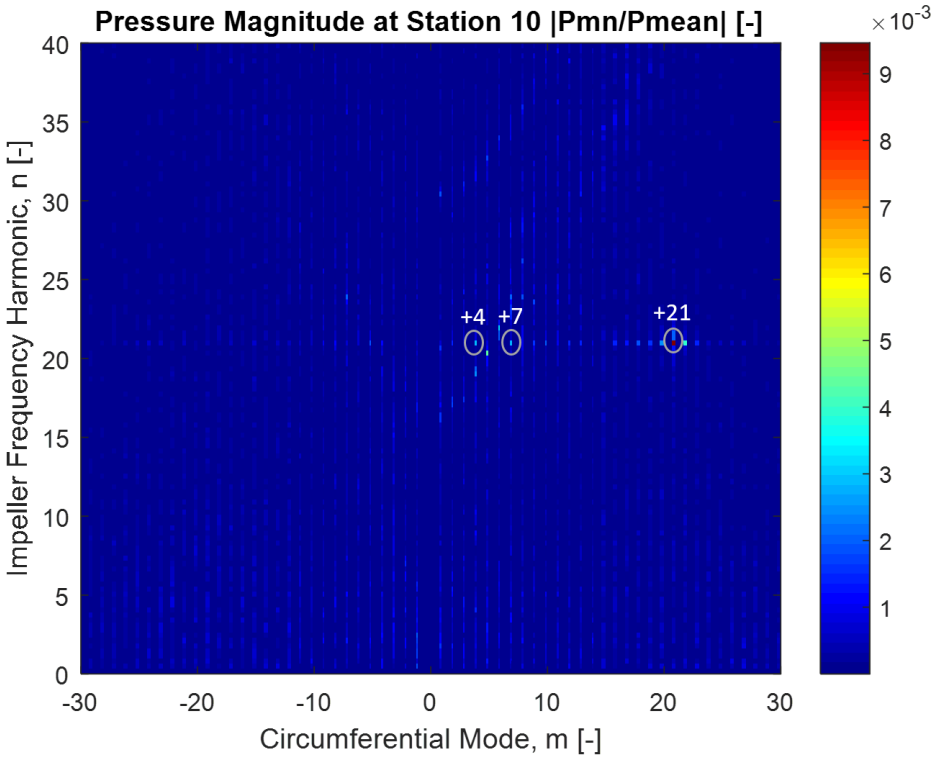

Figure 59 2D Pressure Spectra at Station 10 probes – with pre-swirl vanes.

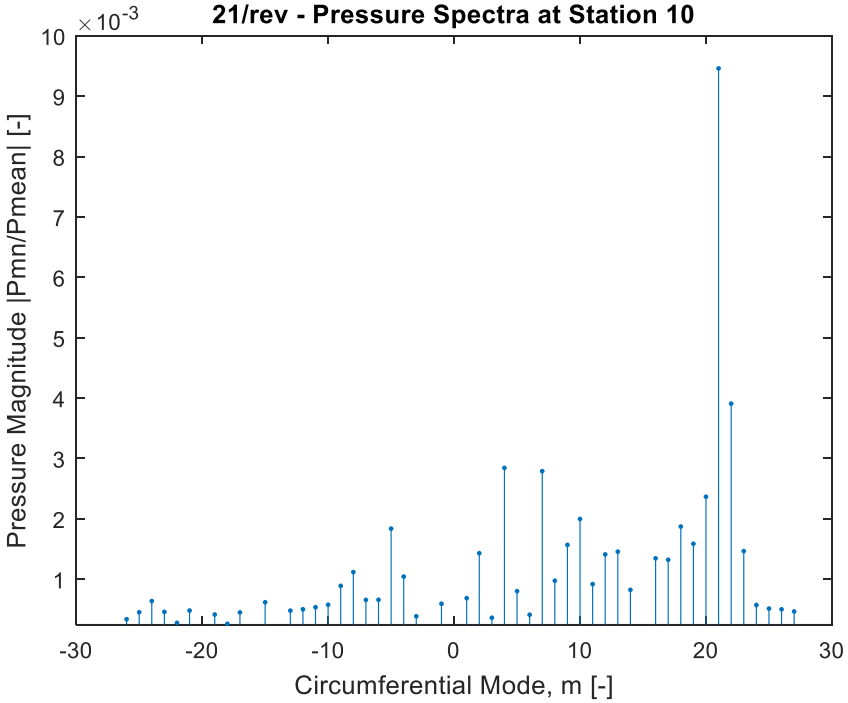

Figure 60 21/rev (BPF) modes at Station 10 – with pre-swirl vanes.

2-D pressure spectra obtained from Station 30 CFD probes is shown in Figure 61. The 21/rev (BPF) modes are shown in Figure 62. Two dominant frequency harmonics are observed: 21/rev – 1*BPF and 42/rev -2*BPF. Addition of pre-swirl vanes excites various new Tyler-Sofrin modes. These are highlighted in Figure 61.

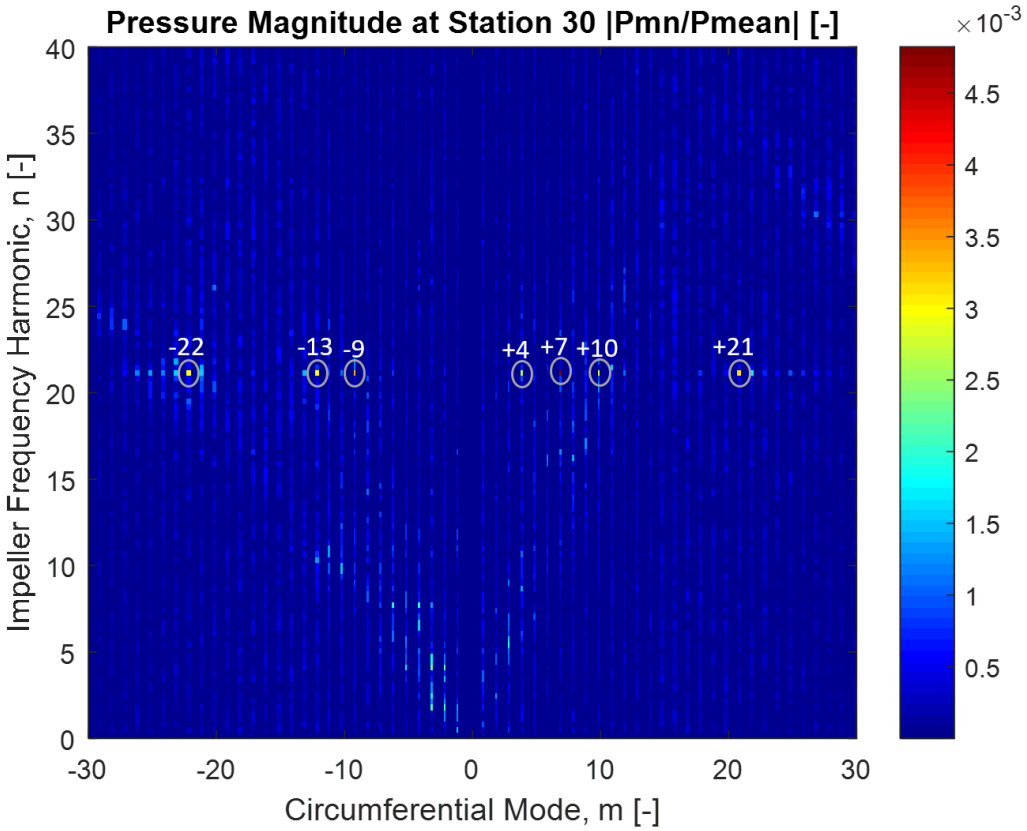

Figure 61 2D pressure spectra at Station 30 – with pre-swirl vanes.

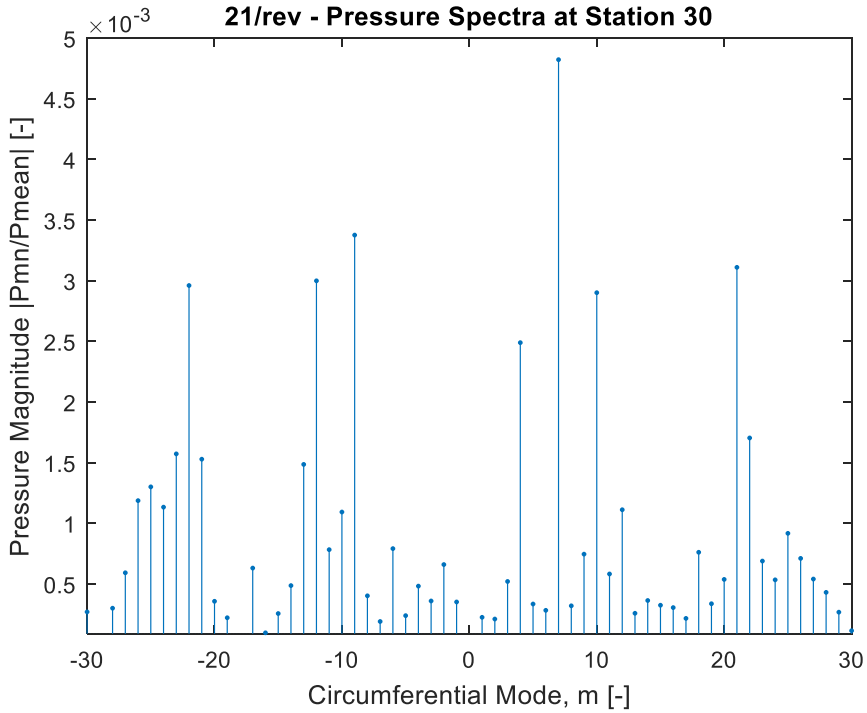

Figure 62 21/rev (BPF) modes at Station 30 – with pre-swirl vanes.

The comparison of BPF modes with the swirl-inlet case is shown in Figure 63. +7 mode is amplified whereas, the amplitude of -9 mode is unaffected. This corroborates findings of Gonzalez et al. [5] where they performed a simple eigen-frequency analysis to detect acoustic resonances in the compressor cascade. They hypothesised that the amplitude of -9 mode is

dominated by the side cavity acoustic resonance and suspected a weak dependency on the +7 mode (source) amplitude. The present investigation confirms these findings as the amplitude of -9 mode is found to be independent of the +7 mode (source) amplitude. This was observed in a previous study in this work where the effects of swirl inlet boundary condition on mode amplitudes at Station 30 were studied (results have been presented in Figure 41). It was observed that the presence of inlet-swirl boundary condition reduces the amplitude of +7 mode but does not affect the -9 mode amplitude at Station 30.

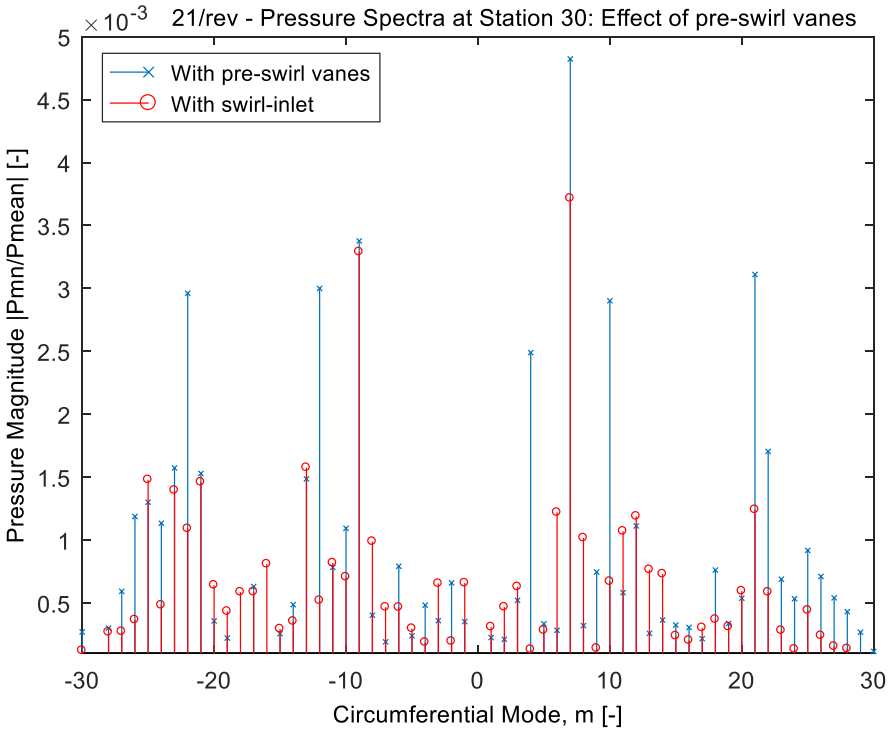

Figure 63 Effects of adding pre-swirl vanes on 21/rev (BPF) modes at Station 30.

B.4. Experimental Validation

Resolution [voxels/ wavelength]	Impeller y^+	Error in stage Temperature Ratio [%]	Error in stage Polytropic Efficiency [%]	Error in stage Pressure Ratio [%]	Error in SPL [dBs]
138	12-138	2.44	4.76	5.8	-0.5

Table 12 Experimental validation of the case with pre-swirl vanes.

Key performance, as well as acoustics parameters from CFD simulation, are compared with test rig data and the findings are mentioned in Table 12. The discrepancy in stage pressure ratio increased due to the addition of pre-swirl blade rows. This can be attributed to the additional friction losses added to the system due to the physical addition of blade rows rather than imposing the inlet-swirl. The total pressure at Station 10 is further reduced, thus, further increasing the overall stage pressure ratio. The predicted polytropic efficiency is closer to test rig data since the temperature ratio is over-predicted as well.

However, the discrepancy in SPL at Station 30 decreased. With an accuracy of <1 dB, the SPL at Station 30 agrees well with the experimental data. This can be attributed to the increased hydrodynamic interaction between the blade rows upstream of the impeller.

C. UDF in PowerFLOW

```
// SETTING INLET SWIRL//
Beta = -45 <<degree>><<rad>>;
Azimuth = atan2(y,z)l
Inlet_surf = 0.037649 <<m^2>>;
Mflux_x = mf_inlet/inlet_surf;
Mflux_y = mf_inlet/inlet_surf*tan(beta)*cos(azimuth);
Mflux_z = mf_inlet/inlet_surf*tan(beta)*(-sin(azimuth));
```

D. Description of Fluent code

The commercial code Fluent 18.1 has been used to simulate the unsteady flow field of the research compressor. Fluent is a finite-volume based flow solver which solves the set of equations for 3D unsteady compressible flow. The flow domain is discretised into finite volumes where a control-volume form of mass, momentum and energy conservation equations are solved.

D.1. Overview of density-based solver

The density-based solver was originally developed for high-speed compressible flows. It is based on a coupled approach where the governing equations of continuity, momentum, energy and species are solved simultaneously. The discrete, non-linear governing equations are linearised to obtain a system of equations for dependent variables in every finite volume (cell). This results in a linear system which is then solved to obtain the updated flow solution [88]. The solution algorithm is presented in Figure 64 [88].

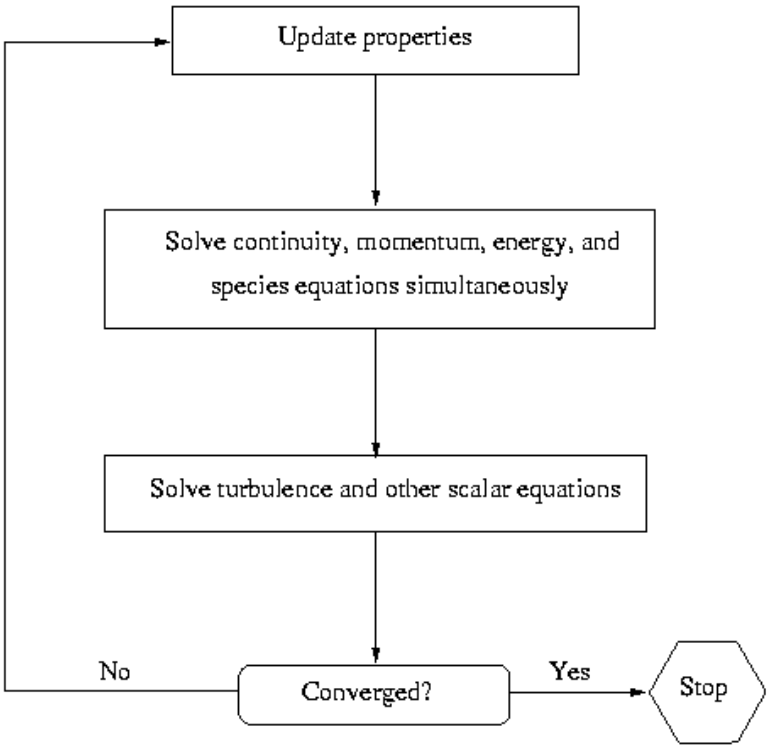

Figure 64 Overview of Density-based solution algorithm. [88]

Fluent offers two formulations to solve the governing equations, coupled-explicit and the coupled-implicit:

- Implicit method: Each cell variable is computed using a formulation that includes both existing and unknown values from the neighbouring cells. Therefore, the equations must be solved simultaneously to obtain the unknown quantities. In summary, the coupled-implicit formulation solves all flow variables in every cell at the same time.
- Explicit method: Each cell variable is calculated using a formulation that includes only the known values. In this case, the equations must be solved one at a time to give unknown variables. In summary, the coupled-explicit approach solves all flow variables in one cell at a time.

In comparison, the implicit method is computationally expensive and harder to implement. Therefore, an explicit scheme has been implemented in this investigation.

D.2. Governing Equations in Vector Form

The Navier-Stokes system of governing equation written to describe mean fluid properties is presented in an integral Cartesian form for the given control volume *V* where the differential surface area is denoted by *dA* [88]:

$$\frac{\partial}{\partial t}\int_V W dV + \oint [F - G].dA = \int_V H dV \tag{7.7}$$

where vectors *F, G* and *W* are defined as follows

$$W = \begin{Bmatrix} \rho \\ \rho u \\ \rho v \\ \rho w \\ \rho E \end{Bmatrix}, F = \begin{Bmatrix} \rho v \\ \rho v u + p\hat{i} \\ \rho v v + p\hat{j} \\ \rho v w + p\hat{k} \\ \rho v E + pv \end{Bmatrix}, G = \begin{Bmatrix} 0 \\ \tau_{xi} \\ \tau_{yi} \\ \tau_{zi} \\ \tau_{ij} v_j + q \end{Bmatrix} \tag{7.8}$$

and the vector *H* constitutes source terms, for example, energy sources and body forces.

Here *v, ρ, p* and *E* are velocity, density, pressure and energy per unit mass, respectively. Heat flux is denoted by q and viscous stress tensor is denoted by τ.

The relationship between total energy *E* and the total enthalpy *H* is given by [88]:

$$E = H - \frac{p}{\rho} \tag{7.9}$$

where

$$H = h + \frac{|v|^2}{2} \tag{7.10}$$

Due to the high disparity between fluid velocity *v* and the acoustic speed of sound *c* at low Mach numbers, the Navier-Stokes equation is given in Equation 7.7 becomes highly stiff. This is worse in case of incompressible flows where acoustic waves travel infinitely fast [88]. The numerical stiffness of Navier-Stokes equation results in poor convergence [88].

Bibliography

[1] C. Matteo, P. X. Dionysios, E. B. Ala, F. M.-B. Ricardo, M. Flavio and F. T. Nina, "Simultaneous Nonlinear Reconciliation and Update of Parameters for Online Use of First-Principles Models: An Industrial Case-Study on Compressors," *Computer Aided Chemical Engineering,* vol. 33, pp. 457-462, 2014.

[2] S. Konig and N. Petry, "Aeroacoustic Phenomenon in High-Pressure Centrifugal Compressors- A Possible Root Cause for Impeller Failures," in *Proceedings of the 38th Turbomachinery Symposium*, Texas, 2009.

[3] F. L. Eisinger, "Acoustic Fatigue of Impellers of Rotating Machinery," *Journal of Pressure Vessel Technology,* vol. 124, pp. 154-160, 2002.

[4] S. K. Richards, F. Moyroud and A. Picavet, "Unsteady acoustic forcing on an impeller due to coupled blade row interactions," in *ASME Turbo Expo 2010: Power for Land, Sea and Air*, Glasgow, UK, 2010.

[5] N. G. Díez, J. Smeulers, F. Moyroud and K. Ramakrishnan, "Aero-Acoustic Analysis of a Low-Pressure Centrifugal Compressor Stage," in *IMECH*, 2016.

[6] K. A. Gould, "Characterization of unsteady flow processes in a centrifugal compressor stage," MIT, Massachusetts, 2006.

[7] L. F. Coffin, "Designing for Low Cycle Fatigue," in *SESA Design Clinics Manual*, Detroit, 1959.

[8] G. R. Sorenson and H. R. Clement, "Low-cycle Fatigue in Small Turbines," in *SESA Spring Meeting*, Indianapolis, 1960.

[9] R. Nisbett, G. Budynas and J. Keith, in *Shigley's Mechanical Engineering*, McGraw-Hill, 8th edition, 2008, p. 265.

[10] H.-L. Wang, G. Xi, J.-Y. Li and M.-J. Yuan, "Effect of the tip clearance variation on the performance of a centrifugal compressor with considering impeller deformation," *Proceedings of the Institution of Mechanical Engineers Part A Journal of Power and Energy,* vol. 8, no. 225, pp. 1143-1155, 2011.

[11] J. S. Caitlin, "Forced response predictions in modern centrifugal compressor design," MIT, Massachusetts, 2005.

[12] O. Eric, H. Steve, O. Maki and M. William, *Interference Diagrams – When Campbell diagrams are not enough,* Whippany, New Jersey: Mechanical Solutions Inc., 2006.

[13] M. P. Boyce, "Rotor Dynamics," in *Gas Turbine Engineering Handbook (4th Edition)*, Elsevier, 2011.

[14] A. Zemp, "Experimental investigation and validation of high cycle fatigue design systems for centrifugal compressors," ETH, Zurich, 2012.

[15] L. Toni, F. Moyroud, K. Ramakrishnan, V. Michelassi and E. Schurr, "Prediction and validation of high-performance centrifugal compressor impeller forced response," in *Proceedings of 12th European Conference on Turbomachinery Fluid dynamics & Thermodynamics*, Stockholm, Sweden, 2017.

[16] L. Eckert and A. Ni, "High Cycle Cracks at Radial Fan Impellers Caused by Aeroelastic Self-Excited Impeller Vibrations Part 1: Case History, Root Cause Analysis, Vibration Measurements," in *17th Biennial conference on mechanical vibration and noise*, Las Vegas, 1999.

[17] N. Petry and S. Koenig, "Experimental study of acoustic resonances in the side cavities of a high-pressure centrifugal compressor excited by rotor/stator interaction," in *ASME Turbo Expo 2010: Power for Land, Sea, and Air*, Glasgow, 2010.

[18] A. Kumlu, "CFD investigation of impeller-diffuser interaction effects on a radial compressor stage," KTH School of Industrial Engineering and Management, Stockholm, 2014.

[19] J. M. Tyler and T. G. Sofrin, "Axial Flow Compressor Noise Studies," *SAE Transactions,* vol. 70, pp. 309-332, 1961.

[20] E. J. Walton and C. S. Tan, "Forced Response of a Centrifugal Compressor Stage Due to the Impeller–Diffuser Interaction," *Journal of Turbomachinery,* vol. 138, no. 9, pp. 1-13, 2016.

[21] R. Ciorciari, A. Lesser, F. Blair and R. Niehuis, "Numerical Investigation of Tip Clearance Effects in an Axial Transonic Compressor," *Journal of Thermal Science,* vol. 21, no. 2, 2012.

[22] J. Fernández Oro, K. Argüelles Díaz, C. Santolaria Morros and E. Blanco Marigorta, "Unsteady rotor-stator interaction in an axial flow blower Part 1: Numerical and experimental flow field characterisation," in *ASME Fluids Engineering Division Summer Meeting and Exhibition*, Houston, TX, USA, 2005.

[23] C. L. Munch and J. B. Ollerhead, "An application of theory to axial compressor noise," *The Journal of the Acoustical Society of America,* vol. 48, no. 1A, 1970.

[24] R. Parker, "Acoustic Resonances and Blade Vibration in Axial Flow Compressors," *Journal of Sound and Vibration,* vol. 92, no. 4, pp. 529-539, 1984.

[25] R. Parker, "Resonance effects in Wake Shedding From Parallel Plates: Calculation of Resonant Frequencies," *Journal of Sound and Vibration,* pp. 330-343, 1967.

[26] R. Parker, "Resonance Effects in Wake Shedding from Compressor Blading," *Journal of Sound and Vibration,* vol. 6, no. 3, pp. 302-309, 1967.

[27] R. Parker and D. Pryce, "Wake-Excited Resonances in an Annular Cascade: An Experimental Investigation," *Journal of Sound and Vibration,* vol. 37, no. 2, pp. 247-261, 1974.

[28] R. Parker and S. Stoneman, "An Experimental Investigation of the Generation and Consequences of Acoustic Waves in an Axial Flow Compressor: Large Axial Spacing between Blade Rows," *Journal of Sound and Vibration,* vol. 99, pp. 169-192, 1985.

[29] S. Konig, "Acoustic Eigenmodes in the Side Cavities of Centrifugal Compressors," *ASME Turbo Expo 2009: Power for Land, Sea, and Air,* vol. 6, pp. 547-557, 2009.

[30] H. W. D. Chiang and R. E. Kielb, "An analysis system for blade forced response," *ASME Journal of Turbomachinery,* vol. 115, no. 1, pp. 762-770, 1993.

[31] H. D. Li and L. He, "Single-passage analysis of unsteady flows around vibrating blades of a transonic fan under inlet distortion," *ASME Journal of Turbomachinery,* vol. 124, no. 2, pp. 285-292, 2002.

[32] W. Ning, S. Moffat, Y. Li and R. G. Wells, "Blade forced response prediction for industrial gas turbines Part 1: Methodologies," in *ASME Turbo Expo 2003*, Atlanta, Georgia, USA, 2003.

[33] W. Ning, S. Moffat, Y. Li and R. G. Wells, "Blade forced response prediction for industrial gas turbines Part 2: Verification and application," in *ASME Gas Turbine Conference and Exhibit*, Atlanta, Georgia, 2003.

[34] S. Schmitt, "Simulation von Flattern und aerodynamischer Zwangserregung in Turbomaschinenbeschaufelungen," Institut für Antriebstechnik, Koln, 2003.

[35] H. Dickmann, T. Wimmel, J. Szwedowicz, D. Filsinger and C. H. Roduner, "Unsteady flow in a turbocharger centrifugal compressor: Three-dimensional computational fluid

dynamics simulation and numerical and experimental analysis of impeller blade vibration," *ASME Journal of Turbomachinery,* vol. 3, no. 128, pp. 455-465, 2006.

[36] F. Lyman, "On the Conservation of Rothalpy in Turbomachines," *ASME Journal of Turbomachinery,* vol. 115, no. 3, p. 520, 1993.

[37] G. Franke, R. Fisher, C. Powell, U. Seidel and J. Koutnik, "On Pressure Mode Shapes Arising from Rotor/Stator Interactions," *Sound and Vibration Magazine,* vol. 39, pp. 14-18, 2005.

[38] A. Zemp and R. S. Abhari, "Vaned Diffuser Induced Impeller Blade Vibrations in a High-Speed Centrifugal Compressor," *ASME Journal of Turbomachinery,* vol. 135, no. 2, p. 9 Pages, 2013.

[39] A. D. Villanueva, "Characterization of the flow field response to vaneless space reduction in centrifugal compressors," MIT Press, Massachusetts, 2006.

[40] K. Gallier, "Experimental Characterization of high-Speed Centrifugal Compressor Aerodynamic Forcing Function," Purdue University Press, Purdue, 2005.

[41] N. Petry, F. K. Benra, S. Konig and C. Woiczinski, "Interaction Between Aerodynamic Phenomenon and Impeller Structure of High-Pressure Radial Compressors," in *8th European Turbomachinery Conference*, Graz, Austria, 2009.

[42] N. Petry, S. Konig and F. Benra, "Influence of the Swirling Flow in the Side Cavities of a High-Pressure Centrifugal Compressor on the Characteristics of Excited Acoustic Modes," *Journal of Turbomachinery,* vol. 3, no. 135, p. 11 pages, May 2013.

[43] K. Vogel, R. S. Abhari and A. Zemp, "Experimental and numerical investigation of the unsteady flow field in a vaned diffuser of a high-speed centrifugal compressor," in *ASME Turbo Expo 2014: Turbine Technical Conference and Exposition*, Düsseldorf, Germany, June 16–20, 2014.

[44] K. A. Gould, C. S. Tan and M. Macrorie, "Characterization of Unsteady Impeller-Blade Loading in a Centrifugal Compressor with a Discrete Passage Diffuser," *ASME Turbo Expo 2007: Power for Land, Sea, and Air,* vol. 6, pp. 1781-1790, 2007.

[45] C. Lusardi, "Characterization of Unsteady Loading Due to Impeller-Diffuser Interaction in Centrifugal Compressors," MIT, Massachusetts, 2012.

[46] Y. Leng and S. Fleeter, "Analytical Modeling of the Unsteady Wave Propagation in the Vaneless Space of a Low-Speed Centrifugal Compressor," in *22nd International Compressor Engineering Conference*, Purdue, West Lafayette, 2014.

[47] U. Haupt and M. Rautenberg, "Investigation of blade vibration of radial impellers by means of telemetry and holographic interferometry," *ASME Journal of Engineering for Gas Turbines and Power,* vol. 104, no. 4, pp. 838-843, 1982.

[48] K. Salzle, "Schwingungsverhalten der Laufräder von Radialventilatoren: Dissertation Universität Stuttgart," University of Stuttgart, Stuttgart, 2001.

[49] D. Jin, "Untersuchung von Schaufelschwingungen und ihrer Erregungsursachen an Radialverdichtern," University of Hannover, Hannover, 1990.

[50] A. Kammerer and R. S. Abhari, "Experimental study on impeller blade vibration during resonance: Part 1: Blade vibrations due to inlet flow distortion," *Journal of Engineering for Gas Turbines and Power,* vol. 131, no. 1, pp. 508-518, 2009.

[51] A. Kammerer and R. S. Abhari, "Blade forcing function and aerodynamic work measurements in a high-speed centrifugal compressor with inlet distortion," in *ASME Turbo Expo 2009: Power for Land, Sea, and Air*, Orlando, Florida, USA, June 8–12, 2009.

[52] F. L. Eisinger and R. E. Sullivan, "Vibration Fatigue of Centrifugal Fan Impeller due to Structural-Acoustic Coupling and its Prevention: A Case Study," *Journal of Pressure Vessel Technology,* vol. 129, pp. 771-774, November 2007.

[53] A. Kammerer, "Experimental research into resonant vibration of centrifugal compressor blades," ETH University Press, Zurich, 2010.

[54] A. H. Epstein, J. B. Gertz, P. R. Owen and M. B. Giles, "Vortex Shedding in High-Speed Compressor Blade Wakes," *Journal of Propulsion,* vol. 4, no. 3, pp. 236-246, 1987.

[55] T. F. Fric, R. Villarreal, R. O. Auer, M. L. James, D. Ozgur and S. T. K., "Vortex Shedding From Struts in an Annular Exhaust Diffuser," *Journal of Turbomachinery,* vol. 1, no. 120, 01 January 1998.

[56] S. Ziada, A. Oengören and A. Vogel, "Acoustic Resonance in the Inlet Scroll of a Turbo-Compressor," *Journal of Fluids and Structures,* vol. 13, no. 3, pp. 361-373, 2002.

[57] R. Parker and S. Stoneman, "The Excitation and Consequences of Acoustic Resonances in Enclosed Fluid Flow around Solid Bodies," Proc. Inst. Mech. Eng, 1989.

[58] P. Tucker, "Computation of Unsteady Turbomachinery Flows: Part 1 - Progress and Challenges," *Progress in Aerospace Sciences,* vol. 47, pp. 522-545, October October 2011.

[59] NUMECA International, "Theoretical Manual FINETM/Turbo v8.7 Flow Integrated Environment, Documentation v8b," NUMECA, Belgium, May 2010.

[60] S. Vilmin, E. Lorrain, C. Hirsch and M. Swoboda, "Unsteady flow modelling across the rotor/stator interface using the nonlinear harmonic method," in *ASME Turbo Expo 2006: Power for Land, Sea, and Air*, Barcelona, Spain, 2006.

[61] M. Mansour and M. Kruse, "Time Unsteady Impeller-Diffuser Interaction in Gas Turbine Engines," in *Proceedings of the 5th National Turbine Engine High Cycle Fatigue (HCF) Conference*, Chandler, AZ, 2000.

[62] M. Shur, M. Strelets, A. Travin, P. Spalart, Suzuki and Takao, "Unsteady Simulations of a Fan/Outlet-Guide-Vane System: Aerodynamics and Turbulence," *AIAA Journal,* vol. 56, no. 6, pp. 2283-2297, 2018.

[63] H. Hasemann, D. Hagelstein and M. Rautenberg, "Coupled vibration of unshrouded centrifugal compressor impellers. Part 1: Experimental Investigation," *International Journal of Rotating Machinery,* vol. 6, no. 2, pp. 101-113, 2000.

[64] K. Satish, E. Guidotti and D. T. Rubino, "Accuracy of centrifugal compressor stages performance predictions by means of high fidelity CFD and validation using advanced aerodynamic probe," in *ASME Turbo Expo 2013: Turbine Technical Conference and Exposition*, San Antonio, Texas, 2013.

[65] C. Clancy, F. Moyroud and K. Ramakrishnan, "Effect of cavities on impeller aeromechanical forcing in a low-pressure ratio centrifugal compressor stage," in *Proceedings of ASME Turbo Expo 2014: Turbine Technical Conference and Exposition*, Düsseldorf, Germany, 2014.

[66] A. D. Jong, "Aeroacoustic Resonance of Slender Cavities," Delft, Netherlands, 2012.

[67] P. Bhatnagar, E. Gross and M. Krook, "A model for Collision Processes in Gases: Small Amplitude Processes in Charged and Neutral One-Component Systems," *Physical Review,* vol. 94, no. 3, pp. 511-525, May 1954.

[68] S. Succi, The lattice Boltzmann equation for fluid dynamics and beyond, Oxford University Press, 2001.

[69] S. Chen and G. Doolen, "Lattice Boltzmann method for fluid flows," *Annual Review of Fluid Mechanics,* vol. 30, pp. 329-364, 1998.

[70] B. Crouse, S. Senthooran, G. Balasubramaniam, D. Freed and K. Karbon, "Computational Aeroacoustics Investigation of Automobile Sunroof Buffeting," in *SAE 2007 Noise and Vibration Conference and Exhibition*, 2007.

[71] B. Crouse, D. Freed, S. Senthooran, F. Ullrich and S. Fertl, *Analysis of Underbody Windnoise Sources on a Production Vehicle using a Lattice Boltzmann Scheme,* SAE Technical Paper, 2007.

[72] A. De Jong and H. Bijl, "Investigation of higher spanwise Helmholtz resonance modes in slender covered cavities," *Journal of Acoustical Society of America,* vol. 128, no. 4, pp. 1668-1678, 2010.

[73] M. Howe, "Low Strouhal number instabilities of flow over apertures and wall cavities," *Journal of Acoustical Society of America,* vol. 315, pp. 772-780, 1992.

[74] G. Kooijman, A. Hirschberg and J. Golliard, "Acoustic response of orifices under grazing flow: Effects of boundary layer profile and geometry," *Journal of Sound and Vibration,* vol. 315, pp. 849-874, 2008.

[75] P. Nelson, N. Halliwell and P. Doak, "Fluid Dynamics of a Flow Excited Resonance, Part 2: Flow Acoustic Interaction," *Journal of Sound and Vibration,* vol. 91, no. 3, pp. 375-402, 1983.

[76] A. Silva and G. Scavone, "Lattice Boltzmann simulations of the acoustic radiation from waveguides," *Journal of Physics,* vol. 40, no. 3, pp. 397-408, 2007.

[77] X. Li, R. Leung and R. So, "One-step Aeroacoustics Simulation using Lattice Boltzmann Method," *AIAA Journal,* vol. 44, no. 1, pp. 78-89, January 2006.

[78] D. F. Funglsang and A. Cain, "Evaluation of shear layer cavity resonance mechanisms by numerical simulations," in *30th Aerospace Sciences Meeting and Exhibit*, Reno, Nevada, 1992.

[79] T. Colonius, A. Basu and C. and Rowley, "Numerical investigation of the flow past a cavity," in *5th AIAA/CEAS Aeroacoustics Conference and Exhibit*, Washington, 1999.

[80] C. Rowley, T. Colonius and A. and Basu, "On self-sustained oscillations in two-dimensional compressible flow over rectangular cavities," *Journal of Fluid Mechanics,* vol. 455, pp. 315-346, 2002.

[81] G. Bres, M. Wessels and N. S., "Tandem Cylinder Noise Predictions using Lattice Boltzmann and Ffowcs Williams-Hawkings Methods," in *16th AIAA/CEAS Aeroacoustics Conference*, Stockholm, Sweden, June 2010.

[82] Y. Dubief and F. Delcayre, "On coherent-vortex identification in turbulence," *Journal of Turbulence,* pp. 1-23, 2000.

[83] M. I. Gonzalez and D. Casalino, "Fan Tonal and Broadband Noise Simulations at Transonic Operating Conditions Using Lattice-Boltzmann Methods," in *AIAA/CEAS Aeroacoustics Conference*, Atlanta, Georgia, 2018.

[84] M. I. Gonzalez, J. Wang, G. Romani and D. Casalino, "Rotor Noise Generation in a Turbulent Wake Using the Lattice-Boltzmann Method," in *AIAA/CEAS Aeroacoustics Conference*, Atlanta, Georgia, 2018.

[85] R. Kielb, "CFD for Turbomachinery Unsteady Flows- An Aeroelastic Design Perspective," in *39th Aerospace Sciences Meeting and Exhibit*, Reno, NV, U.S.A., 2001.

[86] ANSYS, " Including Production Limiters for Two-Equation Models," 2017. [Online]. Available: https://www.sharcnet.ca/Software/Ansys/17.0/en-us/help/flu_ug/flu_ug_sec_options_two_eq_prod_lim_setup.html.

[87] B. Launder and M. Kato, "Modeling flow-induced oscillations in turbulence flow around a square cylinder," *ASME FED,* no. 116, pp. 189-199, 1993.

[88] Fluent Inc., "Fluent 18.1 User's Guide," [Online].

[89] R. Brossier, J. Virieux and S. Operto, "Parsimonious finite-volume frequency-domain method for 2-D P–SV-wave modelling," *Geophysical Journal International,* vol. 175, no. 2, pp. 541-559, 2008.

[90] Institute of Propulsion Technology, DLR, "Mesh Generation," 2015. [Online]. Available: https://www.dlr.de/at/en/desktopdefault.aspx/tabid-1540/2452_read-3822/. [Accessed 2019].

[91] B. Roy and A. M. Pradeep, "Jet Aircraft Propulsion," IIT Bombay, 3008.

[92] B. Y., X. Carbonneau, G. Dufour, N. Binder and I. Trébinjac, "Simulations, Analysis of the Unsteady Flow Field in a Centrifugal Compressor from Peak Efficiency to Near Stall with Full-Annulus," *International Journal of Rotating Machinery,* 2014.

[93] SIMULIA Corp., "PowerFLOW-Users Guide," 2016.

[94] V. A. Levashov and K. Y. Lyubchenko, "Determination of Pressure Fluctuations in Rotor Bundle of Centrifugal Compressor at Critical Conditions of Operation," in *Internation Conference on Compressors and their Systems*, Sumy, 2017.

[95] G. Franke, R. Fisher, C. Powell, U. Seidel and J. Koutnik, "On Pressure Mode Shapes Arising from Rotor/Stator Interactions," *Sound and Vibration Magazine,* vol. 39, pp. 14-18, 2005.

[96] R. Parker and S. Stoneman, "An Experimental Investigation of Generation and Consequences of Acoustic Waves in an Axial Flow Compressor: The Effects of Variations in the Axial Spacings between Blade Rows," *Journal of Sound and Vibration,* vol. 116, no. 3, pp. 509-525, 1987.

[97] U. Haupt and M. Rautenberg, "Blade excitation by broadband pressure fluctuations in a centrifugal compressor," in *ASME Gas Turbine Conference and Exhibition*, Anaheim, 1987.

[98] D. Hagelstein, H. Hasemann and M. Rautenberg, "Coupled vibration of unshrouded centrifugal compressor impellers. Part 2: Computation of vibrationbehaviour," *International Journal of Rotating Machinery,* vol. 6, no. 2, pp. 115-128, 2000.

[99] S. R. Manwaring and S. Fleeter, "Inlet distortion generated periodic aerodynamic rotor response," *ASME Journal of Turbomachinery,* vol. 112, no. 2, pp. 298-310, 1990.

[100] S. Vilmin, E. Lorrain, C. Hirsch and M. Swoboda, "Unsteady flow modelling across the rotor/stator interface using the nonlinear harmonic method," in *ASME Turbo Expo 2006: Power for Land, Sea, and Air*, Barcelona, Spain, 2006.

[101] H. Bryans, A. C. Moussa and Z. Tomsho, "Application of Viscous Flow Computations for the Aerodynamic Performance of a Backswept Impeller at Various Operating Conditions," *ASME Journal of Turbomachinery,* vol. 110, no. 3, pp. 303-311, 1988.

[102] R. M. Chriss, M. D. Hathaway and J. Wood, "Experimental and Computational Results from the NASA Lewis Low-Speed Centrifugal Impeller at Design and Part Flow Conditions," *ASME Journal of Turbomachinery,* vol. 118, no. 1, pp. 55-65, 1996.

[103] M. Hosseini, Z. Sun, X. He and X. Zheng, "Effects of Radial Gap Ratio between Impeller and Vaned Diffuser on Performance of Centrifugal Compressors," *MDPI,* pp. 1-27, 2017.

[104] S. Patrick and Y. Kwong, "impeller-Diffuser Interaction in Centrifugal Compressors," MIT Press, Massachusetts, 2000.

[105] K. Kirtley and T. Beach, "Deterministic Blade Row Interactions in a Centrifugal Compressor Stage," *ASME Journal of Turbomachinery,* vol. 2, no. 114, pp. 304-311, 1992.

[106] N. P. Murray, "Effects of Impeller-Diffuser interactions on Centrifugal Compressor Performance," MIT Press, Massachusetts, 2008.

[107] M. Philips, "Role of Flow Alignment and Inlet Blockage on Vaned Diffuser Performance," MIT, Massachusetts, 1997.

[108] A. D. Jong, "Aeroacoustic Resonance of Slender Cavities," Delft, 2012.

[109] X. Li, R. Leung and R. So, "One-step Aeroacoustics Simulation using Lattice Boltzmann Method," *AIAA Journal,* vol. 44, no. 1, pp. 78-89, January 2006.

[110] S. Noelting, M. Wessels and D. M. Freed, "Prediction of Aeroacoustic Noise from a simplified Landing Gear Using a Lattice-Boltzmann-Scheme," in *46th AIAA Aerospace Sciences Meeting and Exhibit*, Reno, Nevada, January 2008.

[111] F. Perot, M. Meskine and S. Vergne, "Investigation of the statistical properties of pressure loadings on real automotive side glasses," in *15th AIAA/CEAS Aeroacoustic Conference*, Miami, Florida, May 2009.

[112] D. Lee, F. Perot and D. Freed, "The prediction of flow-induced noise related to automotive HVAC systems," in *SAE 2011 World Congress & Exhibition*, 2011.

[113] F. Perot, D. Kim and K. D. Lee, "Direct aeroacoustic prediction of ducts and vent noise," in *16th AIAA/CEAS Aeroacoustics Conference*, Stockholm, Sweden, June, 2010.

[114] B. Crouse, S. Senthooran, G. Balasubramaniam, D. Freed and K. Karbon, "Computational Aeroacoustics Investigation of Automobile Sunroof Buffeting," in *SAE 2007 Noise and Vibration Conference and Exhibition*, 2007.

[115] B. Crouse, G. Balasubramaniam, S. Senthooran and D. Freed, "Investigation of gap deflector efficiency for the reduction of sunroof buffeting," *SAE Technical Paper,* 2009.

[116] H. Chen, C. M. Teixeira and K. Molvig, "Digital Physics Approach to CFD: Some Basic Theoretical Features," *International Journal of Modern Physics,* vol. 8, no. 4, pp. 675-684, 1997.

[117] H. Chen, C. Teixeira and K. and Molvig, "Realization of Fluid Boundary Conditions via Discrete Boltzmann Dynamics," *International Journal of Modern Physics,* vol. 9, no. 8, pp. 1281-1292, 1998.

[118] M. Åbom, "Turbomachinery Aeroacoustics," in *12th European Turbomachinery Conference*, Stockholm, 2017.